NATIONAL ACADEMY OF SCIENCES OF UKRAINE ● G. V. KURDYUMOV INSTITUTE FOR METAL PHYSICS

AN INTERNATIONAL RESEARCH JOURNAL

METALLOPHYSICS AND ADVANCED TECHNOLOGIES

(Metallofizika i Noveishie Tekhnologii)

FOUNDED IN SEPTEMBER, 1979

Volume 47, No. 3; March 2025

CONTENTS

Editorial Announcements	Information for Foreign Subscribers	V
	Information for Contributors	VII
Phase Transformations	Morphology of Cementite Formed as a Result of Austenite Decomposition During Cooling of Overheated Hypereutectoid Steels *J. A. HARASYM and N. O. BONDAREVS'KA*	237
	Development of a Titanium Aluminide Alloy of Optimal Composition by Means of Modification *O. B. HALIENKOVA, V. S. YEFANOV, O. V. ZAVGORODNIY, I. M. KIRIAN, S. O. BULISH, and O. D. RUD*	245
Crystal Lattice Defects	Sintered Al–Si–Ni Alloy: Structure and Properties. II. Sintering and Forging *V. V. KAVERINSKY, G. A. BAGLIUK, S. F. KYRYLYUK, D. G. VERBYLO, Z. P. SUKHENKO, I. M. KIRIAN, M. A. SKORYK, and O. D. RUD*	257
	The Influence of the Size of the Brazing Gap on the Structure and Strength of Kovar Joints with Stainless Steel *S. V. MAKSYMOVA, P. V. KOVAL'CHUK, and V. V. VORONOV*	271
Physics of Strength and Plasticity	The Effect of Heat Treatment on the Physical and Mechanical Properties, and Grindability of the Amorphous $Fe_{73}Si_{16}B_7Cu_1Nb_3$ Alloy Ribbon *B. S. BAITALIUK, V. K. NOSENKO, and I. K. YEVLASH*	287
	The Effect of the Shear-Stress Field in the Glide Plane on Solid Solution Strengthening in Multicomponent Alloys *M. I. LUGOVYY, D. G. VERBYLO, and*	

CONTENTS, No. 3 (Vol. 47)

M. P. BRODNIKOVSKYY 303

Analysis of Deformation Forces in Simulation of a New Thermomechanical Wire Processing
I. E. VOLOKITINA and E. A. PANIN 335

Scientific Editors of Issue—*O. S. Gatsenko, V. A. Tatarenko*
Executive Managing Editor—*O. S. Gatsenko*
Editors—*L. I. Makarenko, M. V. Manilo, I. V. Zagorulko*
The artwork for direct reproduction is made by computer group of EPD of the G. V. Kurdyumov Institute for Metal Physics, N.A.S. of Ukraine

Editorial Office Address:
G. V. Kurdyumov Institute for Metal Physics, N.A.S. of Ukraine, EPD—'MNT',
36 Academician Vernadsky Boulevard, UA-03142 Kyiv, Ukraine
Telephone: +380 44 4249042. Fax: +380 44 4242561. E-mail: mfint@imp.kiev.ua
Media Identifier R30-03171

Approved for publication by the Academic Council of the G. V. Kurdyumov Institute for Metal Physics of the National Academy of Sciences of Ukraine
Published in English or Ukrainian languages according to resolution of Editorial Board of the journal

Printed by Publishing House 'Akademperiodyka', of the NAS of Ukraine
4 Tereshchenkivs'ka Str., UA-01024 Kyiv, Ukraine
Registration Certificate of Publishing Subject: ДК № 544 on 27.07.2001

Journal website: http://mfint.imp.kiev.ua
Journal DOI: https://doi.org/10.15407/mfint

Issue DOI: https://doi.org/10.15407/mfint.47.03

НАЦІОНАЛЬНА АКАДЕМІЯ НАУК УКРАЇНИ ● ІНСТИТУТ МЕТАЛОФІЗИКИ ім. Г. В. Курдюмова

МЕТАЛОФІЗИКА ТА НОВІТНІ ТЕХНОЛОГІЇ

МІЖНАРОДНИЙ НАУКОВИЙ ЖУРНАЛ
ЗАСНОВАНИЙ У ВЕРЕСНІ 1979 р.

Том 47, № 3; березень, 2025

ЗМІСТ

Редакційні оголошення	Інформація для закордонних передплатників	V
	Інформація для авторів	VII
Фазові перетворення	Морфологія цементиту, сформованого в результаті розпаду аустеніту під час охолодження перегрітих заевтектоїдних криць *Ю. А. ГАРАСИМ, Н. О. БОНДАРЕВСЬКА*	237
	Розробка стопу алюмініду Титану оптимального складу шляхом модифікування *О. Б. ГАЛЄНКОВА, В. С. ЄФАНОВ, О. В. ЗАВГОРОДНІЙ, І. М. КІР'ЯН, С. О. БУЛІШ, О. Д. РУДЬ*	245
Дефекти кристалічної ґратниці	Спечений стоп Al–Si–Ni: структура та властивості. 2. Спікання та кування *В. В. КАВЕРИНСЬКИЙ, Г. А. БАГЛЮК, С. Ф. КИРИЛЮК, Д. Г. ВЕРБИЛО, З. П. СУХЕНКО, І. М. КІР'ЯН, М. А. СКОРИК, О. Д. РУДЬ*	257
	Вплив розміру паяльного зазору на структуру та міцність з'єднань ковару із неіржавійною крицею *С. В. МАКСИМОВА, П. В. КОВАЛЬЧУК, В. В. ВОРОНОВ*	271
Фізика міцности та пластичности	Вплив термічного оброблення на фізико-механічні властивості та здатність до подрібнення стрічки з аморфного стопу $Fe_{73}Si_{16}B_7Cu_1Nb_3$ *Б. С. БАЙТАЛЮК, В. К. НОСЕНКО, І. К. ЄВЛАШ*	287
	Вплив поля напружень зсуву в площині ковзання на зміцнення твердого розчину в багатокомпонентних стопах *М. І. ЛУГОВИЙ, Д. Г. ВЕРБИЛО, М. П. БРОДНІКОВСЬКИЙ*	303
	Аналіза деформаційних сил у моделюванні нового термомеханічного оброблення дроту	

І. Є. ВОЛОКІТІНА, Є. А. ПАНІН 335

Наукові редактори випуску: *О. С. Гаценко, В. А. Татаренко*
Відповідальний секретар редакційної колегії *О. С. Гаценко*
Редактор-коректор *О. С. Гаценко*
Технічні редактори: *І. В. Загорулько, Л. І. Макаренко, М. В. Маніло*
Художні редактори: *І. В. Загорулько, Л. І. Макаренко, М. В. Маніло*
Оригінал-макет для прямого репродукування виготовлено комп'ютерною групою РВВ Інституту металофізики ім. Г. В. Курдюмова НАН України

Адреса редакції:
Інститут металофізики ім. Г. В. Курдюмова НАН України, РВВ—Редакція «МНТ»
бульв. Акад. Вернадського, 36; 03142 Київ, Україна
Тел.: +380 44 4249042; факс: +380 44 4242561
Ел. пошта: mfint@imp.kiev.ua
Ідентифікатор медіа R30-03171

Затверджено до друку вченою радою Інституту металофізики ім. Г. В. Курдюмова НАН України
Друкується за постановою редакційної колегії журналу англійською або українською мовами

Підписано до друку 27.03.2025 р. Формат 70×100/16.
Ум. друк. арк. 9,59. Обл.-вид. арк. 8,82.
Тираж 54 пр. Зам. № 0000 від 27.03.2025 р.

Віддруковано ВД «Академперіодика» НАН України
вул. Терещенківська, 4; 01024 Київ, Україна
Свідоцтво суб'єкта видавничої справи ДК № 544 від 27.07.2001 р.

Сайт журналу: http://mfint.imp.kiev.ua
DOI (журналу): https://doi.org/10.15407/mfint
DOI (випуску): https://doi.org/10.15407/mfint.47.03

INFORMATION (GUIDELINES) FOR CONTRIBUTORS

Submission of Manuscripts: Manuscripts should be sent by e-mail (mfint@imp.kiev.ua). Additionally, they can be sent by regular mail to Executive Managing Editor, Editorial Office, G. V. Kurdyumov Institute for Metal Physics, N.A.S. of Ukraine, 36 Academician Vernadsky Boulevard, UA-03142 Kyiv, Ukraine. Manuscripts may also be submitted to a member of the Editorial Advisory Board or to the appropriate Regional Editor who is familiar with the research presented.
Submission of a paper to '*Metallophysics and Advanced Technologies*' (transliteration: '*Metallofizika i Noveishie Tekhnologii*', *i.e.*, '*MfNT*') will be taken to imply that it represents original work not previously published, that it is not being considered for publication elsewhere, and that, if accepted for publication, it will not be republished without the consent of the Editors and Publisher. It is a condition of acceptance by the Editor of a manuscript for publication that the Publishers acquire automatically the copyright in the manuscript throughout the world. Journal '*MfNT*' supports the generally accepted principles described in documents on publication ethics and unacceptable practices, which are presented on the journal website.
Scope of the Journal: *Electronic Structure and Properties, Crystal-Lattice Defects, Phase Transformations, Physics of Strength and Plasticity, Metallic Surfaces and Films, Structure and Properties of Nanoscale and Mesoscopic Materials, Amorphous and Liquid States, Interactions of Radiation and Particles with Condensed Matter, Materials in Extremal Conditions, Reactor and Aerospace Metals Science, Medical Metals Science, New Metallic Materials and Synthetic Metals, Metal-Containing Smart Materials, Physical and Technical Basis of Experiment and Diagnostics, Articles under Discussion*.
Language: The language of publication may be English (preferably) or Ukrainian.
Abstract: Each paper requires an abstract of 200–250 words summarizing the significant coverage and findings (the use of mathematical symbols and expressions in abstract is not recommended).
Keywords and PACS numbers: 5–7 keywords and PACS numbers reflecting the content of the contribution should be supplied (see 'Physics and Astronomy Classification Scheme 2010').
Manuscript Preparation: Papers should be formatted according to the template, which can be downloaded from the Journal's website. The length of **research papers** should not in general exceed 5000 words and 10 figures; **review articles** should not exceed 10000 words and 30 figures, including tables and diagrams. Authors are urged to arrange the subject matter clearly under headings such as: 1. Introduction, 2. Experimental/Theoretical Details, 3. Results, 4. Discussion, 5. Conclusion, References. Subsections should be identified with section and subsection numbers (such as 6.1. Second-Value Subheading).
References and Notes: Notes are indicated in the text by consecutive superior Arabic numbers (without parentheses). References should be numbered consecutively (in square brackets) throughout the text. The full list should be collected and typed at the end of the paper in numerical order. Listed references should be completed in all details including **DOI** (if available) but excluding article titles in journals. **All authors'** initials should precede their names. Examples of references preparation:

1. S. O. Firstov and T. G. Rogul, *Metallofiz. Noveishie Tekhnol.*, **44**, No. 1: 127 (2022) (in Ukrainian). https://doi.org/10.15407/mfint.44.01.0127
2. V. B. Tarelnyk, O. P. Gaponova, and Ye. V. Konoplianchenko, *Prog. Phys. Met.*, **23**, No. 1: 27 (2022). https://doi.org/10.15407/ufm.23.01.027
3. A. Meisel, G. Leonhardt, and R. Szargan, *Röntgenspektren und Chemische Bindung* [X-Ray Spectra and Chemical Bond] (Leipzig: Akademische Verlagsgesellschaft Geest & Portig K.-G.: 1977) (in German).
4. J. M. Ziman, *Printsipy Teorii Tverdogo Tela* [Principles of the Theory of Solids] (Moscow: Mir: 1974) (Russian translation).
5. M. A. Stucke, D. M. Dimiduk, and D. M. Hazzledine, *High Temperature Ordered Intermetallic Alloys. V* (Eds. I. Baker and R. Darolia) (Pittsburgh, PA, USA: MRS: 1993), p. 471.
6. *Handbook of Mathematical Functions with Formulas, Graphs and Mathematical Tables* (Eds. M. Abramowitz and I. A. Stegun), Nat'l Bureau of Standards. Appl. Math. Ser. Vol. **55** (Washington, D.C.: U.S. Govt. Printing Office: 1964).
7. B. B. Karpovych and O. B. Borovkoff, *Proc. of Symp. 'Micromaterials Engineering' (Dec. 25–31, 1999)* (Kyiv: RVV IMF: 2000), vol. **2**, p. 113 (in Russian).
8. A. E. Krug, *Abstr. Int. Conf. Phys. Phenomena (Dec. 25–31, 1991, Alushta)* (Kharkiv: 1991), p. 12.
9. T. M. Radchenko, *Vplyv Uporyadkuvannya Defektnoyi Struktury на Transportni Vlastyvosti Zmishanykh Krystaliv* [Influence of Ordering of the Defect Structure on Transport Properties of the Mixed Crystals] (Thesis of Disser. for the Degree of Dr. Phys.-Math. Sci.) (Kyiv: G. V. Kurdyumov Institute for Metal Physics, N.A.S.U.: 2015) (in Ukrainian). https://doi.org/10.13140/RG.2.2.35430.22089

10. E. M. Gololobov, V. B. Shipilo, N. I. Sedrenok, and A. I. Dudyak, *Sposob Polucheniya Karbonitridov Metallov* [Production Method of Metal Carbonitrides], Authors' Certificate 722341 SSSR (Publ. November 21, 1979) (in Russian).
11. V. G. Trubachev, K. V. Chuistov, V. N. Gorshkov, and A. E. Perekos, *Sposob Polucheniya Metallicheskikh Poroshkov* [The Technology of Metallic Powder Production]: Patent 1639892 SU. MKI, B22 F9/02, 9/14 (Otkrytiya i Izobreteniya, **34**, No. 13: 11) (1991) (in Russian).
12. Yu. M. Koval' and V. V. Nemoshkalenko, *O Prirode Martensitnykh Prevrashcheniy* [On the Nature of Martensitic Transformations] (Kyiv: 1998) (Prepr./N.A.S. of Ukraine. Inst. for Metal Physics. No. 1, 1998) (in Russian).

Journal title abbreviations should conform to generally accepted styles:
https://www.cas.org/support/documentation/references/corejournals;
https://cdn.journals.aps.org/files/rmpguapb.pdf;
https://images.webofknowledge.com/WOK46P9/help/WOS/A_abrvjt.html;
https://mathscinet.ams.org/msnhtml/serials.pdf.

Equations and Formulae: Formulas in the text should be inserted by **MathType**, fully compatible with MS Office. Vectors should be typed in bold without arrows above. Note that complicated formulae, mathematical expressions or (de)notations are not recommended in the title, abstract, and keywords.

Tables: Number tables consecutively with Arabic numerals and give a clear descriptive caption at the top.

Figures: All figures should be numbered with consecutive Arabic numbers, have descriptive captions and be mentioned in the text. Keep figures separate at the end of the text and clearly label each figure with author's name and figure number. The labels at axis should contain the designation (or notation) of quantities and their units.

Preparation: Figures submitted must be of a high enough standard for reproduction with 300–600 dpi resolution (including half-tone illustrations). Redrawing or retouching of unusable figures will be charged to the authors.

Colour Plates: Whenever, the use of colour is an integral part of the research, or where the work is generated in colour, the Journal will publish (in paper version) the colour illustrations with charge to the author. Reprints in colour will carry a surcharge. Please write to the Publisher for details.

Submission of Electronic Text: Authors should submit the electronic version of their paper by e-mail to the Editorial Office. The text file should be saved in the native formats of the MS Word with a name consisting the name of the first author, for example, Hotovchenko.docx. The electronic form of figures (in TIF, EPS, JPG, PNG formats preferably and with name consisting the name of the first author also, for example, Hotovchenko_fig2a.jpg) should be planned so that they reduce to 12.7 cm column width (or less), and keep them separated from the text file. It is desirable to submit additionally all the **figures** within the format of the program, in which they were created.

Proofs: Contributors will receive page proofs for correction by e-mail as a PDF document. These must be returned to Kyiv office (mfint@imp.kiev.ua with subject beginning by word 'mfint') within 5 days of receipt.

Page Charges: There are no page charges to individuals or institutions.

Reprints: Authors can freely download a PDF version of their published article from journal website: https://mfint.imp.kiev.ua. The printed issues may be ordered by completing the appropriate form sent with proofs and prepaid by authors under the terms as for subscription.

Further Information: All questions arising during the **peer review** or after acceptance of manuscripts, especially those relating to reprints, should be directed to G. V. Kurdyumov Institute for Metal Physics, N.A.S. of Ukraine, Executive Managing Editor, Editorial Office, 36 Academician Vernadsky Blvd., UA-03142 Kyiv, Ukraine;
Fax: +380 44 4242561, e-mail: mfint@imp.kiev.ua (with subject beginning by word 'mfint').

We ask the authors to apply with their manuscript Copyright Transfer Agreement form.

Copyright Transfer Agreement

We, the undersigned authors of the manuscript '_____', transfer to the Founders, Publisher, and Editorial Board of the Journal 'Metallophysics and Advanced Technologies' (according to agreements between them) the right to publish this manuscript in original language or in translation to the other languages. We confirm that publication of this manuscript **will not** infringe a copyright of other persons or organizations and publication ethics.

Author(s):_____
(Last Name, First Name, Affiliation)

Correspondence Address:_____

Phone and e-mail: _____

_____ _____
(Signature) *(Date)*

ІНФОРМАЦІЯ (ПРАВИЛА) ДЛЯ АВТОРІВ

Науковий журнал «Металофізика та новітні технології» (МфНТ) щомісяця публікує статті, які раніше ще не публікувалися та не перебувають на розгляді для опублікування в інших виданнях. Статті мають містити результати експериментальних і теоретичних досліджень в області фізики та технологій металів, стопів і сполук з металічними властивостями; рецензії на монографії; інформацію про конференції, семінари; відомості з історії металофізики; рекламу нових технологій, матеріялів, приладів. Журнал дотримується загальноприйнятих принципів, зазначених на його сайті в документах з публікаційної етики та щодо неприйнятних практик.

Тематика журналу: *Електронні структура та властивості, Дефекти кристалічної ґратниці, Фазові перетворення, Фізика міцности та пластичности, Металічні поверхні та плівки, Будова та властивості наномасштабних і мезоскопічних матеріялів, Аморфний і рідкий стани, Взаємодії випромінення та частинок із конденсованою речовиною, Матеріяли в екстремальних умовах, Реакторне й авіакосмічне металознавство, Медичне металознавство, Нові металеві матеріяли та синтетичні метали, Металовмісні смарт-матеріяли, Фізико-технічні основи експерименту та діягностики, Дискусійні повідомлення*.

Статті публікуються однією з двох мов: англійською (віддається перевага) або українською.

Статті, в оформленні яких не дотримано наступних правил для опублікування в МфНТ, повертаються авторам без розгляду по суті. (Датою надходження вважається день повторного надання статті після дотримання зазначених нижче правил.)

1. Стаття має бути підписаною всіма авторами (із зазначенням їхніх адрес електронної пошти); слід вказати прізвище, ім'я та по батькові автора, з яким редакція буде вести листування, його поштову адресу, номери телефону та факсу й адресу електронної пошти.

2. Виклад матеріялу має бути чітким, **структурованим** (розділами, наприклад, «1. Вступ», «2. Експериментальна/Теоретична методика», «3. Результати та їх обговорення», «4. Висновки», «Цитована література»), стислим, без довгих преамбул, відхилень і повторів, а також без дублювання в тексті даних таблиць, рисунків і підписів до них. Анотація та розділ «Висновки» мають не дублювати один одного. Числові дані слід наводити в загальноприйнятих одиницях.

3. Об'єм оригінальної (неоглядової) статті має бути не більше 5000 слів (з урахуванням основного тексту, таблиць, підписів до рисунків, списку використаних джерел) і 10 рисунків. **Об'єм оглядової статті** — до 10000 слів та 30 рисунків.

4. За потреби до редакції може надаватися друкований (А4, подвійний інтервал) примірник рукопису з ілюстраціями.

5. До редакції обов'язково надається (по **e-mail**) файл статті, набраний у текстовому редакторі Microsoft Word, з назвою, що складається з прізвища першого автора (латиницею), наприклад, Hotovchenko.docx.

6. Електронна версія рукопису та його друкований варіянт (в разі його надання) мають бути ідентичними. Вони мають оформлюватися за шаблоном, який можна завантажити з сайту журналу, і містити 5–7 **індексів PACS** в редакції 'Physics and Astronomy Classification Scheme 2010'. Тексти статей мають також містити **назву статті**, **список авторів**, **повні назви** та **поштові адреси установ**, в яких вони працюють, **анотацію статті** (200–250 слів), **5–7 ключових слів** двома мовами (**англійською** та **українською**), а заголовки таблиць і підписи до рисунків мають подаватися **як мовою рукопису, так і англійською мовою**; англомовна анотація може бути представленою в більш розгорнутому варіянті (до 500 слів). Назва статті, її анотація та ключові слова мають не містити складні формули, математичні вирази чи позначення.

7. Електронні версії рисунків мають бути представленими у вигляді окремих файлів (у форматах TIF, EPS, JPG, PNG з розріженням у 300–600 dpi) з назвами, що складаються з прізвища першого автора (латиницею) та номера рисунка, наприклад, Hotovchenko_fig2a.jpg. Додатково рисунки надаються у форматі програми, в якій вони створювалися.

8. Написи на рисунках (особливо на півтонових) слід по можливості замінити літерними позначеннями (набраними на контрастному фоні), а криві позначити цифрами або різними типами ліній/маркерів, які мають бути роз'ясненими в підписах до рисунків або в тексті. На графіках усі лінії/маркери мають бути достатньої товщини/розміру для якісного відтворення їх у зменшеному в 2–3 рази вигляді (рекомендована початкова ширина рисунка — 12,7 см). Світлини мають бути чіткими та контрастними, а написи та позначення мають не закривати істотні деталі (для чого можна використовувати стрілки). Замість зазначення в підтекстовці збільшення під час зйомки бажано проставити масштаб (на контрастному фоні) на одній з ідентичних світлин. На графіках підписи до осей, **виконані мовою статті**, мають містити позначення (або найменування) величин, що відкладаються вздовж осей, і відділені комою їхні одиниці вимірювання.

9. Формули в текст треба вставляти за допомогою редактора формул **MathType**, сумісного з MS Office. **Вектори** слід набирати напівтовстим шрифтом без стрілок зверху.

10. Рисунки, таблиці, формули, а також підрядкові **примітки (виноски)** мають нумеруватися поспіль по всій статті.

11. Посилання на літературні джерела слід давати у вигляді порядкового номера, надрукованого в рядок у квадратних дужках. Список цитованої літератури складається почергово за першою згадкою джерела. Приклади оформлення посилань наведено нижче (просимо звернути увагу на порядок розташування ініціалів і прізвищ авторів, бібліографічних відомостей і на розділові знаки, а також на необхідність зазначення **всіх** співавторів цитованої роботи та її ідентифікатора **DOI**, якщо він є):

1. S. O. Firstov and T. G. Rogul, *Metallofiz. Noveishie Tekhnol.*, **44**, No. 1: 127 (2022) (in Ukrainian). https://doi.org/10.15407/mfint.44.01.0127
2. V. B. Tarelnyk, O. P. Gaponova, and Ye. V. Konoplianchenko, *Prog. Phys. Met.*, **23**, No. 1: 27 (2022). https://doi.org/10.15407/ufm.23.01.027
3. A. Meisel, G. Leonhardt, and R. Szargan, *Röntgenspektren und Chemische Bindung* [X-Ray Spectra and Chemical Bond] (Leipzig: Akademische Verlagsgesellschaft Geest & Portig K.-G.: 1977) (in German).
4. J. M. Ziman, *Printsipy Teorii Tverdogo Tela* [Principles of the Theory of Solids] (Moscow: Mir: 1974) (Russian translation).
5. M. A. Stucke, D. M. Dimiduk, and D. M. Hazzledine, *High Temperature Ordered Intermetallic Alloys. V* (Eds. I. Baker and R. Darolia) (Pittsburgh, PA, USA: MRS: 1993), p. 471.
6. *Handbook of Mathematical Functions with Formulas, Graphs and Mathematical Tables* (Eds. M. Abramowitz and I. A. Stegun), Nat'l Bureau of Standards. Appl. Math. Ser. Vol. **55** (Washington, D.C.: U.S. Govt. Printing Office: 1964).
7. B. B. Karpovych and O. B. Borovkoff, *Proc. of Symp. 'Micromaterials Engineering' (Dec. 25–31, 1999)* (Kyiv: RVV IMF: 2000), vol. **2**, p. 113 (in Russian).
8. A. Eh. Krug, *Abstr. Int. Conf. Phys. Phenomena (Dec. 25–31, 1991, Alushta)* (Kharkiv: 1991), p. 12.
9. T. M. Radchenko, *Vplyv Uporyadkuvannya Defektnoyi Struktury na Transportni Vlastyvosti Zmishanykh Krystaliv* [Influence of Ordering of the Defect Structure on Transport Properties of the Mixed Crystals] (Thesis of Disser. for the Degree of Dr. Phys.-Math. Sci.) (Kyiv: G. V. Kurdyumov Institute for Metal Physics, N.A.S.U.: 2015) (in Ukrainian). https://doi.org/10.13140/RG.2.2.35430.22089
10. E. M. Gololobov, V. B. Shipilo, N. I. Sedrenok, and A. I. Dudyak, *Sposob Polucheniya Karbonitridov Metallov* [Production Method of Metal Carbonitrides], Authors' Certificate 722341 SSSR (Publ. November 21, 1979) (in Russian).
11. V. G. Trubachev, K. V. Chuistov, V. N. Gorshkov, and A. E. Perekos, *Sposob Polucheniya Metallicheskikh Poroshkov* [The Technology of Metallic Powder Production]: Patent 1639892 SU. MKI, B22 F9/02, 9/14 (Otkrytiya i Izobreteniya, **34**, No. 13: 11) (1991) (in Russian).
12. Yu. M. Koval' and V. V. Nemoshkalenko, *O Prirode Martensitnykh Prevrashcheniy* [On the Nature of Martensitic Transformations] (Kyiv: 1998) (Prepr./N.A.S. of Ukraine. Inst. for Metal Physics. No. 1, 1998) (in Russian).

Слід використовувати загальноприйняті скорочення назв журналів:
https://www.cas.org/support/documentation/references/corejournals;
https://cdn.journals.aps.org/files/rmpguapb.pdf;
https://images.webofknowledge.com/WOK46P9/help/WOS/A_abrvjt.html;
https://mathscinet.ams.org/msnhtml/serials.pdf.

Необхідною вимогою є також надання авторами додаткового списку цитованої літератури (**References**) в **латинській транслітерації** (система **BGN/PCGN**; рекомендовані транслітератори: http://www.slovnyk.ua/services/translit.php; http://ru.translit.net/?account=bgn).

Після транслітерованих назв книг, дисертацій, патентів та ін. слід у квадратних дужках наводити їхній англомовний переклад (див. приклади вище). При транслітерації статей з МфНТ слід використовувати написання П.І.Б. авторів, наведені **лише** в англомовному змісті відповідного випуску, і **офіційну** транслітеровану назву журналу (див. також першу сторінку кожної статті та сайт).

12. Коректура авторам надсилається електронною поштою у вигляді pdf-файлу після завершення етапу **рецензування**. На перевірку коректури авторам відводяться 5 робочих днів. Після закінчення зазначеного терміну стаття автоматично направляється до друку. Виправлення слід відмітити та прокоментувати в самому pdf-файлі або оформити у вигляді переліку виправлень (підписаного уповноваженим представником колективу авторів) і переслати електронною поштою на адресу редакції.

Електронний варіянт статті надсилається на e-mail: mfint@imp.kiev.ua (з темою, що починається словом 'mfint'). Друкована версія рукопису (якщо у ній є потреба) надсилається за адресою: **Інститут металофізики ім. Г. В. Курдюмова НАН України, редакція МфНТ; бульвар Акад. Вернадського, 36; 03142 Київ, Україна** або відповідному реґіональному редактору (див. сайт).

Автори можуть вільно завантажити pdf-файли опублікованих статей з сайту журналу (https://mfint.imp.kiev.ua), а також замовити друковані примірники випуску журналу зі своєю статтею, надіславши до редакції журналу **разом з коректурою відповідну заявку та квитанцію про оплату** друку необхідної кількості примірників випуску на умовах, аналогічних передплатним.

Відповідно до угод між редакцією МфНТ, засновниками та видавцем журналу, редакція вважає, що автори, надсилаючи їй рукопис статті, передають засновникам, видавцю та редколеґії право опублікувати цей рукопис мовою ориґіналу та в перекладі іншими мовами, і просить авторів відразу прикладати до рукопису «Угоду про передачу авторського права».

Угода про передачу авторського права

Ми, що нижче підписалися, автори рукопису «_____», передаємо засновникам, видавцю та редколеґії журналу «Металофізика та новітні технології» (згідно з угодами між ними) право опублікувати цей рукопис мовою ориґіналу та в перекладі іншими мовами. Ми підтверджуємо, що ця публікація **не** порушує авторського права інших осіб або організацій і принципів наукової етики. При цьому за авторами зберігаються всі інші права як власників цього рукопису.

Підписи авторів: _____ (П.І.Б., дата, адреса, тел., e-mail)

Metallophysics and Advanced Technologies
Металофіз. новітні технол.
Metallofiz. Noveishie Tekhnol.
2025, vol. 47, No. 3, pp. 237–244
https://doi.org/10.15407/mfint.47.03.0237
Reprints available directly from the publisher

PACS numbers: 61.66.Dk, 61.72.Ff, 68.70.+w, 81.05.Bx, 81.30.Mh, 81.40.Cd, 81.40.Gh

Морфологія цементиту, сформованого в результаті розпаду аустеніту під час охолодження перегрітих заевтектоїдних криць

Ю. А. Гарасим, Н. О. Бондаревська

Інститут металофізики ім. Г. В. Курдюмова НАН України,
бульв. Академіка Вернадського, 36,
03142 Київ, Україна

Досліджено мікроструктуру низьколеґованих заевтектоїдних криць з різним вмістом Карбону (1,05, 1,28 та 1,78 мас.%) після нагріву їх до температур у 1150–1200°C і наступного охолодження з контрольованими швидкостями. Встановлено, що загальним для досліджуваних криць є виділення під час охолодження частинок вторинного цементиту по межах зерен колишнього гомогенного аустеніту. У внутрішніх об'ємах зерен аустеніту криці з 1,05 мас.% Карбону формується структура зернистого перліту, тоді як у криці з 1,28 мас.% Карбону — пластинчастого. В криці з вищим вмістом Карбону (1,78 мас.%) розпад аустеніту приводить до утворення структури з голкоподібними виділеннями Відманштеттового цементиту. Одержані результати можуть бути використані для розробки оптимальних режимів охолодження криць перлітного класу після стикового зварювання для запобігання утворенню в зонах термічного впливу структури зернистого перліту з нижчими характеристиками міцности.

Ключові слова: заевтектоїдна криця, Відманштеттів цементит, морфологія, пластинчаста структура, глобулярна структура, сфероїдизація.

Corresponding author: Julian Andriyovych Harasym
E-mail: garasym @imp.kiev.ua

G. V. Kurdyumov Institute for Metal Physics, N.A.S. of Ukraine,
36 Academician Vernadsky Blvd., UA-03142 Kyiv, Ukraine

Citation: J. A. Harasym and N. O. Bondarevs'ka, Morphology of Cementite Formed as a Result of Austenite Decomposition During Cooling of Overheated Hypereutectoid Steels, *Metallofiz. Noveishie Tekhnol.*, **47**, No. 3: 237–244 (2025).
DOI: 10.15407/mfint.47.03.0237

The microstructure of low-alloy hypereutectoid steels with different carbon content (1.05, 1.28 and 1.78 wt.%) after their heating to temperatures of 1150–1200°C and subsequent cooling at controlled rates is studied. As established, the segregation of particles of secondary cementite along the grain boundaries of former homogeneous austenite during cooling is common to the studied steels. In the inner volumes of austenite grains of steel with 1.05 wt.% carbon, a granular pearlite structure is formed, while, in steel with 1.28 wt.% carbon, a lamellar structure is formed. In steel with a higher carbon content (1.78 wt.%), the decomposition of austenite leads to the formation of a structure with needle-like precipitations of Widmanstätten cementite. The obtained results can be used in the development of optimal modes of cooling of pearlite grade steels after butt-welding to prevent the formation of a granular pearlite structure with lower strength characteristics in the thermally affected zones.

Key words: hypereutectoid steel, Widmanstätten cementite, morphology, lamellar structure, globular structure, spheroidization.

(Отримано 26 вересня 2024 р.; остаточн. варіянт — 14 листопада 2024 р.)

1. ВСТУП

Механічні властивості термозміцнених вуглецевих низьколеґованих криць контролюються не тільки об'ємним вмістом цементиту, але й його морфологією та характером розподілу в об'ємі [1]. В залежності від температурно-часових умов нагріву й охолодження в них може бути сформована структура з різною морфологією цементитних частинок. В процесі металурґійного виробництва прокату з даних криць під час охолодження на повітрі, зазвичай, утворюється структура пластинчастого перліту. Змінити морфологію цементитних виділень у перліті з пластинчастої на глобулярну, що особливо важливо для інструментальних і підшипникових криць, оскільки це сприяє приросту їхніх пластичности, тріщиностійкости та зносостійкости, вдається додатковим термічним обробленням — сфероїдизаційним відпалом [2]. З метою скорочення тривалости даного термічного оброблення в рамках моделю «анормального» механізму розпаду аустеніту авторами [2, 3] розроблено ефективні схеми сфероїдизаційного оброблення, які дають змогу синхронізувати тривалість технологічних операцій гарячого вальцювання та відпалу. Формування глобулярного перліту за повільного охолодження криць відбувається в місцях розташування недорозчинених під час гомогенізації аустеніту цементитних частинок. В разі хемічної гомогенности аустеніту, за відсутности в ньому недорозчинених частинок цементиту, зародження глобулярного цементиту, на думку авторів [2], може здійснюватися на скупченнях дислокацій, які утворилися в процесі термоциклічного оброблення.

Відмінний механізм формування структури глобулярного перлі-

ту в процесі охолодження аустеніту у вуглецевих крицях (так званого «diversed eutectoid transformation» — DET), був розроблений авторами [4]. Згідно з ним, формування структури глобулярного перліту здійснюється, в основному, безпосередньо на рухливій міжфазній γ→α-межі в процесі евтектоїдного перетворення аустеніту. Необхідною умовою реалізації такого механізму є наявність частинок цементиту діяметром > 0,3 мм і швидкости повільного охолодження ≤ 30 К·год$^{-1}$.

Перспективність використання швидкісних методів нагріву (наприклад, індукційного) в формуванні негомогенного аустеніту показано авторами [5].

Аналіза результатів досліджень, наведених у літературі, свідчить, що питання щодо домінувальної ролі пластинчастого перліту в формуванні зернистого перліту залишаються дискусійними та потребують подальших досліджень [6]. Крім того, у аналізі процесів сфероїдизації цементиту не враховуються теплові ефекти, які виникають за γ→α-перетворення та можуть впливати на кінетику процесів [7, 8].

Залишаються нез'ясованими питання, пов'язані з впливом вмісту Карбону на розвиток процесів розпаду гомогенного аустеніту у перегрітих вуглецевих крицях з крупнозернистою вихідною структурою.

Мета даної роботи — дослідити морфологію частинок цементиту, утворених в результаті розпаду гомогенного аустеніту за неперервного охолодження перегрітих вуглецевих заевтектоїдних криць з різним вмістом Карбону (1,05–1,78 мас.%).

2. МАТЕРІЯЛИ ТА МЕТОДИ ДОСЛІДЖЕНЬ

Досліджували вуглецеві низьколеґовані криці із заевтектоїдним вмістом Карбону — від 1,05 до 1,78 мас.%. Криці були витоплені індукційним методом у промислових умовах металурґійних заводів. Вміст леґувальних добавок (Mn, Si, Cu, Al) у крицях не перевищував 0,11 мас.%, а S і P — 0,01 мас.%. Шляхом гарячого вальцювання виливків з криць виготовляли листові полоси товщиною у 20–30 мм. Вихідна структура в гарячекатаних полосах криць — пластинчастий перліт з частинками надлишкового цементиту, які декорують межі зерен колишнього аустеніту. З листових полос механічним способом вирізали зразки розмірами 20×20×30 мм, які піддавалися термічному обробленню, що включало наступні операції (рис. 1):

– нагрів зразків криць до температури $t_н$ = 1150–1200°C ($t_н = Ac_m$ + 20–30°C для криці з 1,78 мас.% C) з наступною витримкою у 1,5–2 години для формування у крицях хемічно гомогенного аустеніту;

– контрольоване охолодження нагрітих зразків до температури у 700°C зі швидкістю $V_{ох.}$=3,5–3 К·хв.$^{-1}$, у подальшому — до 500°C зі

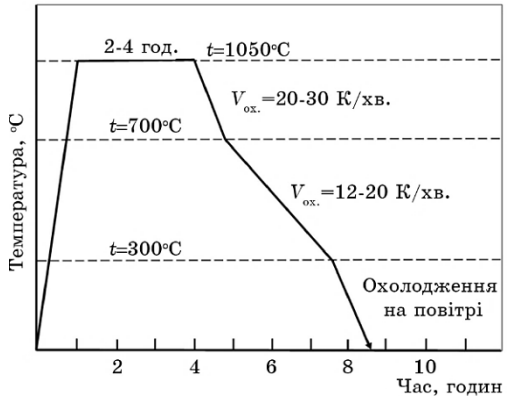

Рис. 1. Схема термічного оброблення криць.

Fig. 1. Scheme of heat treatment of steels.

швидкістю $V_{ох.}$=2–2,5 К·хв.$^{-1}$, а до кімнатної температури — на повітрі.

Для запобігання окисненню та зневуглецюванню поверхні зразків термічне оброблення здійснювалось у вакуумній печі ($P \cong 10^{-2}$ атм).

Металографічні дослідження поверхні зразків криць, підготовлених за допомогою стандартних методик і прощавлених розчином пікринової кислоти з добавками поверхнево-активних речовин, здійснювалися за допомогою оптичного мікроскопу Neophot-32. Для обчислення розміру (середнього діяметра) частинок цементиту всередині зерен колишнього аустеніту використовувалося програмне забезпечення Image-Pro Plus.

3. РЕЗУЛЬТАТИ ДОСЛІДЖЕНЬ ТА ЇХ ОБГОВОРЕННЯ

Мікроструктури досліджуваних криць, що містять 1,05, 1,28 та 1,75% С Карбону, після відпалу за схемою рис. 1 показано на рис. 2. Видно, що у практично однакових умовах відпалу в крицях формуються структури, які відрізняються, зокрема, морфологією цементитних частинок. Загальним для криць з 1,05 і 1,28% С є те, що розпад аустеніту в них розпочинається з виділення надлишкового Карбону у вигляді цементитної сітки по межах зерен колишнього аустеніту. Внаслідок цього, концентрація Карбону в решті об'єму аустеніту з пониженням температури охолодження поступово зменшується до евтектоїдного значення (рис. 3). Тобто за евтектоїдної температури у крицях була сформована структура аустеніт+вторинний цементит на межах зерен колишнього аустеніту. З подальшим охолодженням відбувається розпад решти об'єму аустеніту з практич-

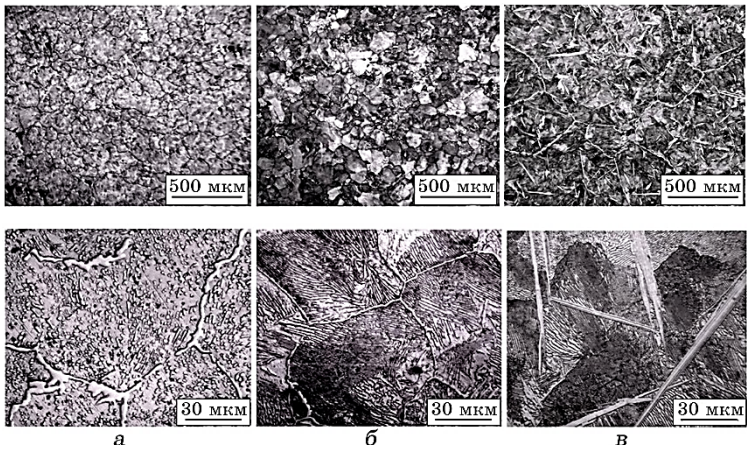

Рис. 2. Мікроструктури криць з вмістом Карбону у (мас.%) 1,05 (*а*), 1,28 (*б*) та 1,78 (*в*) після термічного оброблення.

Fig. 2. Microstructures of steels with carbon content (wt.%) of 1.05 (*a*), 1.28 (*b*) and 1.78 (*c*) after heat treatment.

но однаковим вмістом Карбону, близьким до евтектоїдного. Але, як свідчать результати металографічних досліджень, після охолодження криці з 1,05% С формується глобулярний перліт. Середній діяметер глобулярних цементитних частинок дорівнює $\cong 0{,}9$ мкм (рис. 4). Необхідно зауважити, що в структурі даної відпаленої криці спостерігається незначний вміст (< 10%) цементитних частинок, які зберігають пластинчасту форму, що може свідчити про незавершеність процесів їхньої сфероїдизації.

У крицях з вищим вмістом Карбону (1,14, 1,28 і 1,4%) — пластинчастий перліт. Причина виникнення відмінности в морфології цементиту, на наш погляд, пов'язана з додатковим розігрівом криці під час розпаду аустеніту та розвитком процесів сфероїдизації пластинчастого перліту. Формування у криці з 1,05% С глобулярного перліту може свідчити про розвиток в процесі охолодження процесів сфероїдизації пластинчастого цементиту. Відомо, що процес розпаду аустеніту в заевтектоїдних крицях супроводжується виділенням тепла, внаслідок чого спостерігається розігрів криці, температура якого контролюється, в першу чергу, об'ємом аустенітної фази, що зазнає фазового $\gamma \rightarrow \alpha$-перетворення. На можливість реалізації даної схеми перетворення пластинчастого цементиту в глобулярний в процесі охолодження заевтектоїдних криць вказується авторами [9]. Згідно з їхніми розрахунками, швидкість сфероїдизації збільшується з ростом температури нагріву за експоненційним законом, що сприяє інтенсифікації дифузійних процесів перерозподілу Карбону та формуванню глобулярного цементиту за двоста-

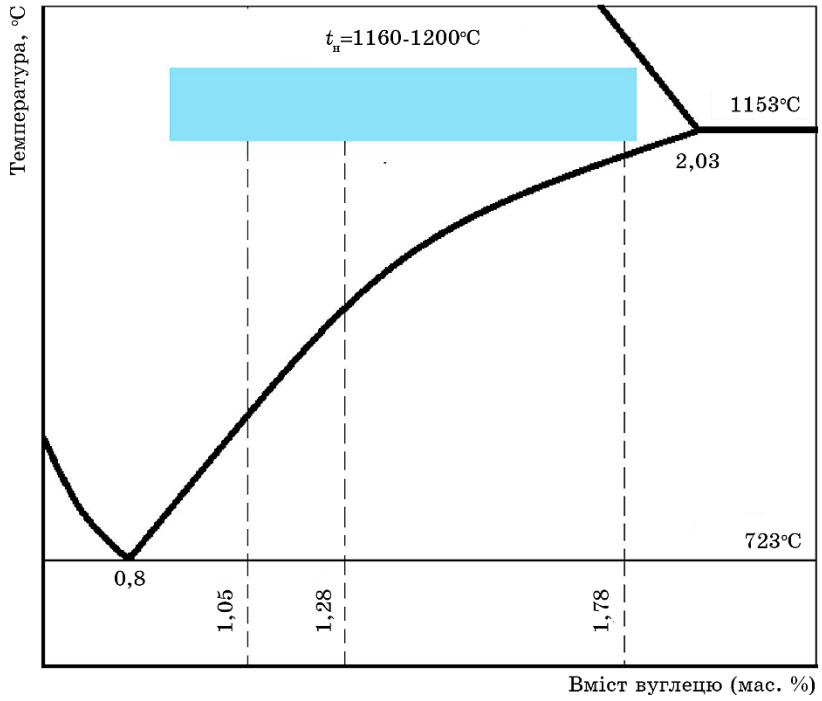

Рис. 3. Ділянка діяграми Fe–C із зазначеним положенням на ній досліджуваних криць.

Fig. 3. Section of the Fe–C diagram with the position of the studied steels on it.

дійною схемою. Спочатку в крицях утворюється пластинчастий перліт, який, внаслідок додаткового розігріву, що викликає розвиток сфероїдизаційних процесів, трансформується в глобулярний.

Із збільшенням вмісту Карбону в криці, а, значить, із зменшенням кількости аустенітної фази, що зазнає розпаду, виділеної теплової енергії недостатньо для розігріву криці. Внаслідок цього сфероїдизаційні процеси не розвиваються і пластинчаста форма цементиту залишається без змін, що і спостерігається за відпалу криць із вмістом Карбону більше 1,05%.

На відміну від криць з меншим (1,05 і 1,28%) вмістом Карбону в даних умовах відпалу в криці з 1,78% С формується структура, показана на рис. 3. В процесі охолодження від 1160°С внаслідок розпаду аустеніту відбувається виділення вторинного Відманштеттового цементиту не тільки по межах колишніх аустенітних зерен, а й у внутрішніх їхніх об'ємах. Середня товщина виділень цементиту — 2–5 мкм. Виділення мають ламінатну структуру та складаються з пластин цементиту товщиною у $\cong$ 0,3–0,5 нм з різною кристалог-

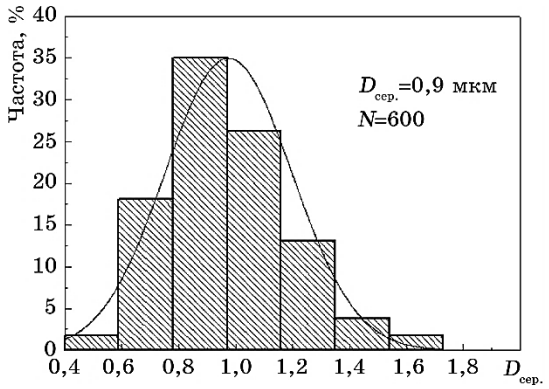

Рис. 4. Гістограма розподілу середнього діяметру глобул цементиту в термообробленій криці з 1,05% С.

Fig. 4. Histogram of the distribution of the average diameter of cementite globules in heat-treated steel with 1.05% C.

рафічною орієнтацією [10].

Необхідно зауважити, що, на відміну від Відманштеттового фериту в доевтектоїдних крицях, процеси формування Відманштеттового цементиту досліджено недостатньо повно. Вплив таких взаємозв'язаних чинників, як величина зерна аустеніту, швидкість охолодження, вміст Карбону, на формування Відманштеттових виділень (фериту, вторинного цементиту) докладно описано авторами [11]. Наявність у вуглецевих крицях виділень Відманштеттового цементиту тягне за собою погіршення пластичних характеристик криць, особливо в умовах динамічних навантажень. Вирішення проблеми впливу Відманштеттових виділень на розвиток процесів їхньої сфероїдизації потребує додаткових досліджень.

На підставі результатів дослідження морфології цементиту в заевтектоїдних вуглецевих крицях можуть бути надані рекомендації щодо режиму охолодження їх під час стикового зварювання залізничних рейок з метою запобігання формуванню в зоні термічного впливу структури зернистого перліту [12].

4. ВИСНОВКИ

1. Встановлено, що вміст Карбону в заевтектоїдних вуглецевих крицях, а, відповідно, об'ємна доля аустеніту, що зазнає евтектоїдного $\gamma \rightarrow \alpha$-перетворення, здатні впливати на морфологію цементиту.
2. Показано, що в процесі охолодження криць, попередньо нагрітих до 1200–1150°С з витримкою у 2–3 години, до 700°С на межах зерен колишнього аустеніту відбувається виділення вторинного цементи-

ту, які декорують межі.
3. Формування зернистого перліту у внутрішніх об'ємах аустенітних зерен під час охолодження криці з 1,05% Карбону, можливо, пов'язане з розвитком процесів сфероїдизації пластинчастого цементиту, зумовлених додатковим підвищенням температури за рахунок теплового ефекту евтектоїдного розпаду аустеніту.
4. Допускаємо, що відсутність розвитку сфероїдизаційних процесів у крицях з більшим вмістом Карбону, а, відповідно, об'ємним вмістом аустеніту, пов'язана з недостатнім розігрівом криць.

ЦИТОВАНА ЛІТЕРАТУРА–REFERENCES

1. В. М. Счастливцев, А. А. Мирзаев, И. Л. Яковлева, *Перлит в углеродистых сталях* (Екатеринбург: 2006); V. M. Schastlivtsev, A. A. Mirzaev, and I. L. Yakovleva, *Perlit v Uglerodistykh Stalyakh* [Pearlite in Carbon Steels] (Ekaterinburg: 2006) (in Russian).
2. Н. Е. Долженков, *Теория и практика металлургии*, **2**: 30 (2008); N. Ye. Dolzhenkov, *Teoriya i Praktika Metallurgii*, **2**: 30 (2008) (in Russian).
3. В. В. Парусов, И. И. Долженков, В. И. Сухомлин, *Металловедение и термическая обработка металлов*, № 6: 6 (1985); V. V. Parusov, I. I. Dolzhenkov, and V. I. Sukhomlin, *Metal Science and Heat Treatment*, № 6: 6 (1985) (in Russian).
4. J. D. Verhoven and E.D. Gibson, *Metall. Mater. Trans. A*, **25**, No. 4:1180 (1998).
5. К. З. Шепеляковский, А. Г. Спектор, А. Н Кузнецов, *Металловедение и термическая обработка металлов*, № 1: 62 (1978); K. Z. Shepelyakovsky, A. G. Spektor, and A. N Kuznetsov, *Metal Science and Heat Treatment*, No. 1: 62 (1978) (in Russian).
6. А. А. Баранов, А. П. Геллер, В. Г. Конарев, *Металловедение и термическая обработка металлов*, № 6: 11 (1985); A. A. Baranov, A. P. Geller, and V. G. Konarev, *Metal Science and Heat Treatment*, No. 6: 11 (1985) (in Russian).
7. Л. Е. Попов, А. А. Попов, *Справочник термиста* (Москва: Металлургия: 1991); L. E. Popov and A. A. Popov, *Spravochnik Termista* [Heat-Treater's Handbook] (Moskva: Metallurgiya: 1991) (in Russian).
8. В. А. Луценко, В. А. Маточкина, О. В. Луценко, *Металлургическая и горнорудная промышленность*, № 4: 234 (2006); V. A. Lutsenko, V. A. Matochkina, and O. V. Lutsenko, *Metallurgicheskaya i Gornorudnaya Promyshlennost'*, № 4: 234 (2006) (in Russian).
9. В. В. Шкатов, А. П. Чернышов, *Физ. мет. металовед.*, № 10: 169 (1991); V. V. Shkatov and A. P. Chernyshov, *Fiz. Met. Metalloved.*, No. 10: 169 (1991) (in Russian).
10. I. A. Bataev, A. A. Bataev, V. G. Burov, Ya. S. Lizunkova, and E. E. Zakharevich, *Steel Trans.*, **38**, No. 8: 684 (2008).
11. Р. П. Тодоров, Х. Г. Христов, *Металловедение и термическая обработка металлов*, № 2: 3 (2004); R. P. Todorov and H. G. Khristov, *Metal Science and Heat Treatment*, No. 2: 3 (2004).
12. L. Pintol, N. Goldenstein, and H. Goldenstein, *The Minerals, Metals & Materials Society*, **71**: 815 (2019).

Metallophysics and Advanced Technologies
Металофіз. новітні технол.
Metallofiz. Noveishie Tekhnol.
2025, vol. 47, No. 3, pp. 245–256
https://doi.org/10.15407/mfint.47.03.0245
Reprints available directly from the publisher

PACS numbers: 61.05.cp, 61.66.Dk, 61.72.Ff, 81.05.Bx, 81.30.Bx, 81.70.Jb, 81.70.Pg

Development of a Titanium Aluminide Alloy of Optimal Composition by Means of Modification

O. B. Halienkova[*], V. S. Yefanov[**], O. V. Zavgorodniy[***], I. M. Kirian[****], S. O. Bulish[***], O. D. Rud[****]

**SE "Ivchenko-Progress",*
2, Ivanova Str.,
UA-69068 Zaporizhzhia, Ukraine
***Ukrainian State University of Science and Technology (USUNT),*
2, Lazaryana Str.,
UA-49010 Dnipro, Ukraine
****National University "Zaporizhzhia Polytechnic",*
64, Zhukovsky Str.,
UA-69063 Zaporizhzhia, Ukraine
*****G. V. Kurdyumov Institute for Metal Physics, N.A.S. of Ukraine,*
36 Academician Vernadsky Blvd.,
UA-03142 Kyiv, Ukraine

Alloys based on γ-aluminide are a promising class of heat-resistant materials for the manufacture of parts of modern aircraft engines, the maximum operating temperature of which is in the range of 600–700°C. The main advantages of these alloys are the combination of low density, high structural stability, and heat resistance. However, due to the natural characteristics of intermetallic compounds (structure ordering, strong covalent bonding), γ-alloys are characterized by low plasticity compared to traditional titanium alloys that complicates the industrial application of these alloys and increases the complexity of the process of manufacturing semi-finished products and final parts. For the successful use of γ-alloys and their introduction into

Corresponding author: Oleksandr Rud
E-mail: rud@imp.kiev.ua

Citation: O. B. Halienkova, V. S. Yefanov, O. V. Zavgorodniy, I. M. Kirian, S. O. Bulish, and O. D. Rud, Development of a Titanium Aluminide Alloy of Optimal Composition by Means of Modification, *Metallofiz. Noveishie Tekhnol.*, **47**, No. 3: 245–256 (2025), DOI: 10.15407/mfint.47.03.0245

modern aircraft engines, it is necessary to increase their technological plasticity, while ensuring high strength and heat resistance characteristics. One of the most effective ways to accomplish this task is by means of alloying and modification. The work considers the influence of alloying elements niobium and molybdenum, as well as the modifying element rhenium, on the morphology, phase composition and mechanical characteristics of the γ-alloy in the Ti–Al system. The optimal concentrations of the elements Nb, Mo and Re in the titanium aluminide-based Ti–29Al–7Nb–2Mo alloy are determined, ensuring a two-fold increase in the mechanical properties of the alloy due to the weakening of covalent bonding forces. Using the method of high-temperature thermal analysis, it is established that the introduction of niobium, molybdenum and rhenium into the intermetallic does not change the sequence of transformations and the temperature ranges of phase-regions existence.

Key words: titanium aluminides, modifiers, phase composition, x-ray microanalysis, x-ray phase analysis.

Стопи на основі γ-алюмініду є перспективним класом жароміцних матеріялів для виготовлення деталів сучасних авіаційних двигунів, максимальна робоча температура яких лежить у діяпазоні 600–700°C. Головними перевагами цих стопів є поєднання низької густини, високої структурної стабільности, жароміцности. Однак, у зв'язку з природніми особливостями інтерметалідних сполук (впорядкованість структури, сильний ковалентний зв'язок), γ-стопам притаманна низька пластичність порівняно із традиційними титановими стопами, що ускладнює промислове освоєння цих стопів і підвищує трудомісткість процесу виготовлення напівфабрикатів і кінцевих деталів. Для успішного використання γ-стопів і впровадження в сучасні авіаційні двигуни необхідно підвищити їхню технологічну та конструкційну пластичність з одночасним забезпеченням високих характеристик міцности та жароміцности. Один з найбільш ефективних способів виконання цього завдання досягається шляхом леґування та модифікування. В роботі розглянуто вплив леґувальних елементів Ніобію та Молібдену та модифікувального елементу Ренію на морфологію, фазовий стан і механічні характеристики γ-стопу системи Ti–Al. Визначено оптимальні концентрації елементів Nb, Mo та Re у стопі на основі алюмініду Титану Ti–29Al–7Nb–2Mo, що забезпечують підвищення рівня механічних властивостей стопу у 2 рази за рахунок послаблення сил ковалентного зв'язку із введенням Молібдену та Ніобію та зміни морфології за рахунок поверхнево-активної дії модифікатора. З використанням методи високотемпературної термічної аналізи встановлено, що введення Ніобію, Молібдену та Ренію в інтерметалідний стоп не змінює послідовність перетворень і температурні діяпазони існування фазових областей.

Ключові слова: алюмініди Титану, модифікатори, фазовий склад, мікроаналіза, рентґенофазова аналіза.

(Received 2 February, 2025; in final version, 11 March, 2025)

1. INTRODUCTION

Titanium aluminide-based alloys, or γ-alloys, are one of the most promising materials for producing blades for new-generation gas turbine engines. Compared to other structural materials used in the aviation industry, the most important advantages of aluminide-based alloys are low density, high specific strength and modulus of elasticity, and high structural stability. The main forming technology for the production of titanium aluminide parts is casting technology [1–5], which is the most economical production process for obtaining products of complex shape. The microstructure of casting products is characterized by a coarse-grained structure, because of which they will be inferior in properties to products obtained, for example, by deformation or additive technologies [6].

To date, the largest numbers of studies on the influence of parameters and type of structure on mechanical properties are carried out on fourth-generation titanium aluminide alloys [7–9]. These alloys contain modifiers for the formation of an equilibrium lamellar structure with a small colony size, which provides high heat resistance and sufficient values of plasticity and fracture toughness.

The main direction of modification is the use of surface-active elements, the mechanism of action of which is adsorption on the surface of grains, which contributes to the change in the surface activity of crystals and the diffusion rate and leads to a change in the shape and size of crystals [10, 11]. The main criterion for choosing a surface-active modifier is low solubility in the lattice of the base metal, *i.e.*, titanium.

Lanthanides and rare earth elements are used as modifiers in titanium alloys – Sc, Y, B, La, Ce, Nd, Dy, *etc.*, the most effective and widely used of which are B and Y, Re is less commonly used [12–14]. Low boron content significantly changes the microstructure and properties. Since the atomic radius of boron (0.91 Å) differs from that of titanium (1.46 Å), at a boron content of more than 0.10%, compounds TiB, Ti_3B_4, TiB_2 are formed in the form of a coarse-needle framework along the grain boundaries, which reduces plasticity [15]. Therefore, the optimal B content is important, ensuring refinement of the structure and at the same time uniform distribution of boride release.

Yttrium has favourable thermodynamic characteristics, which allows it to influence the structure of titanium alloys [16]. Yttrium does not dissolve in titanium due to the large difference in their atomic radii [17]. Having a greater affinity for oxygen than titanium and a number of other elements, yttrium reacts with elements at grain boundaries.

Rhenium lowers the polymorphic transformation temperature of titanium. At rhenium concentrations up to 0.6%, the hardness of tita-

nium increases more than two-fold [18]. Because the difference in atomic radii with Ti is only 6.6%, rhenium has a higher solubility in titanium than yttrium. However, there is currently insufficient information on the influence of rhenium on the morphology, phase state and mechanical characteristics of γ-alloys.

Therefore, the work investigates the effect of Rhenium concentration at the level of 0.2–0.3% on the structure and properties of the Ti–29Al–7Nb–2Mo alloy based on titanium-aluminide intermetallic compound.

2. MATERIALS AND METHODS

The object of study in this work was titanium aluminide ingots of the composition Ti–29%Al alloyed with molybdenum and niobium, followed by modification of the alloy with rhenium. To study the influence of microadditions of the modifying element on the structure formation of the cast material, ingots of different compositions were melted in a vacuum arc furnace in a copper crystallizer using a non-consumable tungsten electrode. The ingots had the shape of washers with a diameter of 65–70 mm, a thickness of ≅ 12 mm, and a weight of ≅ 200 g.

The limiting concentration of Rhenium was selected based on the analysis of literature data, which indicate that the optimal content of modifying elements in alloys based on titanium aluminide is no more than 0.2…0.4% [10, 12, 13]. At higher content of modifying elements, the efficiency of cast grains refinement in general decreased. Therefore, the limiting concentration of rhenium content was selected at the level of 0.2–0.3%.

The chemical compositions of alloys were studied by the spectral reference-free method on an energy-dispersive x-ray fluorescence analyser “Expert 3L”. Etching of samples for metallographic studies was performed in the “Titan” reagent with the composition $HF:HNO_3:H_2O = 1:2:6$. The assessment of the template macrostructure was carried out with the naked eye along the thickness of the ingot. The study of the microstructure of the ingot material was performed using an optical microscope “AxioObserver 5” at magnifications of ×25...200. The study of the structure and distribution of alloying elements at higher magnifications was performed on a JEOL JSM IT-300 scanning electron microscope equipped with an Oxford Instrument X-Max80 x-ray spectral energy-dispersive microanalysis system.

Mechanical properties for tensile testing were determined according to DSTU ISO 6892 1:2019. Samples for testing were cut in the transverse direction to the ingot axis. Registration of diffractograms was carried out on a DRON-4 diffractometer in the Bragg–Brentano geometry with a MoK_α radiation in the angle range from 5° to 60° with a step

of 0.05° and an exposure of 4 s at each point. Differential thermal analysis was carried out on an automated analyser manufactured in the G. V. Kurdyumov Institute for Metal Physics of the N.A.S. of Ukraine in a helium atmosphere with a heating rate of 20 K/min.

3. RESULTS AND DISCUSSION

The chemical composition and mechanical properties of the obtained ingots are given in Tables 1 and 2, respectively. The alloy of the base composition Ti–29Al (alloy No. 1) belongs to the first generation titanium aluminide based alloys and has low strength and almost zero ductility (Table 2). The production of ingots of the Ti–29Al–7Nb–2Mo alloy (alloy No. 2), which belongs to the fourth generation alloys, involves the use of double remelting. During the first remelting, refractory alloying elements (niobium and molybdenum) are introduced into the alloy. During the second remelting, aluminium is added to the resulting ingot, taking into account evaporation losses. This allows minimizing aluminium losses and ensuring guaranteed dissolution of refractory alloying elements and uniform distribution over the ingot cross-section.

From the analysis of Table 2, it is determined that when niobium and molybdenum are introduced into the alloy, an increase in mechanical properties is achieved by weakening the covalent bond between Titanium and aluminium atoms. The increase in strength and ductility for the alloy with rhenium is likely associated with a change in the morphology of the initial alloy.

Qualitative and quantitative phase analysis of the alloys was performed using x-ray diffractometry (Fig. 1). It was found that regardless of the change in chemical composition, the main phase content is unchanged and corresponds to a mixture of α_2- and γ-compounds in different ratios (Table 2). The base alloy has a higher percentage of α_2-phase, and with the introduction of β-stabilizers and a modifier, the content of γ-phase increases, which leads to an increase in plasticity characteristics. This is due to the formation of a slightly distorted lattice of the γ-phase due to alloying with niobium and molybdenum [6, 19], as well as due to a change in the shape and size of the structural

TABLE 1. Chemical composition of alloys.

Alloy No.	System	Element content, wt. %					
		Al	Nb	Mo	O	Ti	Re
1	Ti–29Al	29.4	–	–	0.12	base	–
2	Ti–29Al–7Nb–2Mo	28.7	7.4	2.1	0.13	base	–
3	Ti–29Al–7Nb–2Mo–0.2Re	32.7	7.6	1.31	–	base	0.27

TABLE 2. Phase composition and mechanical properties of alloys.

Alloy No.	Phase composition of the alloy		σ_u, MPa	δ, %
	α_2	γ		
1	77	23	230	–*
2	16	84	385	0.4
3	14	86	510	0.6

*not determined due to the high fragility of the sample.

components of the alloy with the introduction of rhenium. The increase in the percentage of γ-phase with the introduction of niobium and molybdenum allows us to assert the action of the above elements as γ-stabilizers.

The macro- and microstructures of the alloys are shown in Figs. 2 and 3. Comparison of the macrostructure of alloys of different compositions clearly demonstrates the influence of modifiers on changing its morphology. Thus, the macrostructure of the original Ti–29Al alloy consists of large grains of irregular shape of different sizes (Fig. 2*a*), the Ti–29Al–7Nb–2Mo alloy with niobium and molybdenum consists of large shiny grains with a clear boundary, corresponding to 8–9 points on the 10-point scale of macrostructures of titanium alloys [20] (Fig. 2*b*). The introduction of rhenium in an amount of 0.2% led to the

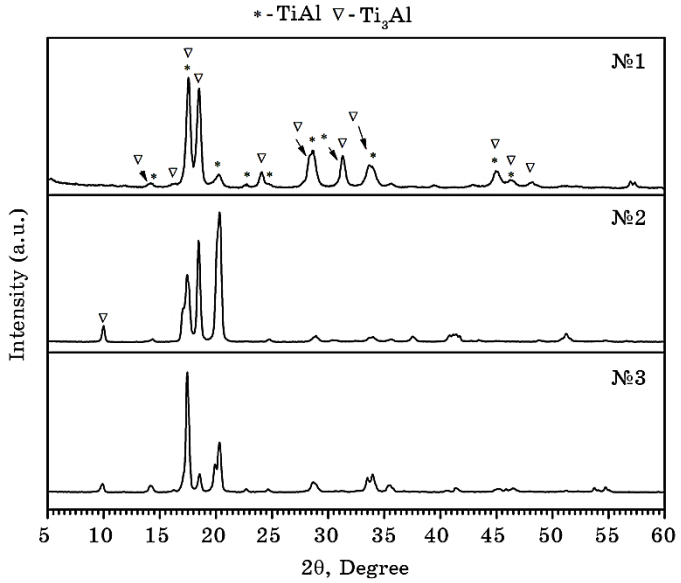

Fig. 1. XRD patterns of alloys: No. 1—Ti–29Al, No. 2—Ti–29Al–7Nb–2Mo, No. 3—Ti–29Al–7Nb–2Mo–0.2Re.

Fig. 2. Macrostructure of alloys after etching: *a*—alloy No. 1, *b*—alloy No. 2, *c*—alloy No. 3.

formation of a macrostructure of 5 points (Fig. 2*c*).

Metallographic study of ingots (Fig. 3) revealed that the microstructure of alloys is characterized by a lamellar structure consisting of a two-phase mixture of ($\alpha_2+\gamma$) phases. The complex introduction of alloying elements and modifier led to a significant change in the morphology of the structural components of alloys compared to the structure of the initial composition.

The microstructures of Ti–29Al and Ti–29Al–7Nb–2Mo alloys (Fig. 3*a*, *b*) are typical for the cast state of titanium alloys, *i.e.*, coarse-grained, characterized by large grains, the internal volume of which is represented by colonies of plates (lamellas) of α_2- and γ-phases, disoriented within one grain. The length of the plates is 100–400 μm, the thickness is 5–15 μm.

When rhenium is introduced into alloy No. 2 in an amount of 0.2% (Fig. 3*c*), the colonies of ($\alpha_2+\gamma$)-phase plates are oriented in a single direction within one grain. In addition, there is a thinning of the structural components of the ingot to 2–3 μm and a reduction in the length of the plates to 100–250 μm, which in turn contributes to an increase in the strength limit of the alloy by 1.5 times compared to the initial

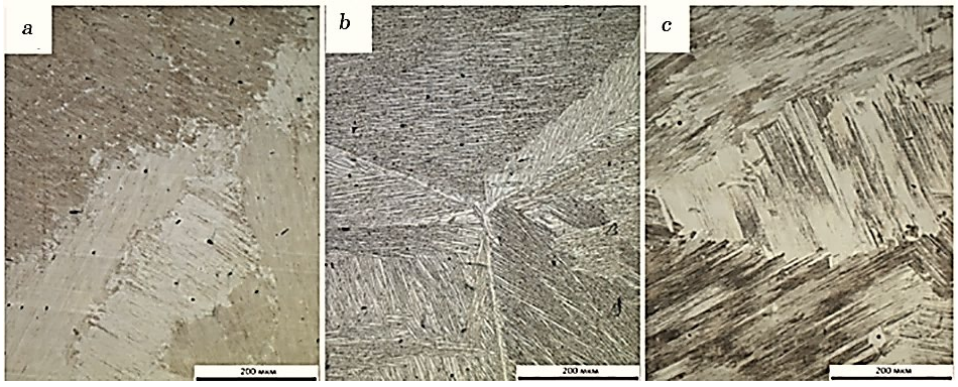

Fig. 3. Microstructure of alloys: *a*—alloy No. 1, *b*—alloy No. 2, *c*—alloy No. 3.

data.

To determine the uniformity of the distribution of the main alloying elements across the cross-section of ingots of the Ti–29Al, Ti–29Al–7Nb–2Mo, and Ti–29Al–7Nb–2Mo-0.2Re alloys, x-ray spectral microanalysis (XSMA) was performed in the mapping mode (Fig. 4).

Thus, the light areas of the structure are depleted in aluminium, while the dark areas, on the contrary, are enriched. According to the stoichiometric composition of the intermetallics Ti_3Al (α_2-phase) and TiAl (γ-phase) and the solubility limit of aluminium in the correspond-

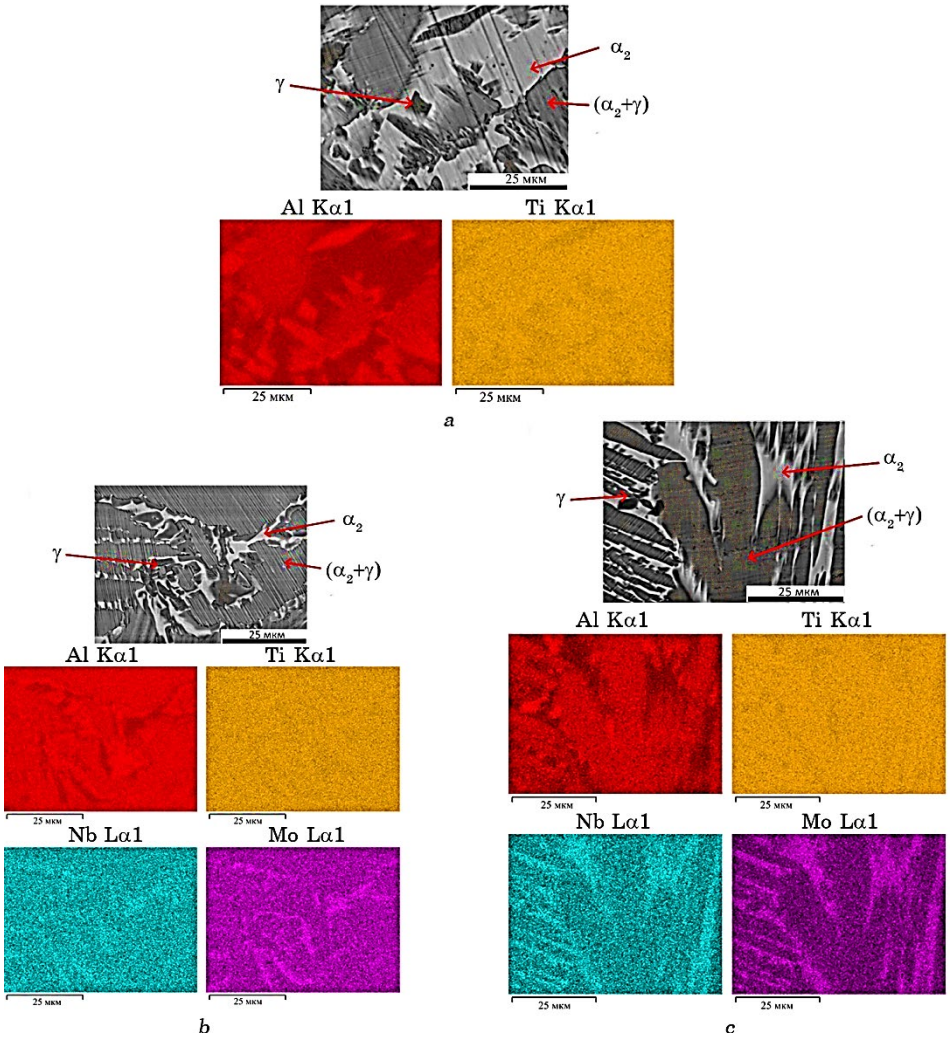

Fig. 4. X-ray spectral microanalysis of alloys in mapping mode: *a*—alloy No. 1, *b*—alloy No. 2, *c*—alloy No. 3.

ing compounds according to the phase diagram [21], the light areas of the structure can be classified as α_2-phase, the dark areas as γ-phase. The results of XSMA correlate with x-ray phase analysis, which shows a higher percentage of γ-phase in the composition of alloy No. 3 (Table 2).

According to the Ti–Al phase diagram (Fig. 5), the phase composition of the alloys at room temperature corresponds to a mixture of compounds α_2 (Ti_3Al)+γ (TiAl).

In terms of the content of molybdenum and niobium, more intense colours in Fig. 4 correspond to the areas of the α_2-phase. From the solubility graph of alloying elements in Ti_3Al and TiAl intermetallics [22], it is established that the solubility of β-stabilizers is greater in the γ-phase lattice: the solubility limit of molybdenum in the Ti_3Al lattice is no more than 1.5 at.%, in the TiAl lattice, it is of about 9 at.%; the solubility limit of niobium is of 12 at.% and 28 at.% for α_2- and γ-phases, respectively. That is, the content of molybdenum and niobium in the alloys is close to the solubility limit of the specified elements in the α_2-phase.

The high-temperature differential thermal analysis was used to study the thermal effects observed during continuous heating of samples from the experimental alloys (Fig. 6). Comparison of the curves with the Ti–Al diagram allows us to state that the endoeffects in the temperature range of 1110–1200°C are due to the transition of the ordered α_2-phase into the disordered α-phase with the h.c.p. lattice by the reaction $\alpha_2+\alpha \rightarrow \alpha+\gamma$ with subsequent transition to the single-phase α-region. Thermal effects in the temperature range of 1200–1300°C are not confirmed in the diagram and may be associated with the oxidation of the samples during heating or the process of separation of secondary

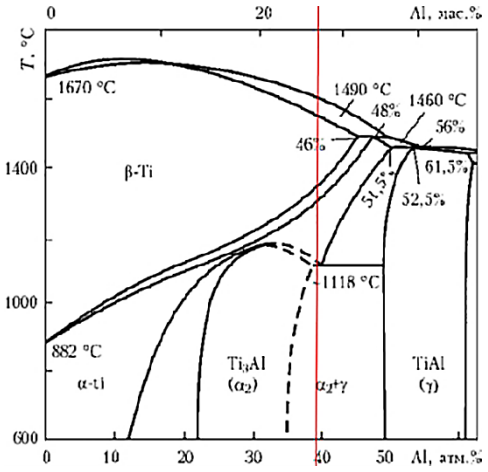

Fig. 5. Ti–Al phase diagram with a plotted line of chemical composition (in terms of aluminium content) of the studied alloys [21].

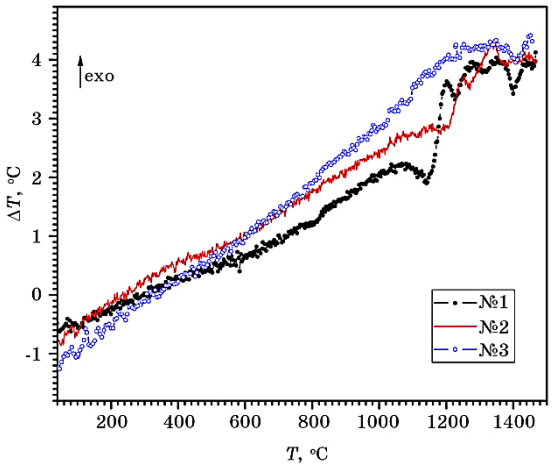

Fig. 6. Thermograms of alloys: No. 1—Ti–29Al, No. 2—Ti–29Al–7Nb–2Mo, No. 3—Ti–29Al–7Nb–2Mo–0.2Re.

phases. The following endoeffects at a temperature of 1350–1400°C are associated with the transition to the β-region, *i.e.*, a polymorphic transformation occurs. Thermal effects observed up to 1100°C, according to [23, 24], can be caused by the ordering-disordering processes occurring in intermetallic phases. Thus, it is determined that the introduction of alloying and modifying elements into an intermetallic alloy does not change the sequence of transformations and the temperature ranges of the existence of phase regions.

Thus, it has been established that alloys based on titanium aluminide of the Ti–29Al system are characterized by low ductility due to the structural features of the intermetallic compound. The introduction of alloying elements, in this case molybdenum and niobium, contributes to the improvement of the mechanical characteristics of the alloy by weakening the covalent bond between titanium and aluminium atoms. The addition of molybdenum and niobium to the Ti–29Al alloy improves the mechanical characteristics of the alloy by weakening the covalent bond between titanium and aluminium atoms. Due to the introduction of the modifying element rhenium into the alloy, the strength is increased to 510 MPa, which is 1.5 times higher compared to the data for the Ti–29Al–7Nb–2Mo system, and the plasticity is increased to 0.6%. The increase in mechanical characteristics due to the modification is achieved by changing the morphology of the structural components of the alloy; the coarse-grained structure of the original alloys with the length of the α_2- and γ-phase plates of 100–400 μm has changed to thinner lamellae with a thickness of up to 2–3 μm and a length of up to 250 μm.

According to x-ray phase analysis, the phase composition of the al-

loys corresponds to a mixture of α_2- and γ-phases in different percentage ratios. In the alloy of the basic composition Ti–29Al, the content of the α_2-phase prevails, with complex alloying and modification in the phase composition of the alloys, the γ-phase with higher values of plastic characteristics prevails. Thus, the introduction of a modifying element does not lead to a change in the phase composition of the alloy, but contributes to an increase in mechanical properties by changing the morphology of the structural components.

4. CONCLUSIONS

1. The optimal concentrations of alloying elements Nb, Mo and modifying element Re in an alloy based on titanium aluminide system have been determined, which ensure an increase in the mechanical properties of the Ti–29Al–7Nb–2Mo-0.2Re alloy.
2. The mechanisms of influence of alloying (molybdenum, niobium) and modifying (rhenium) elements on the structure and properties of the titanium aluminide based alloy have been established: increased plasticity is achieved by weakening the covalent bond forces upon the introduction of molybdenum and niobium and by changing the morphology of the structure due to the surface-active action of the modifiers.
3. Based on the data of x-ray phase analysis, it was established that alloying with molybdenum and niobium leads to a change in the phase ratio in the alloy based on titanium aluminide. In unalloyed aluminide, the content of α_2-phase prevails (up to $\cong$ 77%). After introducing niobium, molybdenum and rhenium, the alloy mainly consists of γ-phase ($\cong$ 84%) and a small amount of α_2-phase ($\cong$ 16%). This phase ratio results in increase in mechanical characteristics up to 1.5 times compared to the properties of unalloyed titanium aluminide.
4. By the method of high-temperature thermal analysis, it was established that the introduction of niobium, molybdenum and rhenium into the intermetallic alloy does not change the sequence of transformations and the temperature ranges of existence of phase regions.
5. The obtained level of properties allows us to consider the Ti–29Al–7Nb–2Mo–0.2Re alloy for use as a material for aircraft products.

REFERENCES

1. X. F. Ding, J. P. Lin, L. Q. Zhang, H. L. Wang, G. J. Hao, and G. L. Chen, *J. Alloys Compd.*, **506**: 115 (2010).
2. S. V. Akhonin, V. O. Berezos, O. M. Pikuly, A. Yu. Severyn, O. O. Kotenko, M. M. Kuzmenko, L. D. Kulak, and O. M. Shevchenko, *Modern Electrometallurgy*, **2**: 3 (2022) (in Ukrainian).
3. B. E. Paton, V. Ya. Saenko, Yu. M. Pomarin, L. B. Medovar, G. M. Grigorenko, and B. B. Fedorovsky, *Problems of Special Electrometallurgy*, **1**: 3 (2002) (in

Russian).
4. B. E. Paton, V. Ya. Saenko, and Y. M. Pomarin, *Spetsial'naya Metallurgiya: Vchera, Segodnya, Zavtra* [Special Metallurgy: Yesterday, Today, Tomorrow] (Kyiv: Politekhnika: 2002) (in Russian).
5. B. Chen, Y. Ma, M. Gao, and K. Liu, *J. Mater. Sci. Technol.*, **26**, Iss. 10: 900 (2010).
6. A. A. Ilin, B. A. Kolachev, and I. S. Polkin, *Titanovyye Splavy. Sostav, Struktura, Svoistva* [Titanium Alloys. Composition, Structure, Properties] (Moskva: VILS-MATI: 2009) (in Russian).
7. M. Reith, M. Franke, M. Schloffer, and C. Körner, *Materialia*, **14**: 100902 (2020).
8. D. Wimler, J. Lindemann, M. Reith, A. Kirchner, M. Allen, W. G. Vargas, M. Franke, B. Klöden, T. Weißgärber, V. Güther, M. Schloffer, H. Clemens, and S. Mayer, *Intermetallics*, **131**: 107109 (2021).
9. T. Klein, L. Usategui, B. Rashkova, M. L. Ny, J. San Juan, H. Clemens, and S. Mayer, *Acta Mater.*, **128**: 440 (2017).
10. M. V. Maltsev, *Modifitsirovannaya Struktura Metallov i Splavov* [Modified Structure of Metals and Alloys] (Moskva: Metallurgiya: 1964) (in Russian).
11. O. N. Magnitskiy, *Liteinyye Svoistva Titanovykh Splavov* [Casting Properties of Titanium Alloys] (Moskva: Mashinostroenie: 1968) (in Russian).
12. V. S. Goltvyanitsa, O. I. Bankovskiy, E. I. Tsivirko, and S. K. Goltvyanitsa, *Novyye Materialy i Tekhnologii v Metallurgii i Mashinostroenii*, No. 1: 66–68 (in Russian).
13. G. A. Bochvar, *Tekhnologiya Legkikh Splavov*, 45 (2005) (in Russian).
14. A. I. Shcherbakov, *Zashchita Metallov*, **36**, No. 3: 255 (2005) (in Russian).
15. N. V. Sysoeva, *Tekhnologiya Legkikh Splavov*, No. 4: 85 (2002).
16. S. A. Firstov, V. F. Horban, N. A. Urticaria, Y. R. Pechkovskii, N. I. Danilenko, and M. V. Karpets, *Strength of Materials*, **42**: 622.
17. E. K. Molchanova, *Atlas Diagramm Sostoyaniya Titanovykh Splavov* [Atlas of State Diagrams of Titanium Alloys] (Moskva: Mechanical Engineering: 1964) (in Russian).
18. I. I. Kornilov, *Fiziko-Khimicheskie Osnovy Zharoprochnosti Splavov* [Physico-Chemical Basis of Heat Resistance of Alloys] (Moskva: AN SSSR: 1961) (in Russian).
19. J. Kumpfert, *Advanced Engineering Materials*, **3**, No. 11: 851 (2001).
20. E. A. Borisova, G. A. Bochvar, and M. Ya. Brun, *Titanovyye Splavy. Metallografiya Titanovykh Splavov* [Titanium Alloys. Metallography of Titanium Alloys] (Moskva: Metallurgiya: 1980) (in Russian).
21. *Titanium'99: Science and Technology: Proc. 9th World Conf. on Titanium (Saint-Petersburg, Russia, 7–9 July 1999)* (Prometey: 1999), vol. **1–3**.
22. B. A. Kolachev, V. Y. Elagin, and V. A. Livanov, *Metallurgiya i Termicheskaya Obrabotka Tsvetnykh Metallov i Splavov: Uchebnik Dlya Vuzov* [Metallurgy and Thermal Treatment of Non-Ferrous Metals and Alloys: Textbook for Universities] (Moskva: "MISiS": 2005) (in Russian).
23. T. M. Radchenko, V. A. Tatarenko, H. Zapolsky, and D. Blavette, *Journal of Alloys and Compounds*, **452**, Iss.1: 122.
24. S. P. Belov, *Metally*, **1**: 134 (1994) (in Russian).

Metallophysics and Advanced Technologies
Металофіз. новітні технол.
Metallofiz. Noveishie Tekhnol.
2025, vol. 47, No. 3, pp. 257–270
https://doi.org/10.15407/mfint.47.03.0257
Reprints available directly from the publisher

PACS numbers: 61.66.Dk, 61.72.Ff, 62.20.Qp, 81.20.Ev, 81.40.Cd, 81.40.Lm, 81.70.Bt

Sintered Al–Si–Ni Alloy: Structure and Properties. II. Sintering and Forging

V. V. Kaverinsky, G. A. Bagliuk, S. F. Kyrylyuk, D. G. Verbylo, Z. P. Sukhenko, I. M. Kirian*, M. A. Skoryk*, and O. D. Rud*

I. M. Frantsevich Institute for Problems in Materials Science, N.A.S. of Ukraine,
3 Omeljan Pritsak Str.,
UA-03142 Kyiv, Ukraine
**G. V. Kurdyumov Institute for Metal Physics, N.A.S. of Ukraine,*
36 Academician Vernadsky Blvd.,
UA-03142 Kyiv, Ukraine

The presented study focuses on the development of a high-silicon Al–Si–Ni alloy with a coefficient of thermal expansion (CTE) comparable to that of steels, using powder metallurgy techniques. Experimental investigations are conducted to evaluate the effects of different sintering regimes—both liquid phase and solid one—on materials fabricated from elemental powder mixtures and ball-milled pre-alloyed powders. The results indicate that the optimal properties are achieved using a solid-phase sintering process followed by hot side setting and hot forging. This method results in a non-porous material with homogeneously distributed, fine spherical silicon inclusions, ranging from 1 to 7 μm in size. Liquid-phase sintering is revealed impractical due to exudation, which leads to chemical-composition misrepresentation and the formation of course, cast-like structures with reduced mechanical properties. The use of pre-alloyed powders is determined to be preferable over elemental powder mixtures, as the latter results in porous materials with coarse intermetallic aggregates. The final alloy exhibits high mechanical properties, including yield strength of ≅ 221 MPa, ultimate tensile strength of ≅ 261 MPa, and hardness of ≅ 96 *HB*, alongside a CTE suitable for industrial applications.

Key words: Al–Si–Ni alloy, powder metallurgy, thermal expansion coeffi-

Corresponding author: Oleksandr Dmytrovych Rud
E-mail: rud@imp.kiev.ua

Citation: V. V. Kaverinsky, G. A. Bagliuk, S. F. Kyrylyuk, D. G. Verbylo, Z. P. Sukhenko, I. M. Kirian, M. A. Skoryk, and O. D. Rud, Sintered Al–Si–Ni Alloy: Structure and Properties. II. Sintering and Forging, *Metallofiz. Noveishie Tekhnol.*, **47**, No. 3: 257–270 (2025). DOI: 10.15407/mfint.47.03.0257

cient, sintering techniques, mechanical properties.

У даному дослідженні зосереджено увагу на розробці висококремнійового стопу Al–Si–Ni з коефіцієнтом теплового розширення (КТР), близьким до КТР криці, з використанням технологій порошкової металурґії. Проведено експериментальні дослідження для оцінки впливу різних режимів спікання як у рідкій, так і в твердій фазах на матеріяли, виготовлені з порошкових сумішей елементарних компонентів і подрібнених порошків попередньо виготовленого стопу. Результати показали, що оптимальні властивості досягнуто за допомогою процесу спікання у твердій фазі з подальшим гарячим пресуванням і штампуванням. Цей метод дав змогу одержати матеріял з однорідно розподіленими дрібними сферичними включеннями силіцію розміром від 1 до 7 мкм. Спікання в рідкій фазі виявилося недоцільним через явище випотівання, яке призводить до спотворення хемічного складу та формування грубих структур литого типу з пониженими механічними властивостями. Використання порошків стопу було визнано ліпшим, аніж сумішей елементарних компонентів, оскільки останні приводять до утворення пористих матеріялів з грубими інтерметалевими аґреґатами. Одержаний стоп демонструє високі механічні властивості, включаючи межу плинности у ≅ 221 МПа, межу міцности за розтягу у ≅ 261 МПа і твердість у ≅ 96 *HB*, а також КТР, що відповідає вимогам промислових виробників.

Ключові слова: стоп Al–Si–Ni, порошкова металурґія, коефіцієнт теплового розширення, методи спікання, механічні властивості.

(Received 20 August, 2024; in final version, 22 October, 2024)

1. INTRODUCTION

The advancement of industry heavily relies on the introduction of new materials with distinct physical, mechanical, and functional properties [1–3]. A significant focus is directed towards the development of innovative technologies for producing modern metallic and metal-composite materials, to enhance their physical and chemical properties. The necessity for novel materials arises from the imperative to improve product characteristics, expand the operational temperature range, and protect equipment from destabilising factors during use. Of particular interest for the manufacturing of precision orientation and navigation instruments in space applications are aluminium-based composite materials that exhibit a reduced coefficient of thermal expansion (CTE) coupled with high resistance to microdeformation.

A promising approach to developing lightweight, corrosion-resistant materials with a low CTE is through the utilisation of hypereutectic alloys within the Al–Si system. This approach is largely favoured due to the almost proportional reduction in CTE with increasing silicon concentration, given that the CTE of silicon is approximate-

ly six times lower than that of aluminium [4]. However, conventional casting methods used for alloys with silicon content exceeding 15% often result in the formation of coarse primary crystals, which significantly degrade the mechanical and technological properties of the material. Furthermore, increasing the silicon content beyond 20–22% exacerbates zonal segregation [4, 5]. Despite the availability of various modification techniques aimed at refining the morphology of the coarse silicon component, traditional methods have yet to produce high-silicon alloys that fully meet the desired quality and property standards.

Powder metallurgy presents a viable solution to the aforementioned challenges in producing the required materials. However, the practical implementation of this approach introduces numerous challenges that necessitate comprehensive research in metal physics and materials science. The preceding phase of this study focused on the development of pre-alloyed powder, which serves as the raw material for subsequent product manufacturing. Nonetheless, additional questions and challenges arise concerning the technology used for producing the final material. Key considerations include determining the optimal sintering temperature and duration, assessing the relative merits of solid-state versus liquid-phase sintering, deciding between using a mere mixture of components or producing a master alloy, addressing potential porosity, and ensuring that the mechanical properties of the alloy are satisfactory, along with strategies for their enhancement. This segment of the study aims to address these questions and develop a suitable technology for producing such materials.

The literature lacks consensus on the suitability of liquid-phase versus solid-state sintering regimes for aluminium-based powder materials. Studies have investigated the sintering of Al–Si, Al–Cu, Al–Si–Cu, and Al–Zn alloys in the presence of a liquid phase, as reported in works [6–10]. These studies highlight the positive effects of liquid-phase sintering, such as the reduction of material porosity through pore filling by the melt. However, it is important to note that these studies focused on alloys with different chemical compositions, characterised by lower silicon content (no more than 12–14%), the absence or significantly lower content of nickel, and the presence of other alloying elements such as copper, zinc, or magnesium. As such, the recommendations derived from these studies cannot be directly applied to the material under consideration without verification and modification.

Hot deformation processing is one potential method for mitigating porosity in powder materials. However, Al–Si materials are known for their brittleness, which may necessitate a specialised technique for hot deformation. Despite these challenges, it remains feasible, and our prior research on the deformation-heat treatment of Al–Si alloys—albeit with lower silicon content in cast alloys—yielded some promising results in terms of structural and property improvements [11]. In

this study, such a method will be applied to materials produced via powder metallurgy, with significantly higher silicon content.

The primary objective of this segment of the study is to develop approaches for the manufacture of Al–Si–Ni sintered alloys and to establish a robust technique that produces high-quality materials suitable for use in precision device constructions.

2. MATERIALS AND METHODS

The present study investigates two principal approaches: the fabrication of materials using a mixture of elemental component powders, and the utilisation of powder produced by grinding melt-spun ribbons of the master alloy. For the first method, aluminium (Al) powder with an average particle size of approximately 147 μm, silicon (Si) powder of around 11 μm, and nickel (Ni) powder of about 76 μm were employed. In the second approach, the powder was generated by mechanically grinding the melt-spun ribbons of the Al–Si–Ni alloy using a Fritsch Pulverisette P-6 planetary ball mill equipped with a stainless steel bowl. The detailed procedure for obtaining the powder was delineated in the previous part of this study [12]. The resulting powder particles had an average size of approximately 180 μm. The chemical compositions of the powders utilised in this study are presented in Table 1.

The powders were compacted under a pressure range of 500–600 MPa into shells fabricated from low-carbon steel. The inclusion of these shells facilitates subsequent hot deformation treatment. Their presence is presumed to optimize the deformation process, making it more akin to the mode of all-around compression, which is critical for materials with inherent brittleness. The briquettes encased in steel shells had an outer diameter of 32 mm, an inner diameter of 28 mm, a height of 37 mm (including the bottom and cover), and a cover thickness of 1.5 mm. The bottom section was welded to the sidewall of the shell before pressing. After pressing and sintering, a cover was pressed onto the specimens and subsequently welded. A series of samples was prepared under the conditions outlined in Table 2.

A specialised die was constructed to facilitate the hot deformation processing. Images of its components are provided in Fig. 1. The temperature for the hot deformation ranged between 520 and 540°C.

TABLE 1. Chemical composition of the starting materials used for specimen fabrication, % wt.

Material type	Al	Si	Ni
Grinded melt-spun ribbon obtained from the Al–Si–Ni alloy	Base	31.32	6.51
Mixture of elemental powders		32.91	5.91

TABLE 2. The sample conditions preparation.

Sample number	Preparation conditions
1	Fabricated from the powder mixture, solid-phase sintering at 350°C (≅ 30 minutes) + 530°C (≅ 2 hours) and forging at 530–540°C
2	Fabricated from pre-alloyed powder, solid-phase sintering at 350°C (≅ 30 minutes) + 530°C (≅ 2 hours) and forging at 520°C
3	Fabricated from pre-alloyed powder, liquid-phase sintering at 560°C (40–45 minutes) and forging at 530–540°C
4	Fabricated from pre-alloyed powder, liquid-phase sintering at 560°C (40–45 minutes) and forging at 520°C, with prior side pressing at 510–520°C
5	Fabricated from the powder mixture, liquid-phase sintering at 560–580°C (≅ 40 minutes) without forging

Dilatometric measurements were conducted using a dilatometer equipped with an inductive transducer, with a relative measurement error of ±0.5%. Mechanical testing was performed on cylindrical samples with a gauge length $l_0 = 20$ mm and diameter $d_e = 3$ mm at a strain rate $e = 2 \cdot 10^{-3}$ s^{-1}. The phase composition of the alloys was analysed using a ДРОН-4 diffractometer with radiation MoK_α. The x-ray diffraction (XRD) patterns were processed using the Rietveld refinement method with MAUD software [13].

Electron microscopy and x-ray microanalysis of the present phases and structural entities were performed using a TESCAN MIRA 3 microscope. The microstructure of the samples was examined using an

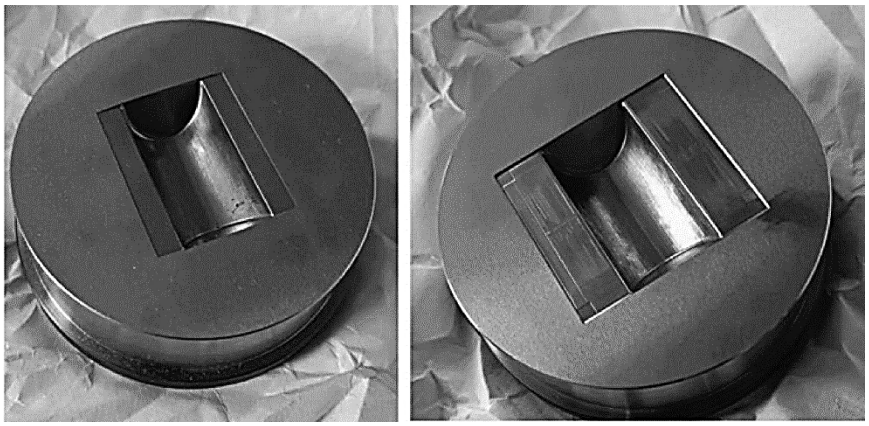

Fig. 1. Images of the die components used for the hot deformation treatment of samples.

'Optima Biofinder Bino' optical microscope, equipped with a 'SIGETA' digital ocular camera (model MC200).

3. RESEARCH RESULTS AND DISCUSSION

X-ray diffraction (XRD) patterns of the synthesised samples are illustrated in Fig. 2. The optimal Rietveld refinement for all sintered samples revealed three primary phases: an Al solid solution, Si, and the intermetallic compound $NiAl_3$. Notably, sample No. 1, fabricated *via* solid-phase sintering from a mixture of elemental powders, also exhibited a minor phase of Ni (≅ 2% wt.) (Fig. 2, *a*). However, according to the Rietveld refinement analysis, the Ni phase was not detected in the other samples.

The results of the quantitative phase analysis are detailed in Table 3. Sample No. 1, synthesised from a mixture of elemental powders by solid-phase sintering, exhibited the lowest amount of $NiAl_3$, potentially due to incomplete intermetallic formation. Conversely, samples No. 2 and No. 5 demonstrated the highest $NiAl_3$ content, approximating the equilibrium phase amount for the studied composition.

The sintering method and initial materials exert a considerable influence on the crystallite sizes of the observed phases. The largest crystallite sizes for Al were found in samples No. 1 and No. 2, obtained

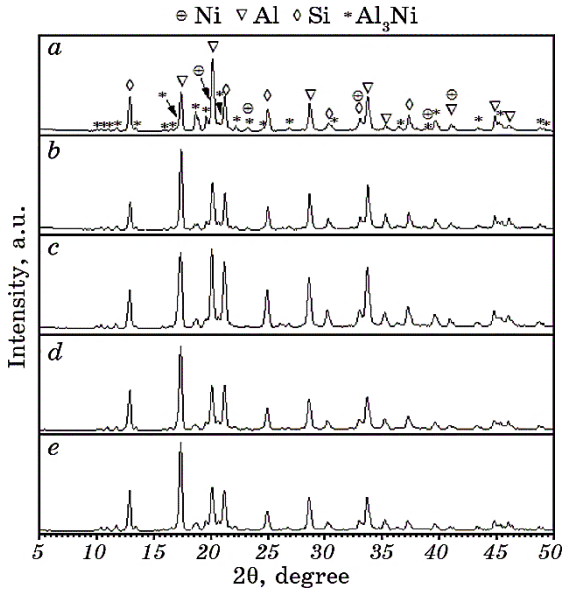

Fig. 2. Representative XRD patterns of sintered materials derived from powder mixtures (*a*, *e* for samples Nos. 1 and 5) and pre-alloyed powder (*b*–*d* for samples Nos. 2–4).

TABLE 3. Crystallographic parameters derived from Rietveld fitting of the XRD patterns of sintered samples.

Sample No.	Phase	Lattice parameters, Å			Crystallite size, Å	Abundance, % wt.	R_{wp}, %
		a	*b*	*c*			
1	Al	4.052	–	–	770	53	11.04
	Si	5.433	–	–	860	34	
	Al_3Ni	6.593	7.365	4.811	670	11	
	Ni	3.526	–	–	780	2	
2	Al	4.054	–	–	1070	58	12.5
	Si	5.433	–	–	1310	24	
	Al_3Ni	6.617	7.378	4.816	630	18	
3	Al	4.061	–	–	500	57	11.29
	Si	5.442	–	–	670	29	
	Al_3Ni	6.624	7.398	4.825	360	14	
4	Al	4.058	–	–	660	58	10.03
	Si	5.439	–	–	730	28	
	Al_3Ni	6.603	7.366	4.813	490	14	
5	Al	4.059	–	–	650	57	10.14
	Si	5.444	–	–	1025	26	
	Al_3Ni	6.623	7.389	4.831	600	17	

after solid-phase sintering from elemental powder (≅ 770 Å) and master alloy powder (≅ 1070 Å), respectively. Although the differences in crystallite sizes between samples subjected to different types of liquid-phase sintering were less pronounced, they were still observable. The crystallite sizes of Si in samples No. 1, No. 3, and No. 4 were approximately 670 Å, 730 Å, and 860 Å, respectively. Samples No. 2 and No. 5 exhibited larger values compared to the others. Notably, the smallest crystallite size for Ni_3Al was observed in sample No. 3 (≅ 360 Å). Both solid and liquid-phase sintering processes increased the Al lattice parameter, indicative of the formation of an Al-based solid solution. $NiAl_3$ was characterized by an orthorhombic lattice within the *Pnma* space group defined by the three lattice parameters *a*, *b*, and *c*.

The microstructure of sample No. 1, prepared from the elemental powder mixture through solid-phase sintering and subsequent hot deformation *via* forging at 530–540°C, is presented in Fig. 3. Significant porosity is evident in the synthesised material (Fig. 3, *a*). Silicon inclusions are uniformly distributed throughout the structure, with an average particle size of 50–70 μm. In addition, the structure contains

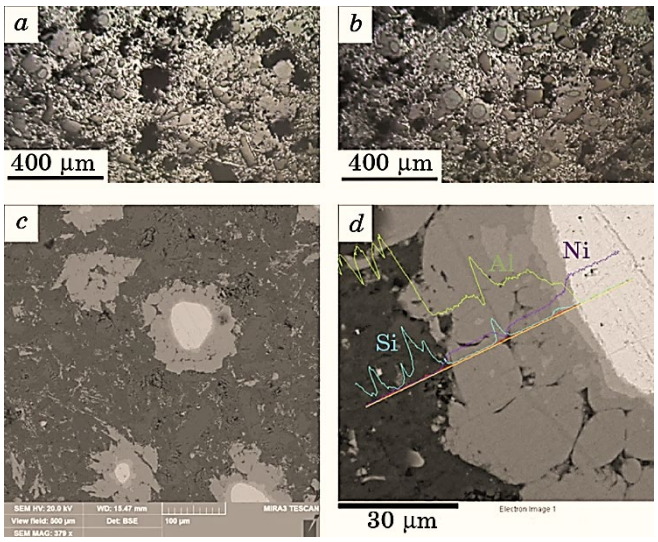

Fig. 3. Microstructure of material produced from a pure components mixture after solid-phase sintering and hot forging at 530–540°C (sample No. 1).

components in the form of rounded inclusions with a surrounding rim (Fig. 3, *b*). Based on the XRD analysis of this sample, these inclusions are likely nickel particles encased in a layer of Al_3Ni intermetallic.

To confirm the origin of these particles, an electron microscopy study coupled with energy-dispersive x-ray spectroscopy (EDS) analysis was conducted (Fig. 3, *d*). The grey background consists of a mixture of Al and Si phases, while the Ni core components attached to intermetallics were examined in details. Most of the intermetallic shell consists of $NiAl_3$, as previously observed in the XRD patterns. The aggregates identified in the structure (see Fig. 3, *c*) correspond to nickel particles surrounded by intermetallics, suggesting that the structure is not in equilibrium.

The hot forging process in this instance does not disrupt such aggregates. A thin (2–3 μm) layer of another intermetallic with a higher Ni content may also be present.

The most favourable structural characteristics were obtained for sample No. 2, produced from ball-milled master alloy powder after solid-phase sintering and hot forging at 520°C. Before forging, the sintered samples underwent preliminary hot pressing from the sides, achieving a set deformation degree of approximately 20–30% at 510–520°C. The microstructure of the material produced in this manner is shown in Fig. 4.

Silicon particles are evenly distributed within the metal matrix and are relatively small, with sizes ranging from 1 to 7 μm, significantly

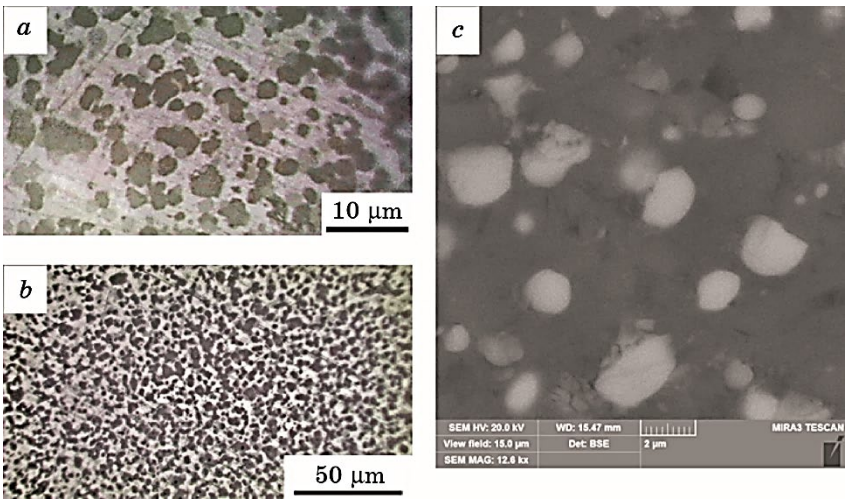

Fig. 4. Microstructure of material from pre-alloyed/master powder after solid-phase sintering and hot forging at 520°C (sample No. 2).

smaller than those in the other cases studied do. Based on the obtained structural indicators, this manufacturing method appears more suitable for further production. An SEM image of the structure of sample No. 2, which exhibited the best characteristics, is presented in Fig. 4. The intermetallic inclusions are spherical, with sizes of approximately 1–3 μm.

The microstructures of specimens produced from pre-alloyed powder after liquid-phase sintering and hot forging at 520–540°C are depicted in Fig. 5. Cast-like structures are visible in some areas (Fig. 5, *a*, *c*), with defects (pores) observed in these regions. The majority of the structure, however, consists of equiaxed polyhedral silicon particles. These inclusions exhibit a wide size range, from ≅ 5 μm to ≅ 60 μm, with an average size of 26.4 ± 4.7 μm.

Reducing the forging temperature to 520°C and incorporating side hot pre-pressing resulted in some improvement in the structure (Fig. 5, *b*, *d*). Despite this, the silicon inclusions were larger than those observed after solid-phase sintering were. The inclusions were homogeneously distributed, and cast-like structures as well as significant pores were not present. The inclusion sizes varied from ≅ 5 μm to ≅ 40 μm, with an average size of 19.8 ± 2.3 μm.

Although it is possible to mitigate porosity and cast structures after liquid-phase sintering, the large initial cast silicon crystals result in larger inclusions following deformation. Additionally, liquid-phase exudation can uncontrollably distort the chemical composition. Spectral analysis of the samples after liquid-phase sintering revealed an increase in Si content to approximately 40%.

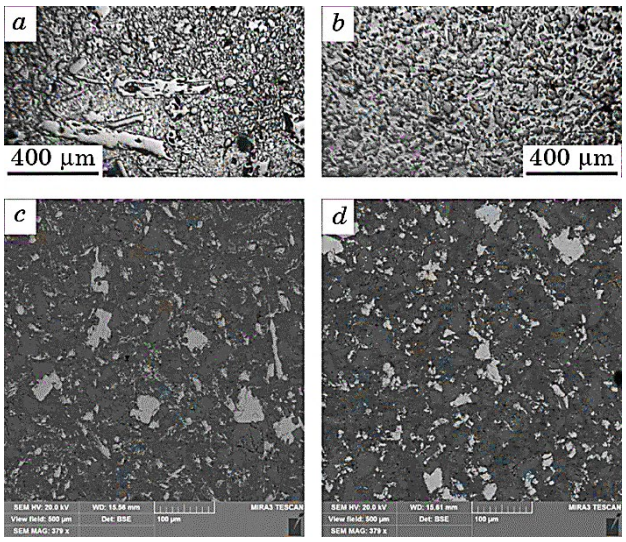

Fig. 5. Microstructure of material from pre-alloyed powder after liquid-phase sintering and hot deformation: forging at 530–540°C, regions with cast-like structures and pores (sample No. 3) (*a*, *c*), forging at 520°C with side pressing at 510–520°C (sample No. 4) (*b*, *d*).

Figure 6 illustrates the microstructure of sample No. 5, fabricated from a powder mixture after liquid-phase sintering and hot deformation. In this instance, slightly less porosity was observed compared to the undeformed state. The specific intermetallic inclusion structures identified after solid-phase sintering were not observed here.

The microstructure (Fig. 6, *a*) consists mainly of elongated Si particles embedded in the Al matrix. These silicon inclusions have a broad size range, from $\cong 10$ μm to $\cong 100$ μm, with an average size of 35.6 ± 6.3 μm. The elongated shapes are likely a result of deformation during the forging process, which aligns the inclusions along the direction of applied force.

Interestingly, the XRD analysis of sample No. 5, produced from the powder mixture through liquid-phase sintering and subsequent hot deformation, revealed no significant difference in phase composition compared to sample No. 1, which underwent solid-phase sintering. However, the microstructural examination highlighted notable disparities in the distribution and morphology of phases. The microstructure of sample No. 5 displayed a coarser and more heterogeneous distribution of Si particles compared to sample No. 1. This discrepancy is attributed to the presence of liquid phases during sintering, which facilitated the growth and coalescence of Si particles.

The microstructural analysis clearly shows that the method of sintering and the nature of the initial powder significantly influence the

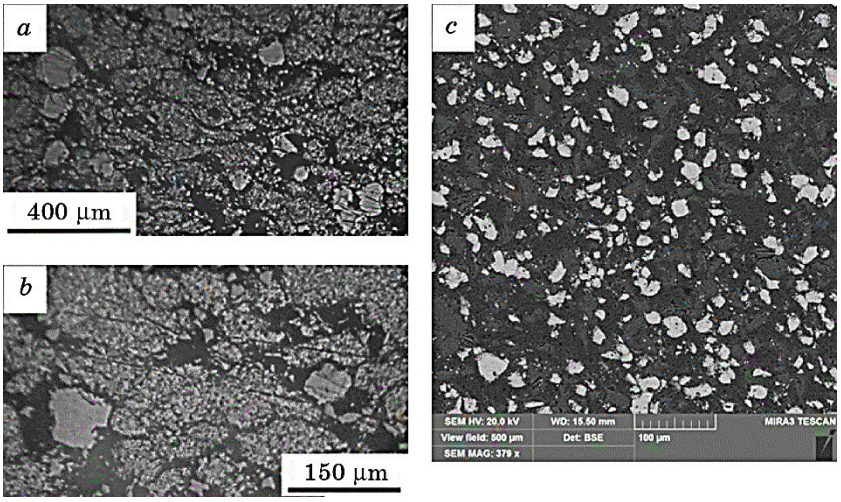

Fig. 6. Microstructure of material from elemental components mixture after liquid-phase sintering and hot deformation at 540–550°C (sample No. 5).

final properties of the material. Solid-phase sintering, especially when combined with hot forging, appears to produce a more uniform microstructure with finer Si particles, which is preferable for enhancing mechanical properties.

The mechanical properties of the sintered and forged samples were evaluated through hardness testing and tensile strength measurements. The results are summarised in Table 4.

Sample No. 2, produced from master alloy powder *via* solid-phase sintering and hot forging, exhibited the highest hardness and tensile strength. These superior properties can be attributed to the fine and homogeneous microstructure obtained through this manufacturing process. In addition, this material exhibited some ductility; however, not significant: values of total elongation reduction of the area were not more than $\cong 2\%$. Nevertheless, the other types of samples appear brittle without any noticeable signs of plasticity at home temperature.

All the other studied types of samples have significantly lower

TABLE 4. Effect of sintering conditions on the mechanical properties.

Sample number	σ_Y, MPa	σ_U, MPa	Hardness, *HB*
1	–	81.3 ± 27.2	68.1 ± 5.3
2	220.7 ± 10.3	261.2 ± 20.9	95.8 ± 3.2
3	–	116.6 ± 10.5	76.9 ± 4.5
4	–	139.7 ± 12.4	82.5 ± 5.7

TABLE 5. CTE values of the material at the studied temperatures.

Samples type	CTE at the temperature, $K^{-1} \cdot 10^6$					
	50°C	100°C	150°C	200°C	250°C	300°C
As-cast alloy		13.2		14.2		
Solid state sintering and forging (No. 2)	13.81	14.98	15.42	15.84	16.19	16.52
Liquid phase sintering and forging (No. 4)	10.51	12.95	13.18	13.49	13.82	14.13

strength and hardness values, which are caused by larger and rough-shaped silicon inclusion in addition to porosity. Among them, the strongest were the samples made of the pre-alloyed powder after liquid phase sintering and deformation regime close to the solid phase sintered previously considered one, which was almost nonporous. The highest ultimate tensile strength shown for such material was 145.4 MPa. Samples made of pure components mixture exhibit the lowest strength and are very brittle.

As it was mentioned in the introduction, except for obtaining appropriate mechanical properties this material needs to have a relatively low CTE close to those of steel. To check its value dynamometric tests were carried out. The results of these tests are given in Table 5. Because of liquid phase exudation liquid, which leads to significant silicon content increase, the corresponding samples exhibit lower CTE values. Pores also contribute to its decline. In the samples that had solid-state sintering and hot forging, which shoved the best mechanic properties, its value at lover temperatures is $13.81 \cdot 10^{-6}\ K^{-1}$. It is quite close to CTE of steel, which could be about $\cong (11-15) \cdot 10^{-6}\ K^{-1}$. However, for plain low-alloyed and carbon steels, it is about $\cong (11-12) \cdot 10^{-6}\ K^{-1}$, which is a bit less than the studied here material. The closest CTE matching shows Cr and Ni alloyed stainless steels, high Cr instrumental steels, and special Cr and Co alloyed steels.

Annealing after deformation does not make a valuable impact on the CTE of the material. However, it could be assumed that some rise of it might be observed, especially for the higher temperatures.

4. CONCLUSIONS

An experimental investigation was carried out to develop an optimised manufacturing process for a high-silicon Al–Si–Ni alloy with a coefficient of thermal expansion comparable to that of steels, using powder metallurgy techniques. In addition to the conventional pressing and sintering stages, hot forging was introduced to mitigate porosity and refine the morphology of silicon inclusions, thereby enhancing the ma-

terial properties. Both liquid and solid-phase sintering regimes were examined for materials produced from elemental powder mixtures and ball-milled pre-alloyed powders.

The results demonstrated that the optimal microstructure and properties were achieved using the following method: production of alloy powder through mechanical grinding of a rapidly solidified strip, compaction of the powder into a low-carbon steel shell at a pressure of 500–600 MPa, vacuum sintering (30 minutes at 350°C followed by 2 hours at 530°C), hot side setting with 20–30% deformation at 510–520°C, and hot forging at 520°C. This process resulted in a non-porous material with homogeneously distributed, fine, spherical silicon inclusions ranging in size from 1 to 7 μm.

Liquid-phase sintering was deemed impractical for the production of this material due to the exudation of the liquid phase, which uncontrollably alters the chemical composition of the material and promotes the formation of pores and voids. Furthermore, even if mechanical means were employed to prevent exudation, the presence of silicon crystals in the liquid phase would lead to their growth, resulting in coarse, cast-like structures with significantly reduced strength.

The use of elemental powder mixtures as a raw material was found to be highly undesirable. Instead, a pre-alloyed powder with the specified composition is recommended, which can be obtained by methods such as grinding a rapidly solidified strip. During solid-state sintering of elemental powder mixtures, nickel, which is insoluble in solid aluminium, tends to form coarse intermetallic aggregates that may include non-equilibrium compounds. Materials produced in this manner also exhibited porosity even after hot forging.

The study further revealed that the manufacturing method significantly influences the crystallite sizes for the Al and Si phases. These regions were found to be approximately 1.5 to 2.0 times larger after solid-phase sintering compared to liquid-phase sintering, regardless of whether the samples were manufactured from powder mixtures or pre-alloyed powders. In liquid-phase sintering, samples with larger coherent scattering regions may exhibit a finer overall structure. Additionally, a minor effect on the lattice parameters of the Al phase and $NiAl_3$ was observed.

As a result, the material developed in this study exhibits high mechanical properties (yield strength $\sigma_Y \cong 221$ MPa, ultimate tensile strength $\sigma_U \cong 261$ MPa, and hardness $\cong 96$ HB), with a coefficient of thermal expansion that meets production requirements, demonstrating its suitability for industrial application.

REFERENCES

1. V. I. Razumovskii and Y. K. Vekilov, *Phys. Solid State*, **53**: 2189 (2011).
2. R. Eliot, *Eutectic Solidification Processing. Crystalline and Glassy Alloys*

(Elsevier: 1983).
3. S. G. Alieva, M. B. Altman, and S. M. Ambartsumyan, *Promyshlennye Alyuminievyye Splavy* [Industrial Aluminium Alloys] (Moskva: Metallurgiya: 1984) (in Russian)
4. V. Vasenev, V. Mironenko, V. Butrim, A. Aronin, and I. Aristova, *Int. Conf. 'Powder Metallurgy and Particulate Materials'* (2013), p. 606.
5. E. L. Rooy, *Properties and Selection: Nonferrous Alloys and Special-Purpose Material* (ASM International: 1990), vol. **2**, p. 3.
6. I. Arribas, J. M. Martin, and F. Castro, *Mater. Sci. Eng. A*, **527**, Iss. 16–17: 3949 (2010).
7. M. L. Delgado, E. M. Ruiz-Navas, E. Gordo, and J. M. Torralba, *J. Mater. Processing Technol.*, **162–163**: 280 (2005).
8. Su Shei Sia, *Development of Hypereutectic Al–Si Based P/M Alloys* (Birmingham: 2012).
9. E. Crossin, J. Y. Yao, and G. B. Schaffer, *Powder Metallurgy*, **50**, Iss. 4: 354 (2007).
10. E. L. Ortiz, W. R. Osyrio, A. D. Bortolozo, G. S. Padilha, J. Y. Yao, and G. B. Schaffer, *Metals*, **12**, Iss. 6: 962 (2022).
11. V. V. Kaverinsky, Z. P. Sukhenko, G. A. Baglyuk, and D. G. Verbylo, *Metallofiz. Noveishie Tekhnol.*, **44**, No. 6: 769 (2022).
12. G. A. Bagliuk, T. O. Monastyrska, V. V. Kaverinsky, V. P. Bevz, V. K. Nosenko, I. M. Kirian, D. L. Pakula, V. V. Kyrylchuk, A. M. Lakhnik, and O. D. Rud, *Metallofiz. Noveishie Tekhnol.*, **45**, No. 8: 951 (2023).
13. L. Luterotti and S. Gialanella, *Acta Mater.*, **46**: 101 (1998).

Metallophysics and Advanced Technologies
Металофіз. новітні технол.
Metallofiz. Noveishie Tekhnol.
2025, vol. 47, No. 3, pp. 271–285
https://doi.org/10.15407/mfint.47.03.0271
Reprints available directly from the publisher

PACS numbers: 06.60.Vz, 61.66.Dk, 61.72.Ff, 66.10.cg, 81.20.Vj, 81.70.Jb, 83.50.Uv

The Influence of the Size of the Brazing Gap on the Structure and Strength of Kovar Joints with Stainless Steel

S. V. Maksymova, P. V. Koval'chuk, and V. V. Voronov

E. O. Paton Electric Welding Institute, N.A.S. of Ukraine,
11 Kazymyr Malevych Str.,
UA-03150 Kyiv, Ukraine

Comprehensive studies of the influence of brazing gap widths (100, 50, 20 μm) on the structure and mechanical properties of brazed dissimilar joints between Kovar and stainless steel, utilizing Cu–Mn–4.5Co–2.5Fe filler metal during high-temperature vacuum brazing, are presented. X-ray microspectral analysis reveals a two-phase structure in the brazed seams, when Cu–Mn–Co–2.5Fe filler metal is employed. This structure consists of both the α-Cu phase forming the main zone of the brazed seam (with a 100 or 500 μm gap) and discrete grains of the γ-phase $(Fe_xMn_yCo_z)Me$. During brazing, mutual-diffusion processes occur at the interphase boundary between the liquid filler metal and the solid base metal. The filler metal becomes saturated with constituent components of the base metal—chromium, cobalt, and nickel—thus, influencing the chemical composition and mechanical properties of the brazed seam. Micro-x-ray spectral analysis indicates that reducing the gap from 100 to 20 μm increases the γ-phase $(Fe_xMn_yCo_z)Me$ content in the seam from 13.20% to 90.90%, while simultaneously decreasing the α-Cu phase from 86.83% to 9.10%. These structural changes positively affect the mechanical properties of the brazed dissimilar joints, leading to increased shear strength in Kovar–stainless steel overlap joints. With a gap size of 20 μm, the brazed samples exhibited failure primarily on the stainless steel (600 MPa).

Key words: copper–manganese–cobalt–iron filler metal, brazing gap, structure, strength, high-temperature vacuum brazing, solid solution.

Corresponding author: Svitlana Vasylivna Maksymova
E-mail: maksymova.svitlana15@ukr.net

Citation: S. V. Maksymova, P. V. Koval'chuk, and V. V. Voronov, The Influence of the Size of the Brazing Gap on the Structure and Strength of Kovar Joints with Stainless Steel, *Metallofiz. Noveishie Tekhnol.*, **47**, No. 3: 271–285 (2025). DOI: 10.15407/mfint.47.03.0271

Наведено результати комплексних досліджень впливу паяльного зазору (100, 50, 20 μm) за використання припою Cu–Mn–4,5Co–2,5Fe на структуру та механічні властивості паяних різнорідних з'єднань ковар–корозійнотривка криця за вакуумного високотемпературного лютування. Мікрорентґеноспектральною аналізою встановлено, що за застосування припою Cu–Mn–Co–2,5Fe у паяних швах формується двофазна структура, яку утворено первинною фазою — твердим розчином на основі системи Cu–Mn (α-Cu), який заповнює основну зону паяного шву (із зазором у 100, 50 мкм), і незначною кількістю окремих дискретних зерен γ-фази ($Fe_xMn_yCo_z$)*Me*. Встановлено, що під час процесу лютування перебігають взаємні дифузійні процеси на міжфазній межі між рідким припоєм і твердим основним металом. Припій насичується складовими компонентами основного металу: Хромом, Кобальтом і Ніклем, що впливає на хемічний склад металу паяного шва, відповідно, на механічні властивості паяних з'єднань. За результатами мікрорентґеноспектральної аналізи визначено, що зменшення зазору зі 100 до 20 μm приводить до збільшення кількости γ-фази ($Fe_xMn_yCo_z$)*Me* у шві з 13,20 до 90,90% і одночасного зменшення кількости α-Cu фази з 86,83 до 9,10%. Такі структурні особливості паяних різнорідних з'єднань позитивно впливають на їхні механічні властивості та сприяють збільшенню міцности на зріз напускних з'єднань ковар–корозійнотривка криця. За величини зазору у 20 мкм руйнування зразків відбувалося по основному металу — корозійнотривкій криці (600 МПа).

Ключові слова: припій Купрум–Манґан–Кобальт–Ферум, паяльний зазор, структура, міцність, високотемпературне вакуумне лютування, твердий розчин.

(Received 20 May, 2024; in final version, 1 February, 2025)

1. INTRODUCTION

The utilization of dissimilar material joints, such as Kovar with stainless steel, is becoming increasingly prevalent in the creation of responsible structures across various industries including electronics, energy, and automotive sectors [1–4]. Kovar is a precision iron-based alloy containing 29% nickel and 17% cobalt, which is characterized by a low coefficient of thermal expansion and is used in the production of individual brazed joints with glass, ceramics or other materials [5]. Stainless steel contains chromium, nickel, titanium or other alloying elements that increase its resistance to corrosion in various environments [6].

Several technological processes, including brazing, diffusion welding, electron beam, and laser welding, have been explored to fabricate Kovar joints with stainless steel [7–12]. Among these, brazing emerges as a promising and reliable method. Brazing facilitates the formation of interatomic bonds between materials by heating them to a temperature below the base metal melting point. With a suitably chosen filler

metal composition possessing a melting temperature range, it becomes possible to preserve the original structure and mechanical properties of the base metal [13].

By vacuum brazing, alongside temperature and holding time, the size of the brazing gap between the connecting parts represents a crucial parameter. It is well established that the structure formation in brazed seams and the resulting mechanical properties of brazed joints is closely linked to the size of the brazing gap [14–16].

This study aims to investigate the impact of gap size on the structure and mechanical properties of dissimilar Kovar-stainless steel joints obtained through vacuum high-temperature brazing, utilizing Cu–Mn–Co–Fe filler metal.

2. EXPERIMENTAL/THEORETICAL DETAILS

Experimental Cu–Mn–4.5Co–2.5Fe filler metal was produced by argon-arc melting using a non-fusible tungsten electrode on a cold copper substrate within a high-purity argon environment (argon volume fraction not less than 99.993%). To ensure uniform distribution of alloying elements throughout the ingot volume, the filler metal underwent fivefold remelting. For experimentation purposes, the filler metal was utilized in its cast state, boasting a melting temperature range of 917–957°C [17].

Base metal samples for mechanical testing (three samples per gap size) were crafted from precision alloy Kovar and stainless steel 12Kh18N10T, each measuring 80×15×2 (Fig. 1 and Table 1). The overlap size did not exceed the thickness of the brazed plates, which was 2 mm.

High-temperature brazing utilizing experimental filler metal was

TABLE 1. Chemical composition of Kovar (29NK) and steel 12Kh18N10T [18].

Grade	Chemical elements, wt. %									
	Fe	Ni	Co	C	Si	Mn	Cr	Ti	Al	Cu
Kovar	51.14–54.5	28.5–29.5	17–18	0.03	0.3	0.4	0.1	0.1	0.2	0.2
12Kh18N10T	67	9–1	–	0.12	0.8	2	17–19	0.4–1	–	0.3

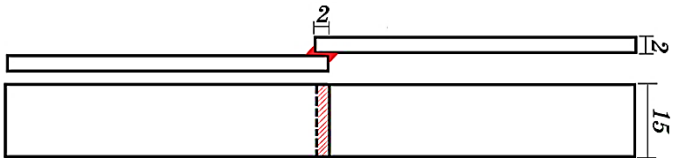

Fig. 1. Schematic representation of Kovar–stainless steel brazed joints.

conducted in a vacuum furnace (model SGV 2.4-2/15-I3) with radiation heating, featuring a working space rarefaction corresponds to 1.33×10^{-3} Pa. Heating was performed at a controlled rate not exceeding 18–20°C/min, while cooling within the temperature range of 1060 to 200°C maintained a rate of 10–15°C/min. Temperature measurement error was kept within ±5°C. The brazing temperature surpassed the liquidus temperature of the filler metal by 30°C, with a holding time at the brazing temperature set to 3 minutes. Prior to brazing, mechanical processing of the samples involved polishing with a 125 μm diamond tool and degreasing with B-70 gasoline followed by dehydration using technical alcohol. The cast-state filler metal (weighing 0.1–0.15 g) was positioned near the gap and secured using a contact welding machine. Gap sizes for the three batches of samples were maintained at 20 μm, 50 μm, and 100 μm, respectively. The samples were brazed without clamping or additional loading.

Post-brazing, samples composed of dissimilar materials were sectioned perpendicular to the seam, and microsections were prepared following standard procedures. Metallographic examinations and micro-x-ray spectral analyses were carried out using a TescanMira 3 LMU scanning electron microscope. The distribution of elements within separate phases was studied by localized micro-x-ray spectral analysis employing an Oxford Instruments X-max 80 mm^2 energy dispersive spectrometer. Microsections were observed without chemical etching, utilizing the reflected electron (BSE) mode, with measurement locality maintained within 1 μm. Mechanical properties of brazed joints were evaluated at room temperature utilizing a ZDM 10 Zwick-1488 testing machine. Percentage ratios of phases were determined through SEM image analysis using the ImageJ program, with an error margin of ±1.5%.

3. RESULTS AND DISCUSSION

During high-temperature vacuum brazing of Kovar flat samples with stainless steel using Cu–Mn–Co–2.5Fe filler metal, tight brazed seams are consistently achieved. The brazing gap size within the range of 20–100 μm does not impede the filler metal ability to wet both base materials and evenly spread over them. Notably, a well-formed direct and reverse fillet with negligible dimensions is observed (Fig. 2).

No defects such as erosion, unbrazing, cracks, or cavities were identified during visual inspection of the brazed joints. Remarkably, despite the base metal samples possessing varying coefficients of thermal linear expansion (Table 2), they maintained their geometric dimensions. This observation suggests the appropriate selection of the basic alloying system of the filler metal and hints at the potential relaxation of stresses between Kovar and stainless steel.

Thorough examinations of the structure of brazed joints (with a gap

TABLE 2. Coefficients of thermal linear expansion of stainless steel and forged steel [19, 20].

Temperature, °C	Coefficients of thermal linear expansion, 10^{-6}/°C	
	12Kh18H10T	Kovar
20	–	
100	16.6	5.86
200	17	5.20
300	17.2	5.13
350	–	4.89
400	17.5	5.06
450	–	5.25
500	17.9	6.15
600	18.2	7.80
700	18.6	9.12
800	18.9	10.31
900	19.3	11.26

size of 100 μm) using scanning electron microscopy in the reflected electron mode validated the superior quality formation of brazed seams (Fig. 3). It is worth noting that contrast in this mode is contingent upon the atomic number of the constituent elements within the brazed joint and obviates the need for chemical etching to discern the chemical composition of distinct phases.

The findings from local x-ray microspectral analysis confirmed a two-phase composition of the seam. The primary phase, constituting 86.83% of the total area of the seam, consists of a homogeneous Cu–Mn solid solution, incorporating trace amounts of nickel, iron, and cobalt (Fig. 3 and Table 3, spectrum 4).

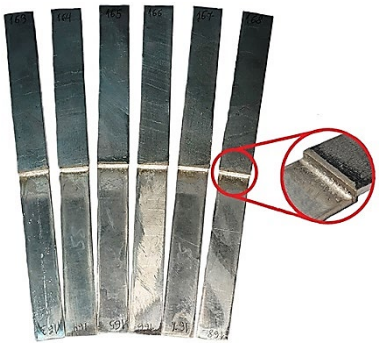

Fig. 2. Appearance of brazed samples.

TABLE 3. Chemical composition of separate phases in the Kovar–stainless steel brazed seam by 100 μm gap size.

No. spectrum	Chemical elements, wt.%							
	Si	Ti	Cr	Mn	Fe	Co	Ni	Cu
1	0.54	0.22	17.87	1.37	71.50	0.00	8.50	0.00
2	0.14	0.65	2.91	32.16	32.58	20.11	2.54	8.91
3	0.17	0.00	3.28	30.38	34.35	19.87	3.32	8.63
4	0.00	0.00	0.00	26.49	1.12	1.43	3.48	67.48
5	0.00	0.00	2.87	28.50	34.25	19.60	4.68	10.10
6	0.17	0.00	1.97	31.23	35.12	18.83	3.86	8.83
7	0.12	0.00	1.93	28.64	36.72	18.40	5.85	8.34
8	0.27	0.00	0.00	0.39	52.75	18.01	28.58	0.00

The second phase comprises discrete dark grains of an iron-based phase, which also incorporate other constituents from both the filler metal and the base metal (Table 3, spectrum 2, 3, 5, 6, and 7). The concentration of iron within these grains falls within the range of 32.58–36.72%. According to binary diagrams of metal systems, this compound likely corresponds to the γ phase $(Fe_xMn_yCo_z)Me$ [21]. Notably, with a gap size of 100 μm, this phase predominantly crystallizes near the seam's border with the base metal. In the central zone of the seam, its presence is minimal, except for isolated single grains of minor sizes ranging from 4 to 10 μm. These grains exhibit enrichment in iron, manganese, and cobalt, collectively occupying 13.17% of the seam area.

The results of electron beam scanning perpendicular to the seam corroborate previous findings and confirm the homogeneous distribution of manganese across the entire width of the brazed seam.

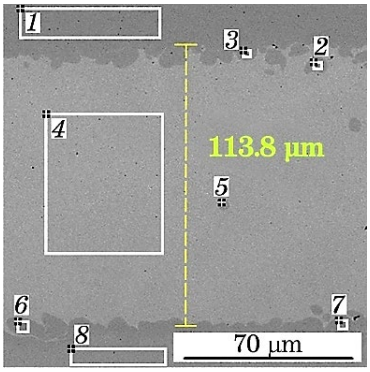

Fig. 3. Microstructure of a brazed dissimilar Kovar–stainless steel joint by 100 μm gap.

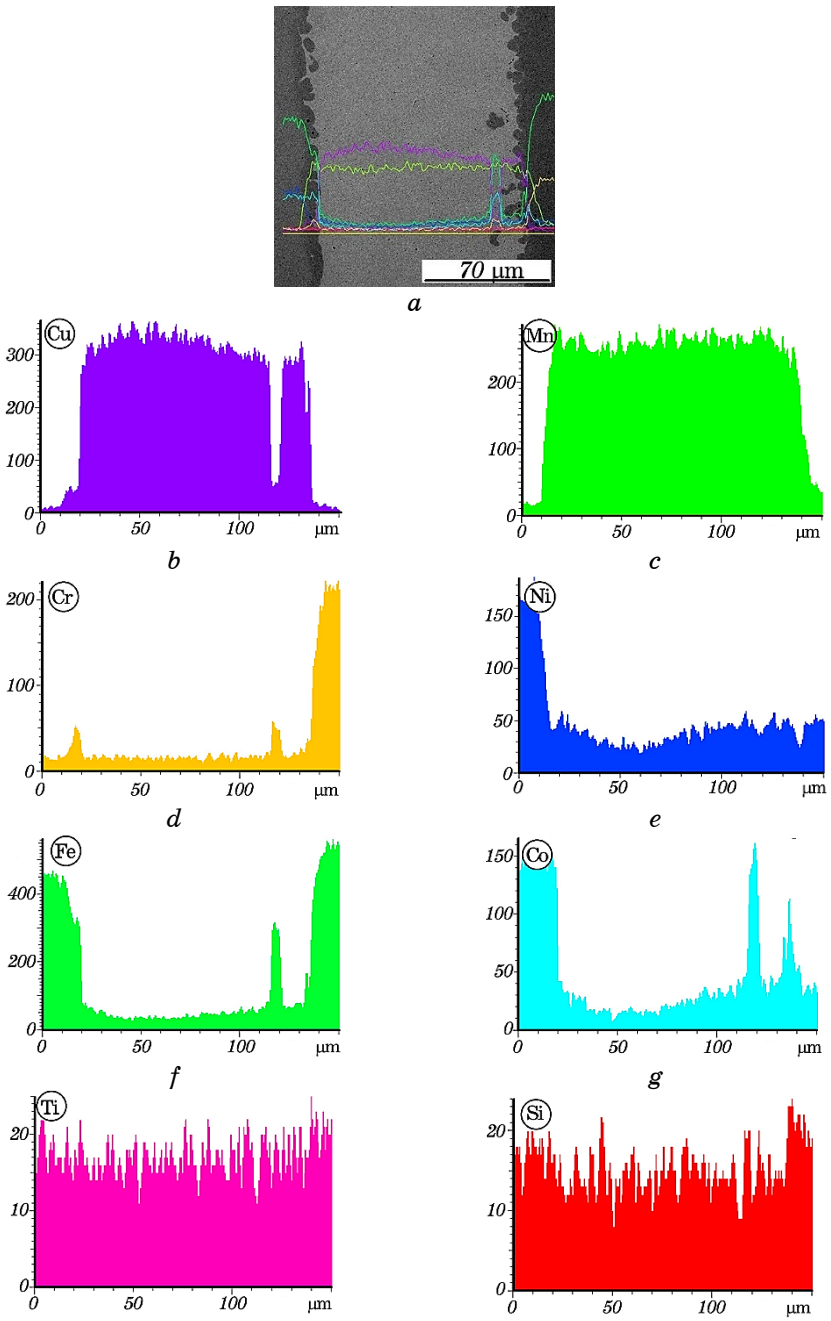

Fig. 4. Electronic image of the microstructure of the brazed joint (*a*) and the distribution of copper (*b*), manganese (*c*), chromium (*d*), nickel (*e*), iron (*f*), cobalt (*g*), titanium (*h*), and silicon (*i*).

Within the discrete dark grains, there is a noticeable increase in the concentration of iron, cobalt, and chromium, accompanied by a significant reduction in the amount of copper (Fig. 4).

The decrease in the amount of nickel, albeit to a lesser extent, is also notable during the scanning of this phase with a beam. Based on the findings from micro-x-ray spectral studies, it can be affirmed that active mutual diffusion processes occur between the components of the filler metal and the base metal during the formation of the structure of brazed joints. Specifically, iron, cobalt, nickel, chromium, and manganese exhibit such interactions. These processes are influenced by factors including the heating temperature, non-equilibrium conditions of crystallization of the brazing filler metal, and the chemical composition of both the base metal and filler metal.

Consequently, a concentration gradient emerges at the interface between the filler metal and the base metal.

Drawing upon the aforementioned results, a schematic representation of the metal structure formation of the brazed seam can be proposed (Fig. 5). This representation elucidates a significant transformation in the chemical composition of the original filler metal during

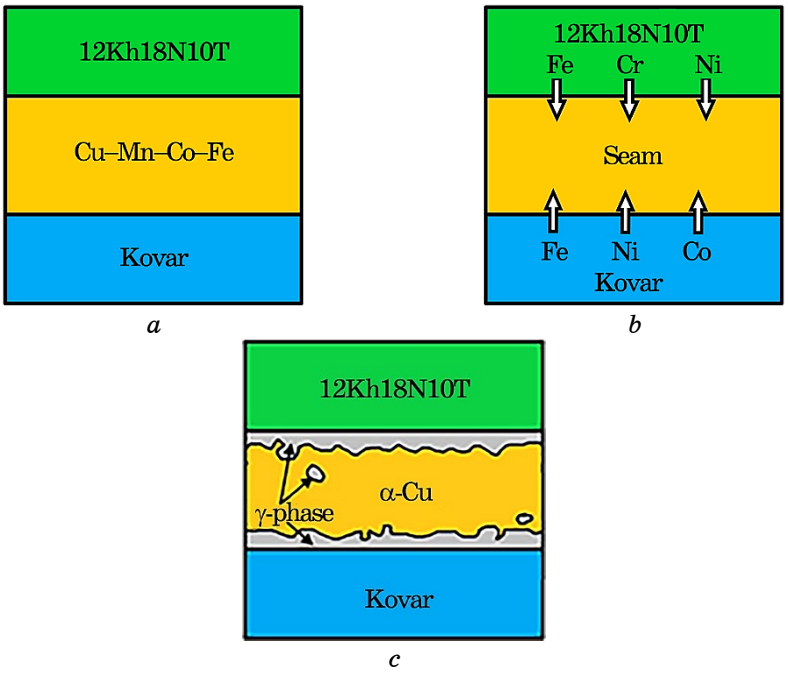

Fig. 5. Scheme of the formation of dissimilar Kovar joints with stainless steel with a gap of 100–50 μm: in the initial state (*a*); during heating (*b*) and after crystallization of the brazed seam (*c*).

TABLE 4. Chemical composition of separate phases in the Kovar–stainless steel brazed seam by 50 μm brazing gap.

No. spectrum	Chemical elements, wt. %							
	Si	Ti	Cr	Mn	Fe	Co	Ni	Cu
1	0.50	0.00	18.02	1.26	71.27	0.00	8.94	0.00
2	0.00	0.00	3.46	29.58	36.80	18.41	3.23	8.51
3	0.00	0.00	3.38	25.95	37.13	17.91	5.61	10.02
4	0.00	0.00	0.14	24.87	1.25	1.24	4.27	68.22
5	0.18	0.00	2.44	29.00	36.95	18.49	4.68	8.25
6	0.19	0.00	0.07	0.55	53.07	17.87	28.25	0.00

high-temperature brazing. This transformation contributes to the formation, alongside the solid solution (copper-based), of an iron-based phase manifested in the form of discrete single grains against a solid solution background.

Reducing the brazing gap size from 100 to 50 μm does not affect the morphology of the seam, but only leads to a decrease in its width (Fig. 6).

Similar to the previous sample, its structure is constituted by a copper–manganese solid solution, albeit with a slight reduction in its proportion compared to the previous sample, accounting for 82.25% of the total seam area. The concentration of iron in this solid solution remains consistent with the measurements of the previous sample, approximately at ≅ 1.25% (Fig. 6, Table 4, spectrum 4).

Notably, the proportion of the γ-phase ($Fe_xMn_yCo_z$)*Me* in the seam increases by approximately 4%, reaching 17.75%. This phase is predominantly observed near the interface of the filler metal with the base metal (Fig. 6, Table 4, spectrum No. 2 and No. 5).

Reducing the gap size to 20 μm during the brazing of dissimilar Ko-

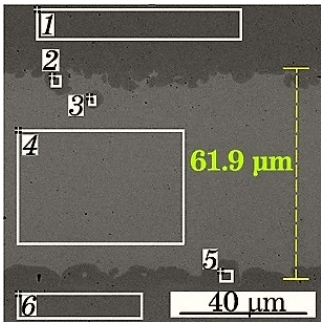

Fig. 6. Microstructure of a dissimilar brazed joint Kovar–stainless steel with the gap of 50 μm.

TABLE 5. Chemical composition of separate phases in the Kovar–stainless steel brazed seam by 20 μm brazing gap.

No. spectrum	Chemical elements, wt. %							
	Si	Ti	Cr	Mn	Fe	Co	Ni	Cu
1	0.25	0.00	5.15	20.25	46.13	11.25	9.46	7.52
2	0.00	0.00	0.74	17.68	6.39	1.71	7.49	65.99
3	0.33	0.19	9.85	16.28	53.58	7.43	8.00	4.34
4	0.21	0.00	4.94	20.34	46.18	10.56	9.63	8.13
5	0.16	0.00	0.23	0.36	54.08	17.68	27.49	0.00
6	0.47	0.23	17.81	1.31	70.59	0.44	8.89	0.26

var-stainless steel joints results in not only a decrease in the width of the brazed joint but also induces notable morphological changes in the structure during the crystallization of the brazed seam metal (Fig. 7).

Based on the research findings, there is a notable reduction in the amount of Cu–Mn solid solution in the brazed seam, accounting for only 9.10% of the total seam area. Additionally, data from local micro-x-ray spectral analysis reveal significant disparities in the chemical composition of separate phases compared to previous samples. Specifically, the concentration of iron in the solid solution increases to approximately ≅ 6.39% when the brazing gap size is reduced to 20 μm (Fig. 7 and Table 5, spectrum 2).

The concentration of iron in the γ-phase grains $(Fe_xMn_yCo_z)Me$ also escalates to 46.13–53.58%, concurrently with an increase in cobalt concentration to 7.43–11.25% (as per point local micro-x-ray spectral analysis data). Examining the obtained microstructures reveals that in

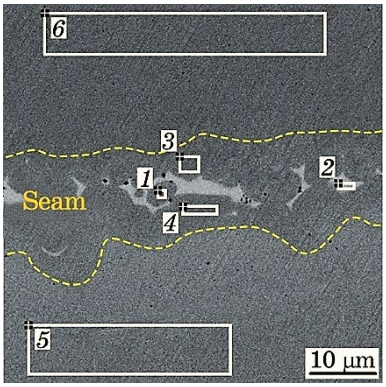

Fig. 7. Microstructure of the brazed seam of dissimilar Kovar–stainless steel joint by gap of 20 μm.

certain regions of the seam, these phase grains crystallize so closely together that they appear to amalgamate into conglomerates at the interphase boundary between the liquid filler metal and solid base metal, forming a continuous layer on the sides of both base materials: Kovar and stainless steel. It is evident that such features in the formation of the brazed seam structure can be attributed to the reduction in gap size. The vigorous interaction of the molten filler metal Cu–Mn–Co–Fe with the solid base metal during the brazing process also plays a role. Additionally, the resultant mutual diffusion processes at the filler metal-base metal interface contribute to this. These processes commence from the initial moments of the appearance of the liquid phase of the brazing filler metal [22].

Analysis of the obtained results regarding the local chemical composition of distinct phases in the brazed seam reveals (Fig. 8, *a*) that a decrease in the size of the brazing gap correlates with an increase in iron concentration in the γ-phase $(Fe_xMn_yCo_z)Me$, alongside a simultaneous reduction in manganese and cobalt content.

The reduction in gap size has minimal effect on the chemical composition of the Cu–Mn solid solution. However, it does result in a slight synchronous increase in the concentrations of Fe and Ni (Fig. 8, *b*).

It is important to note that despite the base metal remaining in the solid state during brazing, the structure and chemical composition of both the initial filler metal and the metal of the seam undergo significant disruption. Based on the results, it is possible to elucidate the underlying structural mechanism for the formation of the brazed seam. According to the chemical composition of the formed phases, the primary phase is the γ-phase $(Fe_xMn_zCo_y)Me$, as it can be associated with a higher temperature phase (Fig. 9, *a*, *b*) [23]. The secondary phase is a

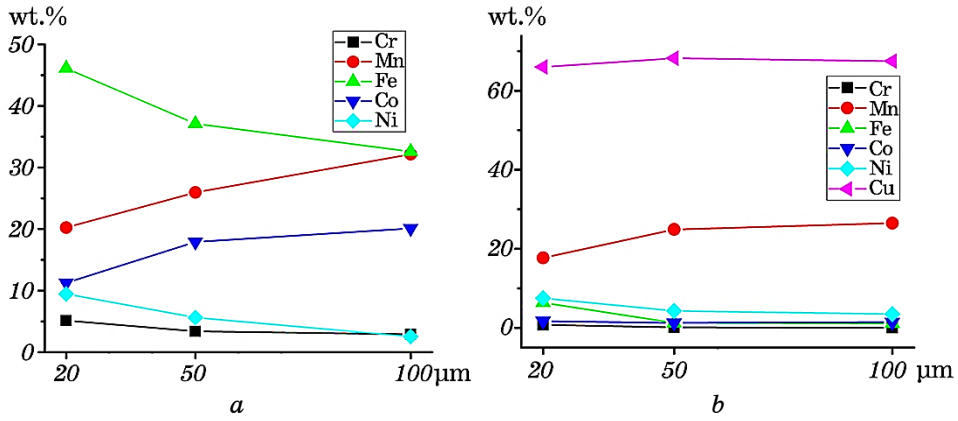

Fig. 8. Concentration of chemical elements in the γ-phase $(Fe_xMn_zCo_y)Me$ (*a*) and α-Cu solid solution (*b*) in the location depending on the size brazing gap.

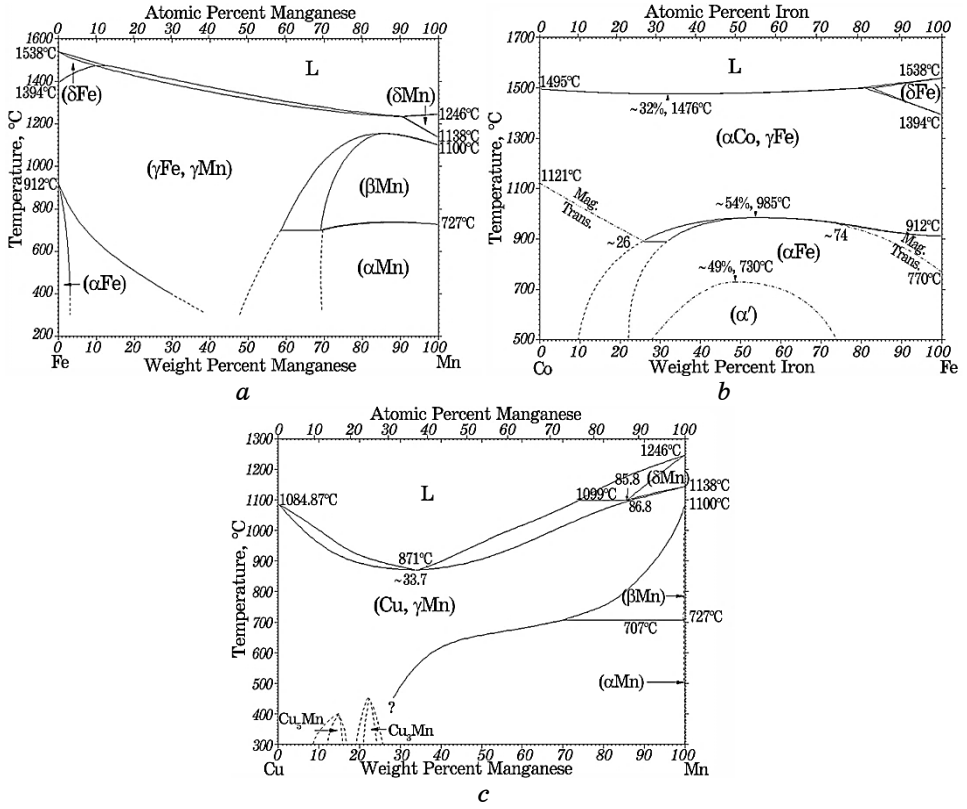

Fig. 9. Binary diagram Fe–Mn (*a*), Fe–Co (*b*), Cu–Mn (*c*).

copper-manganese solid solution, which fills the gap and crystallizes at a later stage (Fig. 9, *c*).

Furthermore, the findings from this study have demonstrated that the structure and morphological characteristics of the metal seams in brazed dissimilar joints between Kovar and stainless steel, utilizing Cu–Mn–Co–Fe filler metal, primarily hinge upon the width of the brazing gap size, thereby influencing diffusion processes. It has been established that the presence of $(Fe_xMn_yCo_z)Me$ is primarily dictated by the size of the brazing gap. Concurrently, empirical evidence has confirmed that an increase in gap size adversely influences the mechanical properties of brazed joints (Table 6), which can be attributed to the aforementioned structural attributes of brazed seams.

The brazed samples obtained with a minimum brazing gap of 20 μm exhibit maximum strength (600 MPa), with their failure occurring predominantly on the main metal—stainless steel, accompanied by minor plastic deformation. This observation underscores that the strength of a dissimilar joint obtained through brazing surpasses that of stainless

TABLE 6. Strength of brazed joints Kovar–stainless steel depending on the gap size (at 20°C).

Filler metal	Brazing gap size, μm	τ_s, MPa	σ_b, MPa	Fracture site
Cu–Mn–Co–2.5Fe	20	–	580–635	12Kh18N10T
	50	498–505	–	seam
	100	408–459	–	seam

steel subsequent to undergoing a high-temperature vacuum brazing cycle. Based on the obtained data, it is evident that the size of the brazing gap influences the morphology of the seam, the chemical composition of its separate phases, and the mechanical properties of brazed joints. The results of the conducted investigations validate the correlation between the structural attributes of brazed seams and their strength.

It is noteworthy that the trend of enhancing the mechanical properties of brazed joints with a reduction in gap size is also evident when brazing other materials (Fig. 10), such as 316 L steel utilizing BNi-2 (Ni620) filler metal [15].

This phenomenon can be attributed to the peculiarities of the microstructure following the crystallization of the brazed seam metal.

At gaps exceeding 50–60 microns, the central zone of the seam experiences the formation of brittle phases. Consequently, during mechanical tests, the failure of brazed samples is observed within these phases. Conversely, as the gap size decreases, the morphology of the brazed seams undergoes significant alterations, with the absence of brittle phases in the seams. Instead, failure occurs along the interphase boundary of the base metal and filler metal in the region where a solid solution forms [15].

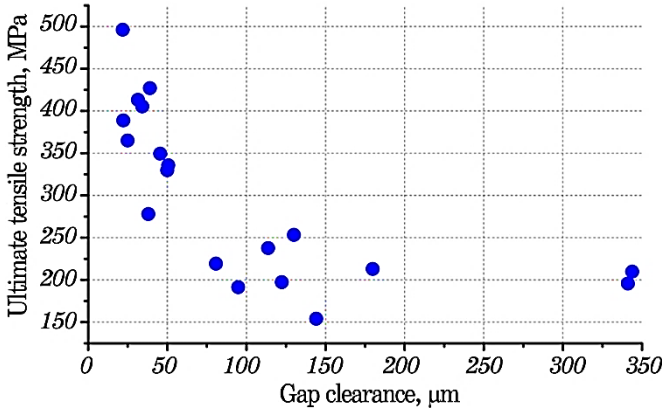

Fig. 10. Dependence of strength on gap size for BNi-2 [15].

4. CONCLUSION

Metallographic studies of dissimilar Kovar–stainless steel brazed joints confirmed the formation of a two-phase structure comprising of α-Cu solid solution (based on the Cu–Mn system) and grains of the γ-phase ($Fe_xMn_yCo_z$)*Me*. The volume ratio of these phases varies depending on the gap size. Decreasing the gap size from 100 to 20 μm results in a decrease in the solid solution amount from 86.83% to 9.10%, accompanied by a simultaneous increase in the γ-phase amount from 13.17 to 90.90%.

Reduction of the brazing gap size from 100 to 20 μm leads to an increase in iron concentration in the γ-phase from 32.58 to 46.13%, with a simultaneous decrease in manganese content from 32.16 to 20.25%, respectively. In the Cu–Mn solid solution, diminishing gap size causes a slight increase in iron amount from 1.12 to 6.39%.

Mechanical testing results indicate that reducing the brazing gap size from 100 to 50 μm enhances the shear strength of brazed joints from 408–459 to 498–505 MPa. Further reduction of the gap size to 20 μm boosts strength (up to 600 MPa), with sample failure occurring predominantly on the main metal—stainless steel with minor plastic deformation. This behaviour can be attributed to the structural characteristics of the brazed joints, notably the significant presence of the γ-phase (90.90%).

REFERENCES

1. G. J. Qiao, H. J. Wang, J. Q. Gao, and Z. H. Jin, *Mater. Sci. Forum*, **486–487**: 481 (2005).
2. Y. J. Fang, X. S. Jiang, D. F. Mo, T. F Song, Z. Y. Shao, D. G. Zhu, M. H. Zhu, and Z. P. Luo, *Adv. Mater. Sci. Eng.*, **2018**: 1 (2018).
3. G. Xia, C. Chen, J. Jia, W. Huang, H. Liu, and Y. Long, *Weld. World*, **68**: 1427 (2024).
4. B. Ahn, *Metals.*, **11**, No. 7: 1037 (2021).
5. C. Xin, Y. Jiazhen, N. Li, W. Liu, J. Du, Y. Cao, and H. Shi, *Ceram. Int.*, **42**, No.11: 12586 (2016).
6. L. F. Rudenko and T. P. Govorun, *Alloy Steels and Alloys* (Sumy: Sumy State University: 2012) (in Ukrainian).
7. S. H. Baghjari, M. Gholambargani, and S. A. A. Akbari Mousavi, *Lasers Manuf. Mater. Process.*, **6**: 14 (2019).
8. M. M. A. Fadhali, S. J. Zainal, Y. Munajat, A. Jalil, and R. Rahman, *AIP Conf. Proc.*, **1217**: 147 (2010).
9. Yu. V. Kaletina, E. D. Efimova, and M. K. Romanov, *Materials Science and Heat Treatment of Metals*, **6**: 26 (2014) (in Russian).
10. J. Feng, M. Herrmann, A.-M. Reinecke, and A. Hurtado, *J. Exp. Theor. Anal.*, **2**, No. 1: 1 (2024).
11. T. Song, X. Jiang, Z. Shao, D. Mo, D. Zhu and M. Zhu, *Metals*, **6**, No. 11: 263 (2016).

12. T. A. Mai and A. C. Spowage, *Mater. Sci. Eng. A*, **374**, Nos. 1–2: 224 (2004).
13. G. V. Ermolaev, V. V. Kvasnitsky, V. F. Kvasnitsky, S. V. Maksymova, V. F. Khorunov, and V. V. Chigarov, *Payannya Metaliv* [Brazing Materials] (Mykolaiv: NUK: 2015) (in Ukrainian).
14. V. M. Radziievskyi, A. F. Budnyk, and V. B. Yuskaiev, *Metallurgy of High-Temperature Technology of Non-Separable Joints* (Sumy: Sumy State University: 2011) (in Ukrainian).
15. E. Hedin, *Proc. of the 7th Int. Brazing and Soldering Conf. (IBSC) (Apr. 15–18, 2018, New Orleans, USA)*, p. 155–160.
16. S. V. Maksymova, V. F. Khorunov, and V. V. Voronov, *The Paton Welding J.*, **3**: 28 (2013).
17. S. V. Maksymova, P. V. Kovalchuk, V. V. Voronov, and I. I. Datsiuk, *The Paton Welding J.*, **8**: 13 (2023).
18. M. M. Shyshkov, *Marochnyk Staley i Splaviv: Dovidnyk* [Brand of Steels and Alloys: Directory] (Donetsk: 2000) (in Ukrainian).
19. https://metallicheckiy-portal.ru/marki_metallov/stk/12X18H10T
20. https://www.hightempmetals.com/techdata/hitempKovardata.php#4
21. A. M. Zakharov, *Diagrammy Sostoyaniya Dvoinykh i Troinykh Sistem* [State Diagrams of Binary and Ternary Systems] (Moskva: Metallurgiya: 1990) (in Russian).
22. S. V. Maksymova, *Current Topics and Emerging Issues in Materials Sciences*, **2**: 14 (2023).
23. T. B. Massalski, *Binary Alloy Phase Diagrams* (Materials Park, Ohio: ASM International: 1990). In CD.

Metallophysics and Advanced Technologies
Металофіз. новітні технол.
Metallofiz. Noveishie Tekhnol.
2025, vol. 47, No. 3, pp. 287–301
https://doi.org/10.15407/mfint.47.03.0287
Reprints available directly from the publisher

PACS numbers: 62.20.Qp, 62.25.Mn, 75.50.Kj, 81.20.Ev, 81.40.Ef, 81.40.Lm, 81.40.Rs

The Effect of Heat Treatment on the Physical and Mechanical Properties, and Grindability of the Amorphous $Fe_{73}Si_{16}B_7Cu_1Nb_3$ Alloy Ribbon

B. S. Baitaliuk, V. K. Nosenko, and I. K. Yevlash

G. V. Kurdyumov Institute for Metal Physics, NAS of Ukraine,
36 Academician Vernadsky Blvd.,
UA-03142 Kyiv, Ukraine

The effect of heat treatment on the physical and mechanical properties and grindability of amorphous $Fe_{73}Si_{16}B_7Cu_1Nb_3$ (of FINEMET-type) alloy ribbon is investigated. A non-monotonic dependence of microhardness, brittleness, and electrical resistivity on the annealing temperature is established. As shown, the optimum temperature, which provides the best grindability of the ribbon, is of 450°C, which is lower than the nanocrystallization temperature of this amorphous alloy. The morphology, size, and fractional composition of the grinded powder are studied using scanning electron microscopy.

Key words: FINEMET, amorphous ribbon, nanocrystalline structure, heat treatment, powder.

Досліджено вплив термічного оброблення аморфної стрічки стопу $Fe_{73}Si_{16}B_7Cu_1Nb_3$ (типу FINEMET) на фізико-механічні властивості та здатність до подрібнення. Встановлено немонотонну залежність мікротвердости, крихкости, електроопору від температури відпалу. Показано, що оптимальною температурою, яка забезпечує найліпше подрібнення стрічки є температура у 450°C, що є нижчою за температуру нанокристалізації цього аморфного стопу. З використанням електронної сканувальної мікроскопії досліджено морфологію, розміри та фракційний склад подрібненого порошку.

Ключові слова: FINEMET, аморфна стрічка, нанокристалічна структура, термооброблення, порошок.

Corresponding author: Bohdan Serhiyovych Baitaliuk
E-mail: baytalyuk@ukr.net

Citation: B. S. Baitaliuk, V. K. Nosenko, and I. K. Yevlash, The Effect of Heat Treatment on the Physical and Mechanical Properties, and Grindability of the Amorphous $Fe_{73}Si_{16}B_7Cu_1Nb_3$ Alloy Ribbon, *Metallofiz. Noveishie Tekhnol.*, **46**, No. 3: 287–301 (2024). DOI: 10.15407/mfint.47.03.0287

(Received 30 July, 2024; in final version, 1 August, 2024)

1. INTRODUCTION

Modern electronic and electrotechnical devices cannot do without inductive components such as inductors, filters, transformers, and sensors. These components often include magnetodielectrics as the basis for magnetic cores, especially considering modern trends towards miniaturization and high efficiency in electronics and microelectronics [1–8].

Along with traditional materials for the production of magnetodielectrics, which have been actively used for a long time (these are composites mainly based on iron, Sendust, Permalloy, Fe–Si system alloys and their mixtures [9–17]), composites based on powders of amorphous and nanocrystalline alloys are becoming increasingly widespread [18–23]. Alloys based on iron, cobalt, and nickel have become widely used, primarily due to their high saturation induction and low hysteresis and eddy current losses [24–27].

Among the new materials used in the production of magnetodielectrics is the FINEMET alloy, which is essentially an amorphous Fe–Si–B alloy with small admixtures of Cu and Nb [28]. The optimal composition of the alloy has hardly changed since its invention—it is $Fe_{73.5}Si_{13.5}B_9Cu_1Nb_3$ [29]. This unusual combination of elements has become the key to obtaining a nanocrystalline structure with high soft magnetic properties [30, 31].

The results of numerous studies [32–39] have shown that magnetodielectrics based on this type of alloy are today increasingly being offered with a wide range of properties according to the field of application to replace expensive Permalloy cores. The combination of high saturation induction, high permeability, good frequency dependence, low hysteresis losses and temperature stability allows reducing the weight and dimensions of the magnetic components used, for example, in pulse power supplies or telecommunications equipment. In addition to these attractive characteristics, the nanocrystalline alloy is made from inexpensive iron and silicon. All this together has led to a constantly growing application of the new alloy in magnetic choke cores, high-frequency transformers, inductors and converters for various fields of electronics and electrical engineering.

For the production of massive magnetodielectrics of various shapes and sizes, powder metallurgy methods [40–43] are mainly used, which include the following basic operations: production of powders, mixing with a binder, pressing, sintering, finishing operations. An important stage in the production of magnetodielectrics, based on nanocrystalline alloys, is the process of powders production. Physical, physical-mechanical, and magnetic properties of obtained products great extent

depend on powder performances [44].

Attempts to obtain powders from amorphous and nanocrystalline alloys have been made repeatedly [45–47]. Among the known works, those [48–53] deserve attention, in which the authors achieved the goal by mechanically grinding an amorphous or nanocrystalline ribbon. Thus, the authors of [32] obtained composites based on powders of the nanocrystalline alloy FINEMET. The powder was obtained by grinding a pre-annealed amorphous ribbon at a temperature of 573 K to make it brittle. However, along with describing all the advantages of this method, the authors limited themselves to a separate study of technological properties and practically did not consider the influence of the annealing temperature on the grindability of the ribbon, as well as such characteristics of the powder as particle size, shape, electrical resistivity, and hardness, which is important for further study of the process of forming magnetic cores from nanocrystalline powders.

In this work, the results of studying the effect of the annealing temperature of the amorphous ribbon of the $Fe_{73}Si_{16}B_7Cu_1Nb_3$ alloy (MM-11H [54]) on its plasticity, microhardness, electrical resistivity, and grindability are presented. Obtaining an amorphous powder by grinding waste from the production of an amorphous ribbon has obvious advantages and does not require complex technological equipment for its production. The powder obtained by this method has a homogeneous structure and composition, as well as minimum impurity content, which is difficult to achieve when manufacturing amorphous powder by other methods (for example, spraying or mechanical synthesis).

2. OBJECTS AND RESEARCH METHODS

Non-conforming remnants of the amorphous ribbon of the MM-11H alloy (manufactured by LLC 'MELTA') with the composition $Fe_{73}Si_{16}B_7Cu_1Nb_3$, 20 μm thick and 10 mm wide (Fig. 1), were used as the starting material for the research.

To obtain the powder and study the grindability of the ribbon, a ball mill was used, and the grinding parameters are given in Table 1.

The shape and morphology of the surface of individual powder particles were determined using a РЕМ-106*И* scanning electron microscope.

The microhardness of the ribbon was measured on ПМТ-3 microhardness meter using the Vickers method (ГОСТ ISO 6507-1:2007). The hardness value was calculated by the formula:

$$H = 1854P/d^2, \quad (1)$$

where P is the load (g), d is the diagonal of the imprint (μm).

The electrical resistance of the samples was measured using a CS4105 microohmmeter, designed to measure electrical resistance in

Fig. 1. Non-conforming remnants of the studied amorphous alloy MM-11H ribbon.

the range from 10^{-5} to 50 Ω.

To determine the brittleness of the nanocrystalline ribbon, was used a method that was described in [56]. The essence of the method is that the ribbon is clamped between two micrometer jaws, as shown in Fig. 2, which is compressed until destruction.

Relative deformation before destruction in the surface zone of the ribbon is taken as the criterion of brittleness. The parameter of brittleness is the value ε_f:

TABLE 1. Technological parameters of obtaining powder of nanocrystalline alloy MM-11H by grinding in a ball mill. n_{cr} is the critical rotational speed of the mill, at which balls 'stick' to the drum walls [55].

Technological parameter	Optimal values	Used values	Notes
Drum diameter D, cm	–	20	Drum volume: 7.22 l
Drum rotation speed, rpm	$(0.75–0.8)n_{cr}$	95	$n_{cr} = 42.4D^{-1/2}$
Ball-to-material mass ratio	2.5–6	5.5	Ball mass: 12.2–13.7 kg
Mill filling coefficient	0.4–0.5	0.5	$V_{material}/V_{drum}$
Grinding environment	Alcohol	Alcohol	Contributes to the intensification of grinding
Grinding time, min	30–60	60	To obtain the desired fraction

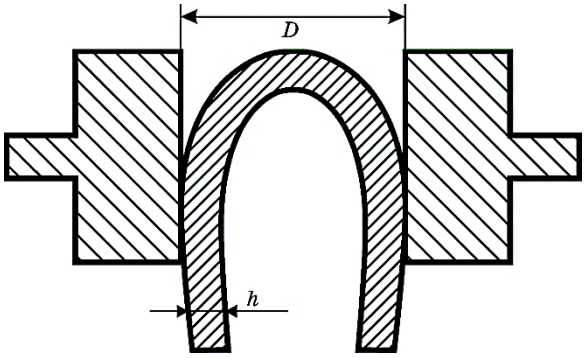

Fig. 2. Scheme of the installation for determining the brittleness of the nanocrystalline ribbon.

$$\varepsilon_f = h/(D - h), \tag{2}$$

where h is the thickness of the ribbon, D is the distance between the micrometer jaws between which the bending is carried out at the moment of the ribbon destruction.

The obtained values of ε_f were averaged over the data of 5 measurements, excluding the results in which the brittleness was several times higher than in most measurements.

The heat treatment of the amorphous ribbon was carried out at temperatures of 200–600°C in air, with a holding time of 30, 60, and 90 minutes for each individual experiment.

3. RESULTS AND DISCUSSION

3.1. Brittleness of the Ribbon

As known, pressing is an important stage in the manufacture of powder parts, including cores. The ability to compact powder samples is strongly influenced by the shape and plasticity of the powder particles, and to a lesser extent by the surface condition and the coefficient of friction between the particles and the walls of the mould. Since the shape of the powder particles produced by the mechanical grinding of the ribbon is always the same (plate-like, flaky), the main indicator of the ability of amorphous and nanocrystalline powders to deform can be the level of their plasticity (which can be indirectly judged by the level of their hardness). For powder soft magnetic composites, lower microhardness usually contributes to better compaction, higher strength, better magnetic properties of finished products, and less wear of mould parts during the forming process.

Additionally, it is worth noting that the choice of annealing temper-

ature and duration is of strategic importance. Annealing at low temperatures may not provide sufficient brittleness for effective grinding, while high temperatures can lead to unwanted boride crystallization and loss of magnetic properties. Thus, the ideal annealing temperature for the MM-11H alloy is in the range that provides optimal brittleness without the risk of crystallization.

At the first stage, the amorphous ribbon was subjected to heat treatment to increase its brittleness. For this purpose, it was annealed at temperatures of 200, 300, 450, 530 and 600°C for 30, 60 and 90 minutes (in air). It is not advisable to use high temperatures, since above 600°C for the studied alloy, rapid crystallization processes begin and it loses its magnetic properties [28, 57, 58].

To determine the grindability of the ribbon, the loss of its plasticity (embrittlement) as a function of the annealing temperature was investigated. A typical curve of the dependence of the brittleness of amorphous alloys on the annealing temperature is shown in Fig. 3.

It is easy to see in Fig. 3 and expression (2) that in a completely plastic state (when the ribbon bends without destruction) $D = 2h$ and $\varepsilon_f = 1$. The higher the value of D, the higher the degree of brittleness. In absolute brittleness, $D \to \infty$ and $\varepsilon_f \to 0$.

The dependence of the relative deformation to fracture of the MM-11H alloy ribbon on the annealing temperature and time is shown in Fig. 4.

The nature of the curve's behaviour shows that in the initial state, the amorphous ribbon has high plasticity, strength, and hardness, the absence of deformation hardening, and very small values of macroscopic deformation before destruction. However, after annealing at a temperature above a certain critical temperature, it transitions into a brittle state. This phenomenon of loss of plasticity within the amor-

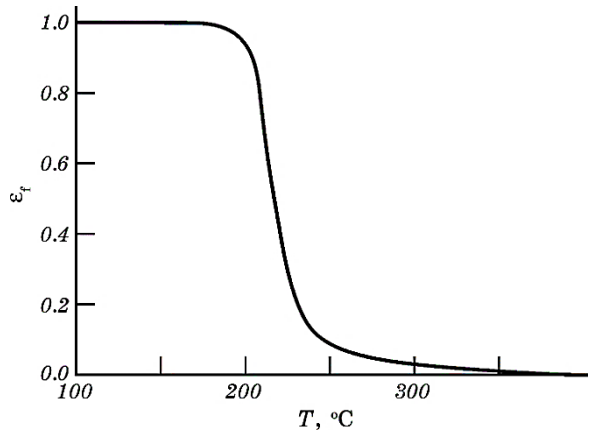

Fig. 3. Typical curve of the dependence of the brittleness of amorphous alloys on the annealing temperature [56].

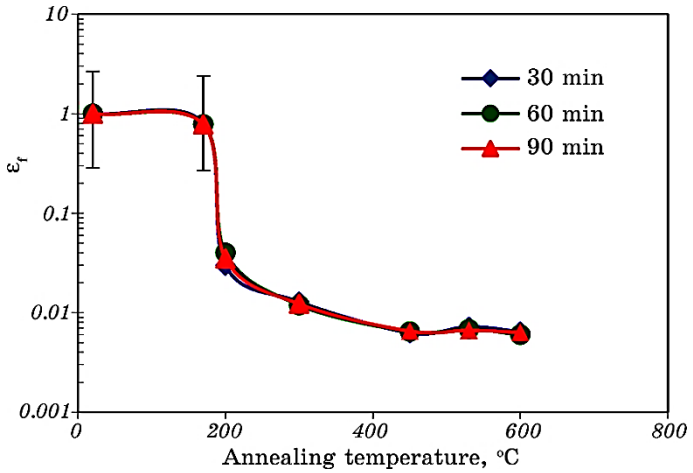

Fig. 4. Dependence of the relative deformation before destruction of the MM-11H alloy ribbon on the annealing temperature and time.

phous state is called annealing brittleness of amorphous alloys [59].

The transition temperature from the plastic state to the brittle state for the alloy under study is about 200°C, as can be seen from Fig. 4. It has been established that the annealing duration within 30–90 minutes does not affect the deformation value before destruction, since the alloy acquires these properties in the first minutes of annealing [56]. More accurate results of the acquisition of brittleness by the ribbon at the initial stages of crystallization do not seem possible due to the small thickness of the ribbon and the large error in measuring the fracture distance of less than 0.1 mm.

It is interesting that at a temperature of 530°C, a slight increase in plasticity is observed, and this change looks the same for each annealing time. This can be seen in detail from Fig. 5, where the distance (*D* in millimetres) at which the 20 μm thick ribbon breaks is plotted on the ordinate axis instead of the deformation value before destruction ε_f.

Such behaviour of the curves in amorphous-nanocrystalline Fe-based alloys can be caused by various factors such as crystallization, enrichment with soluble elements, phase separation, free volume annihilation, and residual stress. The exact cause of annealing brittleness remains is unknown [60].

The authors of [61] investigated the effect of annealing temperature on the mechanical and structural transitions of the nanocrystalline Fe–Si–B alloy ribbon. They concluded that the initial drop in plasticity could be explained by the release of free volume and an increase in the volume of the shear transformation zone volume. The release of free volume leads to structural relaxation of residual stresses. In addition, a slight dip in the brittleness curve in the crystallization temperature

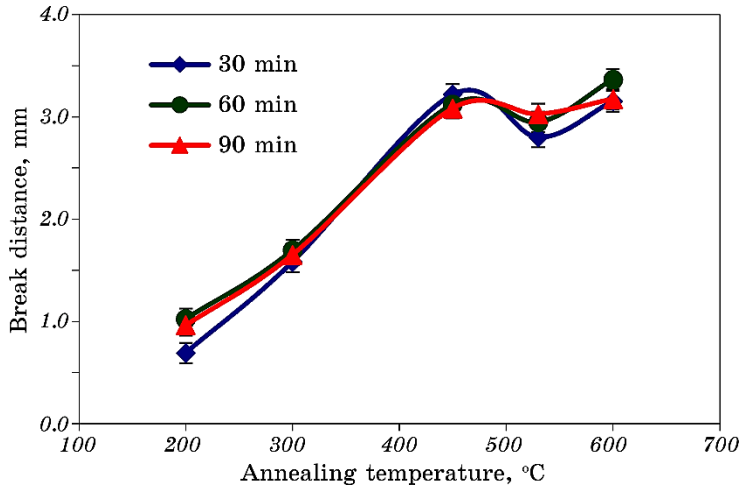

Fig. 5. Dependence of the fracture distance of the 20 μm thick MM-11H alloy ribbon on the annealing temperature and time.

range is due to the very beginning of nanocrystallization and a decrease in internal stresses.

In our case, at a temperature of 530–570°C, nanocrystallization of the alpha-solid solution of silicon in iron (with a b.c.c. lattice) occurs rapidly [28, 57]. The general microstructure is characterized by randomly oriented ultrathin grains of b.c.c. Fe(Si) (20 at.% Si) with an average grain size of 10–15 nm within the amorphous matrix, which occupies 20–25% of the total volume of the ribbon. This structure is the basis for unique soft magnetic properties.

It should be noted that the optimal volume ratio between iron nanocrystals and the amorphous matrix is not achieved immediately, nor is the optimal silicon content in nanocrystals. It is achieved after a certain period of time and at a certain optimal temperature, which, due to the intense mechanical effect on the initial structure of the ribbon, may change for the ground powder compared to the ribbon.

3.2. Microhardness of the Ribbon

Figure 6 shows the dependence of the microhardness of the MM-11H ribbon on the annealing temperature and time.

As can be seen in Fig. 6, at annealing temperatures up to 450°C, the microhardness of the ribbon almost does not change (in comparison with the initial state) and reaches ≅ 800 kg/mm^2. Starting from a temperature of 450°C, the microhardness of the alloy begins to grow rapidly and increases almost twice by the time it reaches 600°C. Moreover, the annealing time within 30–90 minutes does not affect the hardness

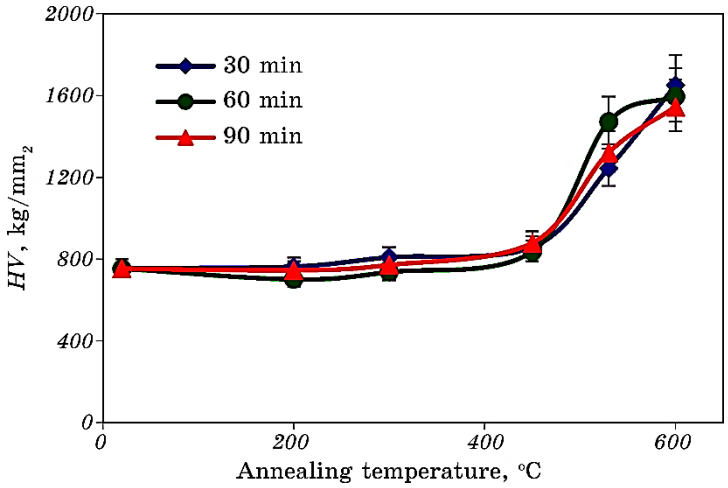

Fig. 6. Dependence of the microhardness of the MM-11H alloy ribbon on the annealing temperature and time.

in any way (the slight discrepancy in values can be explained by the measurement error).

A characteristic feature of the MM-11H alloy is also that the microstructure (as well as the soft magnetic properties) does not strongly depend on the annealing temperature (T_a) in the range $\Delta T_a = 50–100$°C. The main process takes place in the first 10–15 minutes and does not strongly depend on the subsequent nanocrystallization time. However, increasing the annealing temperature above approximately 600°C leads to both rapid growth of nanograins to micron sizes and crystallization of the residual amorphous phase with the formation of Fe_2B and Fe_3B borides [28, 57, 62].

3.3. Electrical Resistivity of the Ribbon

One of the important properties that magnetodielectrics must have is high specific electrical resistivity. The low eddy current losses of amorphous and nanocrystalline alloys are due to the fact that they have a relatively lower specific electrical conductivity, in particular, compared to pure iron, electrical steels or Permalloys.

As is known, losses in magnetic materials are divided into three categories:

$$P = P_h + P_e + P_{ex}, \tag{3}$$

where P_h is hysteresis loss, P_e is eddy current loss, P_{ex} is excess loss.

The nature of excess losses is not yet well understood. These losses

depend on the mechanical stresses arising in the material and resonant losses. They appear at very low induction values and very high frequencies, so these losses are usually ignored. Therefore, the main losses in the core are hysteresis losses and eddy current losses.

The dependence of the electrical resistivity of the MM-11H alloy ribbon on the annealing temperature is shown in Fig. 7.

Figure 7 shows that in the unannealed state, the ribbon has an electrical resistivity of $1.9 \cdot 10^{-6}$ μΩ·m, which is consistent with the literature data for amorphous ribbons: 100–300 μΩ·cm, including the review work by the authors [63]. This is an order of magnitude higher than that of pure iron ($0.1 \cdot 10^{-6}$ μΩ·m), and much higher than that of electrical steels (0.25–0.6 μΩ·m), Sendust (0.8 μΩ·m), molybdenum Permalloy (0.6 μΩ·m), and iron–nickel Permalloy (0.45 μΩ·m), which are often used as magnetic conductors. The electrical resistivity of the MM-11H amorphous ribbon even exceeds the values of nichrome (1.1 μΩ·m) or FeCrAl (1.2–1.4 μΩ·m) alloys. Such a high electrical resistivity of this alloy explains its low total magnetization losses, including low eddy current losses when used in transformer and choke cores at medium and high frequencies [62].

As the annealing temperature increases (as can be seen in Fig. 7), the electrical resistivity of the ribbon begins to decrease rapidly with increasing annealing temperature above 450°C. At a temperature of 600°C, the electrical resistivity decreases to $1.3 \cdot 10^{-6}$ Ω·m, which is one and a half times less than the initial resistance of the ribbon in the unannealed state, and this is obviously due to the complete nanocrystallization of the ribbon [28, 60].

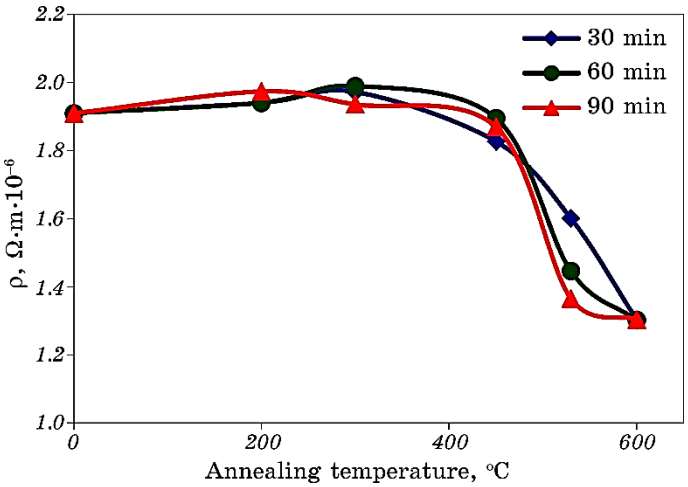

Fig. 7. Dependence of the electrical resistivity of the MM-11H alloy ribbon on the annealing temperature and time.

3.4. Grindability of the Ribbon

For a practical study of the grindability of the ribbon, it was ground in a ball mill for 1 hour in an alcohol medium. For this, the ribbon was first annealed at temperatures of 200, 300, 450, and 530°C, grinded, and then the resulting powder was sieved into fractions with different sets of sieves.

The morphology and shape of the powder particles obtained after grinding the ribbon are shown in Fig. 8.

As can be seen from the photo, all powder particles have a lamellar (flake) shape, which indicates brittle destruction of the alloy.

The results of the sieve analysis are shown in Fig. 9. Analysis of the data shows that with increasing annealing temperature, the grindability of the ribbon increases and the content of fine fractions increases. At an annealing temperature of 200°C, large fractions with a powder particle size of 0.4 to 7 mm predominate, which indicates insufficient

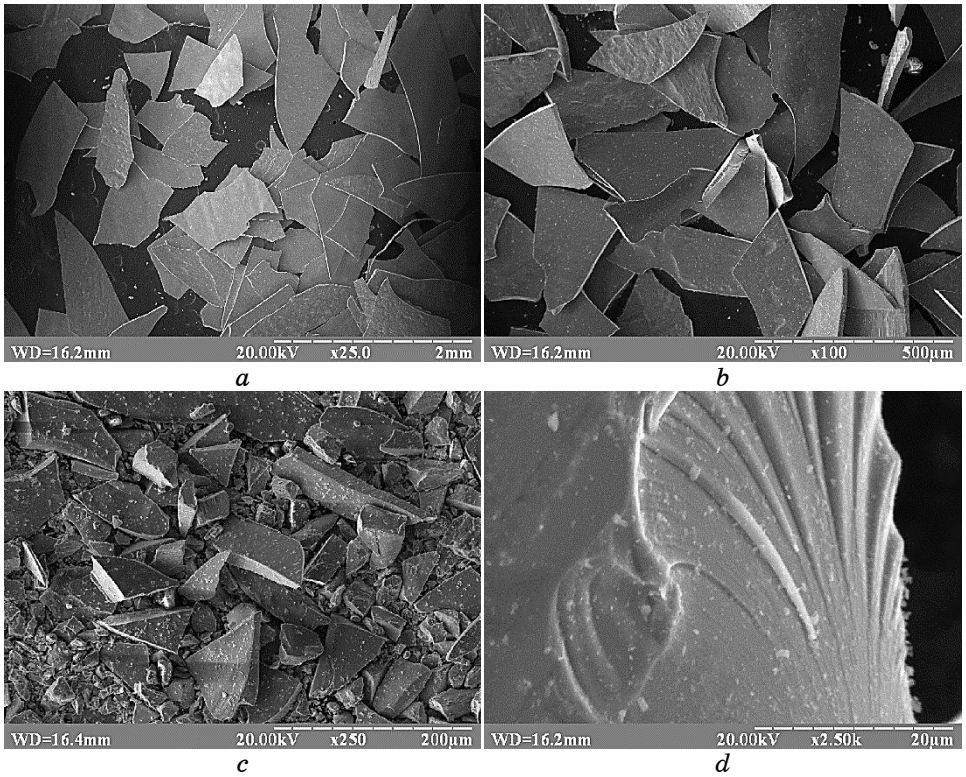

Fig. 8. Shape of MM-11H alloy powder particles from the ribbon annealed at 450°C: fraction 500–2500 µm (*a*), fraction 80–160 µm (*b*), fraction < 50 µm (*c*), fracture surface (*d*).

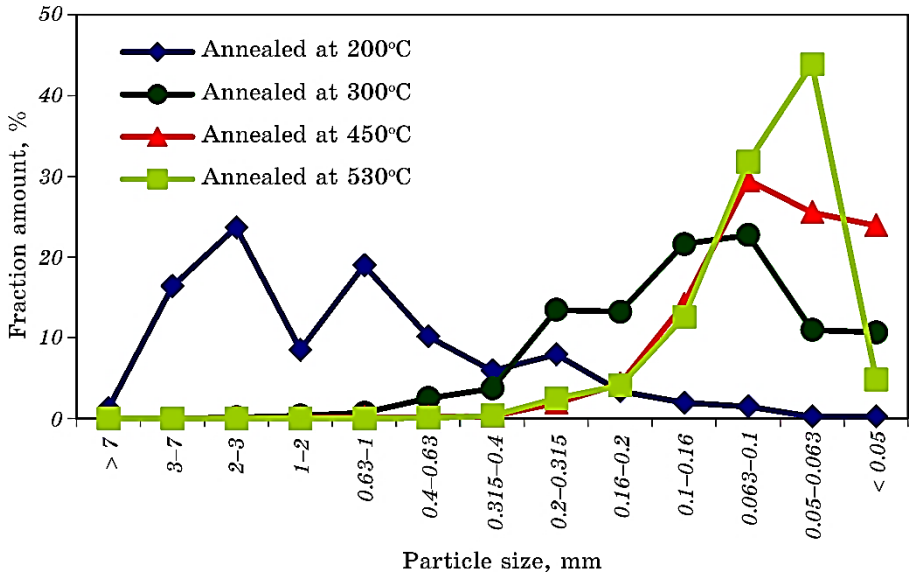

Fig. 9. Fractional composition of the MM-11H nanocrystalline alloy powder after 1 hour of grinding from an amorphous ribbon annealed at temperatures of 200–530°C.

brittleness of the alloy. Such fractions are usually not used for the production of magnetodielectrics, as they are poorly pressed. At an annealing temperature of 300°C, fractions with particles of 0.2–0.063 mm in size predominate, which is already a technologically acceptable size for pressing and manufacturing magnetic conductors. The smallest powder fractions were obtained from the ribbon annealed at 450°C (with the main content of the fraction less than 0.1 mm).

However, at 530°C, a decrease in the amount of the smallest fractions (less than 50 μm) is observed, which may be associated with the deformation hardening of the ribbon when it contains 75–80% of the volume of nanocrystals [60], which negatively affects its grindability.

The practical significance of the results obtained, presented in Figs. 5, 6, and 8, lies in establishing the optimal regimes of pre-annealing and grinding of the amorphous ribbon to obtain an amorphous-nanocrystalline powder of the required (adjustable) fractional composition with minimal microhardness (lower microhardness—better pressing ability of the powder) and the highest electrical resistance (which reduces eddy current losses).

4. CONCLUSIONS

It is shown that the annealing temperature is a key factor that affects

the physical and mechanical properties of the amorphous ribbon of the $Fe_{73}Si_{16}B_7Cu_1Nb_3$ (MM-11H) alloy.

It is established that with increasing pre-annealing temperature above 200°C, the amorphous ribbon almost completely loses its plasticity and turns into a brittle state. In this case, as well as in the annealing temperature range up to 450°C, the microhardness of the ribbon remains practically unchanged (800 kg/mm^2), while an increase in temperature to 600°C leads to an increase in it by almost 2 times.

At the same time, with increasing annealing temperature above 450°C, there is a decrease in the electrical resistivity from $1.9 \cdot 10^{-6}$ μΩ·m to $1.3 \cdot 10^{-6}$ μΩ·m after heat treatment at 600°C, which is caused by the development of nanocrystallization processes in the amorphous ribbon. This value of the electrical resistivity of the nanocrystalline ribbon of the MM-11H alloy is significantly higher than that of industrial crystalline soft magnetic alloys, which are used as a material for the manufacture of magnetic conductors. Such a high specific electrical resistance of this alloy leads to a low level of watt losses for eddy currents when used in transformers and chokes at medium and high frequencies.

It is established that the highest grindability of the amorphous ribbon is achieved after its heat treatment in air at 450°C for 30 minutes. As a result of such treatment, a powder fraction of the smallest size was obtained 100 ± 50 μm.

The results of this study are already being used by the authors to optimize the processes of manufacturing metal-polymer magnetodielectrics based on the nanocrystalline powder of the $Fe_{73}Si_{16}B_7Cu_1Nb_3$ (MM-11H) alloy, as well as in the development of new soft magnetic nanostructured alloys with improved magnetic properties.

REFERENCES

1. O. Gutfleisch, M. Willard, E. Brück, C. Chen, S. Sankar, and J. P. Liu, *Adv. Mater.*, **23**, Iss. 7: 821 (2011).
2. A. M. Leary, P. R. Ohodnicki, and M. E. McHenry, *JOM*, **64**: 772 (2012).
3. S. Wu, W. Hu, Q. Ze, M. Sitti, and R. Zhao, *Multifunctional Mater.*, **3**, No. 4: 042003 (2020).
4. A. Talaat, M. V. Suraj, K. Byerly, A. Wang, Y. Wang, J. K. Lee, and P. R. Ohodnicki, *J. Alloys Compd.*, **870**: 159500 (2021).
5. T. N. Lamichhane, L. Sethuraman, A. Dalagan, H. Wang, J. Keller, and M. P. Paranthaman, *Mater. Today Phys.*, **15**: 100255 (2020).
6. Q. Lu, K. Choi, J.-D. Nam, and H. J. Choi, *Polymers*, **13**, Iss. 4: 512 (2021).
7. J. M. Silveyra, E. Ferrara, D. L. Huber, and T. C. Monson, *Science*, **362**: eaao0195 (2018).
8. *Interdisciplinary Engineering Sciences Concepts, Researches and Applications* (Ed. S. Islak) (Lyon: 2022).
9. B. S. Baitalyuk, V. A. Maslyuk, S. B. Kotlyar, and Ya. A. Sytnyk, *Powder Metall. Met. Ceram.*, **55**: 496 (2016).

10. J. L. Ni, F. Duan, S. J. Feng, F. Hu, X. C. Kan, and X. S. Liu, *J. Alloys Compd.*, **897**: 163191 (2022).
11. G. E. Fish, *Proc. IEEE*, **78**, No. 6: 947 (1990).
12. W. Li, Y. Zheng, Y. Kang, A. Masood, Y. Ying, J. Yu, J. Zheng, L. Qiao, J. Li, and S. Che, *J. Alloys Compd.*, **819**: 153028 (2020).
13. G. Ouyang, X. Chen, Y. Liang, C. Macziewski, and J. Cui, *J. Magn. Magn. Mater.*, **481**: 234 (2019).
14. B. D. Cullity and C. D. Graham, *Introduction to Magnetic Materials* (John Wiley and Sons: 2011).
15. F. Fiorillo, *Characterization and Measurement of Magnetic Materials* (Academic Press: 2004).
16. Z. Y. Wu, Z. Jiang, X. A. Fan, L. J. Zhou, W. L. Wang, and K. Xu, *J. Alloys Compd.*, **742**: 90 (2018).
17. Z. Zheng, S. Li, and K. Peng, *J. Magn. Magn. Mater.*, **568**: 170423 (2023).
18. D. Azuma, N. Ito, and M. Ohta, *J. Magn. Magn. Mater.*, **501**: 166373 (2019).
19. R. Hasegawa, *J. Magn. Magn. Mater.*, **324**: 3555 (2012).
20. S. Lu, M. Wang, and Z. Zhao, *J. Non-Cryst. Solids*, **616**: 122440 (2023).
21. X. Wang, Z. Lu, C. Lu, G. Li, and D. Li, *J. Iron Steel Res. Int.*, **21**: 1055 (2014).
22. C. Chang, J. Guo, Q. Li, S. Zhou, M. Liu, and Y. Dong, *J. Alloys Compd.*, **788**: 1177 (2019).
23. R. Ma and P. Yu, *Mater. Res. Bull.*, **139**: 111256 (2021).
24. H. Shokrollahi and K. Janghorban, *J. Mater. Process. Technol.*, **189**, Iss. 1–3: 1 (2007).
25. A. Krings, A. Boglietti, A. Cavagnino, and S. Sprague, *IEEE Trans. Ind. Electron.*, **64**, Iss. 3: 2405 (2017).
26. K. L. Alvarez, H. A. Baghbaderani, J. M. Martín, N. Burgos, M. Ipatov, Z. Pavlovic, and J. Gonzalez, *J. Magn. Magn. Mater.*, **501**: 166457 (2020).
27. Y. Yoshizawa, S. Fujii, D. H. Ping, M. Ohnuma, and K. Hono, *Scr. Mater.*, **48**, Iss. 7: 863 (2003).
28. *Handbook of Magnetic Materials. Vol. **10*** (Ed. K. H. J. Buschow) (Elsevier: 1997).
29. Y. Yoshizawa, S. Oguma, and K. Yamauchi, *J. Appl. Phys.*, **64**: 6044 (1988).
30. M. Manivel Raja, N. Ponpandian, B. Majumdar, A. Narayanasamy, and K. Chattopadhyay, *Mater. Sci. Eng. A*, **304–306**: 1062 (2001).
31. G. Herzer, *Acta Mater.*, **61**, Iss. 3: 718 (2013).
32. H. Sun, C. Wang, J. Wang, M. Yu, and Z. Guo, *J. Magn. Magn. Mater.*, **502**: 166548 (2020).
33. Z. Guo, J. Wang, W. Chen, D. Chen, H. Sun, Z. Xue, and C. Wang, *Mater. Des.*, **192**: 108769 (2020).
34. T. Zhou, Y. Liu, R. Wang, J. Ye, J. Li, W. Zhao, and V. G. Harris, *J. Alloys Compd.*, **791**: 1138 (2019).
35. C. Wu, H. Chen, H. Lv, and M. Yan, *J. Alloys Compd.*, **673**: 278 (2016).
36. H. Chen, J. Xu, C. Wang, R. Fu, Z. Fu, Q. Chen, and X. Liu, *Ceram. Int.*, **50**, Iss. 19, Pt. A: 35746 (2024).
37. H. Wei, H. Yu, Y. Feng, Y. Wang, J. He, and Z. Liu, *Mater. Chem. Phys.*, **263**: 124427 (2021).
38. X. Li, Y. Dong, X. Liu, S. Wu, R. Zhao, H. Wu, W. Gao, A. He, J. Li, and X. Wang, *Mater. Sci. Eng. B*, **285**: 115965 (2022).
39. B. Wang, Z. Zhang, J. Shen, Y. Tian, B. Wang, L. Cai, L. Liu, Y. Yu, and

G. Wang, *J. Alloys Compd.*, **972**: 172812 (2024).
40. K. J. Sunday and M. L. Taheri, *Metal Powder Rep.*, **72**, Iss. 6: 425 (2017).
41. H. G. Rutz, F. G. Hanejko, and G. W. Ellis, *PM2TEC '97: Powder Metallurgy and Particulate Materials (June 29–July 2, 1997)* (Chicago: 1997).
42. W. Lu, B. Yan, and R. Tang, *J. Alloys Compd.*, **425**: 406 (2006).
43. P. Wang, Z. Zhu, J. Liu, H. Wang, J. Pang, and J. Zhang, *J. Magn. Magn. Mater.*, **596**: 171985 (2024).
44. E. Périgo, B. Weidenfeller, P. Kollár, and J. Füzer, *Appl. Phys. Rev.*, **5**: 031301 (2018).
45. M. Liu, K. Huang, L. Liu, T. Li, P. Cai, Y. Dong, and X.-M. Wang, *J. Mater. Sci. Mater. Electron.*, **29**: 6092 (2018).
46. I. Otsuka, K. Wada, Y. Maeta, T. Kadomura, and M. Yagi, *IEEE Trans. Magn.*, **44**, Iss. 11: 3891 (2008).
47. L. Zhang, Y. Wu, Y. Dong, X. Jia, A. He, J. Li, W. Wang, and B. Shen, *J. Mater. Sci.*, **59**: 8784 (2024).
48. V. A. Maslyuk, B. S. Baitalyuk, and V. K. Nosenko, *Naukovi Notatky. Inzhenerna Mekhanika*, **25**, No. 2: 150 (2009) (in Ukrainian).
49. P. Gramatyka, R. Nowosielski, P. Sakiewicz, and T. Raszka, *J. Achiev. Mater. Manuf. Eng.*, **150**, Nos. 1–2: 27 (2006).
50. P. Gramatyka and R. Nowosielski, *Advances in Nanostructured Materials, Processing–Microstructure–Properties NANOVED 2006–NENAMAT (May 14–17, 2006)* (Bratislava: Slovak Academy of Sciences: 2006), p. 81.
51. F. Mazaleyrat and L. Varga, *J. Magn. Magn. Mater.*, **215–216**: 253 (2000).
52. B. Zhou, M. Lv, J. Wu, B. Ya, L. Meng, L. Jianglin, and X. Zhang, *Mater.*, **15**: 2558 (2022).
53. R. M. Aranda, R. Astacio, P. Urban, B. Aranda, and F. G. Cuevas, *Powder Technol.*, **441**: 119816 (2024).
54. *Melta* www.melta.com.ua.
55. H. Watanabe, *Powder Technol.*, **104**, Iss. 1: 95 (1999).
56. A. M. Glezer and N. A. Shurygina, *Amorfno-Nanokristallicheskie Splavy* [Amorphous-Nanocrystalline Alloys] (Moskva: Fizmatlit: 2013) (in Russian).
57. V. V. Maslov, V. K. Nosenko, L. E. Taranenko, and A. P. Brovko, *Fiz. Met. Metalloved.*, **91**, No. 5: 47 (2001) (in Russian).
58. V. V. Nemoshkalenko, L. E. Vlasenko, A. V. Romanova, V. V. Maslov, V. K. Nosenko, and A. P. Brovko, *Metallofiz. Noveishie Tekhnol.*, **20**, No. 6: 22 (1998).
59. S. P. Hozhii, *Osnovy Fizyko-Tekhnichnykh ta Khimiko-Termychnykh Protsesiv dlya Pidvyshchennya Resursu Vyrobiv Mashynobuduvannya* [Basics of Physico-Technical and Chemical-Thermal Processes for Increasing the Resource of Mechanical Engineering Products] (Kyiv: National Technical University of Ukraine 'Igor Sikorsky Kyiv Polytechnic Institute': 2022) (in Ukrainian)
60. J. Zhou, J. You, and Q. Keqiang, *J. Appl. Phys.*, **132**: 040702 (2022).
61. C. Minnert, M. Kuhnt, S. Bruns, A. Marshal, K. G. Pradeep, M. Marsilius, E. Bruder, and K. Durst, *Mater. Des.*, **156**: 252 (2018).
62. V. K. Nosenko, *Visnyk Natsionalnoi Akademii Nauk Ukrainy*, **4**: 68 (2015) (in Ukrainian).
63. M. P. Semenko, M. I. Zakharenko, Yu. A. Kunytskyi, V. A. Makara, and A. P. Shpak, *Usp. Fiz. Met.*, **10**: 131 (2009) (in Ukrainian).

Metallophysics and Advanced Technologies
Металофіз. новітні технол.
Metallofiz. Noveishie Tekhnol.
2025, vol. 47, No. 3, pp. 303–333
https://doi.org/10.15407/mfint.47.03.0303
Reprints available directly from the publisher

PACS numbers: 46.35.+z, 61.72.Bb, 61.72.Lk, 62.20.fg, 81.40.Cd, 83.60.La

The Effect of the Shear-Stress Field in the Glide Plane on Solid Solution Strengthening in Multicomponent Alloys

M. I. Lugovyy, D. G. Verbylo, and M. P. Brodnikovskyy

I. M. Frantsevych Institute for Problems in Materials Science, N.A.S. of Ukraine,
3, Omeljan Pritsak Str.,
UA-03142 Kyiv, Ukraine

Atomic-sizes' misfit and elastic-moduli misfit for the solute atoms at the crystal-lattice sites in concentrated solid solution, notably, in multicomponent alloy, can be considered as discrete random variables. Definition of variance of such random variables allows to develop method and analytical expressions to determine the main parameters of stochastic shearing-stresses' field that is generated within the glide plane by solute atoms. The main parameters are the standard deviations and correlation lengths of the short- and long-wavelength components of this field. The developed method also shows that it is possible to determine two different effective distortions of crystal lattice, each of which is responsible for its own component of the shearing-stresses' field. Another conclusion of the new method is that there is no single empirical constant for all alloys at once to determine the yield strength using the shear modulus and average lattice distortion. The short-wavelength component of the shearing-stresses' field within the glide plane creates dominant force barriers, which the dislocation can overcome by the thermal-activation assistance. The long-wavelength component creates barriers, which can be overcome athermally, that is, by applying additional mechanical stress. All these barriers can be described using the main parameters of the shearing-stresses' field. Effect of solute atoms located farther from the glide plane on yield strength cannot be neglected because they create long-wavelength component of the shearing-stresses' field. The analysis of

Corresponding author: Mykola Ivanovych Lugovyy
E-mail: m.lugovyi@ipms.kyiv.ua

Citation: M. I. Lugovyy, D. G. Verbylo, and M. P. Brodnikovskyy, The Effect of the Shear Stress Field in the Glide Plane on Solid Solution Strengthening in Multicomponent Alloys, *Metallofiz. Noveishie Tekhnol.*, **47**, No. 3: 303–333 (2025). DOI: 10.15407/mfint.47.03.0303

overcoming barriers from the short- and long-wavelength components of the shearing-stresses' field is resulted in describing the temperature dependence of the yield strength of a multicomponent alloy. This dependence describes well the mechanical behaviour of the alloy in a wide range of temperatures, including in the range of the high-temperature 'plateau', except very low and very high temperatures, where additional factors and mechanisms operate.

Key words: multicomponent alloy, solid solution, glide plane, shearing stresses, dislocation, yield strength.

Невідповідності атомових розмірів і модулів пружности для розчинених атомів у вузлах кристалічних ґратниць концентрованого твердого розчину, який являє собою багатокомпонентний стоп, можна розглядати як дискретні випадкові величини. Визначення дисперсії цих випадкових величин уможливлює розробити метод розрахунку й одержати аналітичні вирази для основних параметрів поля стохастичних зсувних напружень, яких зґенеровано у площині ковзу розчиненими атомами. Основними параметрами є стандартні відхили та довжини кореляції коротко- та довгохвильової компонент цього поля. Розроблений метод також показує, що можна визначити дві різні ефективні дисторсії кристалічних ґратниць, кожна з яких відповідає за свою компоненту поля зсувних напружень. Ще один висновок нового методу: немає єдиної емпіричної константи одразу для всіх стопів, щоб визначити границі плинности через модуль зсуву та середню дисторсію ґратниць. Короткохвильова компонента поля зсувних напружень у площині ковзу створює домінантні силові бар'єри, які дислокація може долати за допомогою термічної активації. Довгохвильова компонента створює бар'єри, які можуть бути подолані атермічно, тобто шляхом прикладання додаткового механічного напруження. Всі ці бар'єри можна описати за допомогою основних параметрів поля зсувних напружень. Не можна нехтувати впливом атомів розчиненої речовини, розташованих далі від площини ковзу, на границю плинности, оскільки вони створюють довгохвильову компоненту поля зсувних напружень. Аналіза подолання бар'єрів від коротко- та довгохвильової компонент поля зсувних напружень дає нам температурну залежність границі плинности багатокомпонентного стопу, яка може добре описати механічну поведінку стопу в широкому діяпазоні температур, в тому числі й в області високотемпературного «плато», за винятком дуже низьких і дуже високих температур, де діють додаткові чинники та механізми.

Ключові слова: багатокомпонентний стоп, твердий розчин, площина ковзу, зсувні напруження, дислокації, межа плинности.

(Received 6 June, 2024; in final version, 14 October, 2024)

1. INTRODUCTION

Multicomponent alloys are promising materials that demonstrate many unique properties, in particular, very high yield strengths [1, 2]. The yield strength of such alloys, which are mostly substitutional solid

solutions, depends on the distribution of internal stresses in the material. It should be noted that the distribution of internal stresses affects the shape of the dislocation line, which also affects the stress required to start its movement in the glide plane [3]. Solid solution strengthening allows achieving high yield strength in multicomponent alloys even at high temperatures. Thus, the concept of solid solution strengthening allows obtaining materials for applications in a wide range of temperatures [1]. Such features of the mechanical behaviour of these materials are very useful for use in modern technology [1, 2].

Crystal lattice distortion created by solute atoms results in stochastic shear stresses in the dislocation glide plane. The different atoms in the solid solution have some atomic size misfit and elastic modulus misfit in comparison with the average atomic size and the effective elastic modulus of the alloy. These misfits lead to distortion of the crystal lattice, which varies randomly in space. Local distortion changes with temperature, and understanding the features of these changes is important for determining the temperature dependence of the material's yield strength. In such a way, crystal lattice distortion is a source of internal stresses. In the case of alloys where there is no dominant component, the internal shear stress at any point of glide plane is a random variable, which typically has a statistical distribution according to the normal law, because these stresses are the sum of contributions of many solute atoms, which are located around the glide plane. In general, these internal stresses follow a zero balance, that is, the stress averaged over the entire glide plane must be zero. Regions with stresses of different signs alternate with each other on the glide plane, which results in a zero balance of forces. The average size of the region where the stresses have the same sign is an important characteristic of the stochastic shear-stress field, which determines its correlation length. These stresses lead to forces acting on the dislocation, affecting its shape, and creating resistance to its movement due to the deviation of dislocation shape from a straight line. The wavy equilibrium shape of the dislocation is formed by the balancing of the forces acting on individual segments of the dislocation due to shear-stress field and the forces of linear tension, which in turn depend on the shape of the dislocation line. Thus, this shape is a set of ‘waves’, *i.e.*, bulges of different lengths and heights. To estimate the parameters of the average bulge, the first step is to determine idealized shape of the bulge.

One of such attempts was the consideration of the quadratic parabolic form of such bulge [3]. The use of the shape of an arc of a circle is also quite widespread [4]. For bulges, in which the height is much smaller than the length, these two idealized shapes give the same numerical results. In a numerical experiment using the method of discrete dislocation dynamics, it was found that the best approximation for the shape

of the average bulge of the dislocation line will be a sinusoidal shape, in which the wave height is also much smaller than its length [5].

Modelling of solid solution strengthening and yield strength of multicomponent alloys, which is important for the development of new alloys, was considered in many works [3, 6–22]. In particular, the effect of the dislocation line shape in solid solution on the yield point was studied in [3, 6–19]. Such modelling allows predicting the likely yield strengths of such materials and can help in the development of new promising alloys of this class [3, 6–28]. Many works were devoted to the theoretical description of solid solution strengthening and the corresponding formation of the temperature dependence of the yield strength [3, 6–31]. In work [3], the critical stress necessary for the start of dislocation motion in the stochastic shear-stress field in the glide plane, essentially the yield point, is considered. The amplitude of the shear stresses, the average linear size of the region, where the stochastic stresses have the same sign, and the length of the dislocation segment, where the elementary-gliding process occurs, *i.e.*, the length of the average bulge on the dislocation line, are important in this case. The paper [6] considered the interaction of a moving dislocation with obstacles in the glide plane, which are created by solute atoms located in the immediate vicinity of this plane. There are two types of dislocation interaction with obstacles in the glide plane. The first type is when these obstacles can be considered as points. It is true for very dilute solid solutions, in which there are few solute atoms, which are located at a large distance from each other [32]. The second type is when the obstacles have a finite range of interaction with the dislocation, *i.e.* a certain size in the direction of dislocation motion, and the statistics of the interaction of the dislocation with such obstacles are different from the first case [3].

A new theory to calculate the yield strength of disordered solid solutions with an arbitrary number of components and an arbitrary composition, based on the Labusch model, was proposed in [7–15]. In these works, the waviness and roughness of the dislocation line were modelled in a simplified form by the identical trapezoidal protrusions in two opposite directions lying in the glide plane. The height and length of the protrusions were determined by first-principles calculations using density functional method. This theory uses the calculated first-principles interaction energies of solute atoms with dislocations as inputs to determine the yield strength and activation volume as functions of composition, temperature, and strain rate. Reducing waviness to uniform trapezoidal ridges requires neglecting the actual shape of the dislocation line, which is actually a sum of bulges of different heights, lengths, and shapes. Besides, one-dimensional sinusoidal dependence of internal stresses on the coordinate along the direction of dislocation motion was only considered in this theory. Neglecting the

real two-dimensional stochastic distribution of shear stresses in the glide plane can lead to significant errors in determining the shape of the dislocation line and the yield strength of the material.

The dislocation line shape was modelled using discrete dislocation dynamics [17]. Such modelling gives a more realistic shape, but it depends on the method of determining the stochastic shear-stress field in the glide plane. To model the distribution of shear stresses, a special method was developed in [17]. The force acting from the shear-stress field on a certain dislocation segment was calculated as a superposition of forces from randomly located pinning points in the glide plane, each of which created a Gaussian pinning potential. At the same time, the force acting on the dislocation from a certain pinning point dropped to almost zero when moving away from this point. Thus, pinning points located far from the dislocation segment practically did not act on it. This way of determining the forces acting on the dislocation and actually determining the shear-stress field provides a normal distribution of probabilities for these stresses, since the stress at a certain point is the sum of many random small contributions from different pinning points. However, this method has its drawbacks. First, the variance of the normal distribution is poorly specified by this method, as it depends on the number of pinning points that fall into the zone of influence around a certain point on the dislocation line. It should also be noted that the pinning points, which contribute to the force acting on a certain point on the dislocation line, are located only in the glide plane in the method proposed in [17]. However, in a real alloy, many crystal lattice distortion centres, which will contribute to the stochastic shear-stress field in the glide plane, are located in the space above and below the glide plane.

It should be noted that namely with such a more realistic approach, the distribution of shear stresses in the glide plane is divided into short-wavelength and long-wavelength components. Second, the identical pinning points are more consistent with modelling a binary alloy in which the identical solute atoms are dissolved in the solvent matrix. This method is somewhat questionable for multicomponent alloys. Thirdly, this method requires significant computing power and time spent on calculations. Thus, the development of another method of determining stochastic shear stresses in the glide plane may be useful. In addition, an insufficiently accurate method for determining the characteristic parameters of the dislocation line shape was proposed in [17], and the statistics of the various components of this shape were not studied.

Since the dislocation line shape was modelled only at zero applied stress in Ref. [17], the question arises about the evolution of this shape under the action of an external load. It was also noted that, in order to determine directly the yield strength using such modelling, it is neces-

sary to find such a critical applied stress at which the dislocation line shape ceases to be in equilibrium. In this case, the velocities of all segments of the dislocation will not go to zero sometime after the application of this external stress. Therefore, the dislocation will not stop and not reach an equilibrium shape. Such determination of yield strength requires successively increasing the applied stress from zero with a certain small step and checking the equilibrium shape of the dislocation line at each such step. The segments of the dislocation start to move with each subsequent increased stress, because their equilibrium is disturbed. Further, two cases are possible. First, the dislocation segments may stop after some time. This will mean that new equilibrium shape has been reached. Second, the movement of the segments will not stop and the dislocation will break away from the points of initial pinning. This can be conventionally considered as the plastic deformation beginning.

Various aspects of thermal activation analysis of the temperature dependence of the yield strength in binary and multicomponent solid solutions, in particular in high-entropy alloys, were considered in [25-28]. One of the considered problems is the existence of a 'plateau' on the temperature dependence of the critical shear stress at high temperatures, an almost constant value of the yield strength in a certain temperature range. The paper [25] shows that the existence of such a 'plateau' is essentially anomalous. The elastic modulus of the material decreases as the temperature increases, which in turn should lead to a decrease in the stochastic shear stresses in the dislocation glide plane, which are created by numerous local distortions of the crystal lattice, and, accordingly, to a decrease in the yield strength, rather than its constant value at elevated temperatures. Since the 'plateau' is observed experimentally, there must be additional factors that compensate for the decrease in the elastic modulus with increasing temperature. In particular, the drop in the shear modulus must be compensated by an increase in the distortion of the crystal lattice as the temperature increases for the 'plateau' existence. In the temperature region, where a 'plateau' is observed, in multicomponent solid solutions, in addition to an increase in the root mean square displacements of atoms, there may also be an effect of dynamic deformation ageing accompanied by the corresponding strengthening, which compensates for the elastic modulus decrease [25]. However, this effect is not universal and cannot explain the 'plateau' in all cases. Thus, the factors that compensate for the elastic modulus decrease due to the increase in temperature and contribute to the emergence of a 'plateau' require further research. The study of the dependence of the crystal lattice distortion on temperature is relevant in this sense.

Some issues of determining lattice distortion and yield strength in multicomponent alloys were discussed in Refs. [20–22]. Modelling of

dislocation motion by the method of discrete dislocation dynamics and calculation of the stochastic shear-stress field in the glide plane by direct summation of contributions from individual solute atoms located at the sites of crystal lattice in the space around this plane are considered in Refs. [5, 23, 24, 33]. The shear stress acting on the edge dislocation in the glide plane from a single solute atom can be calculated using the energy of interaction of such an atom and a trial rectilinear segment of the dislocation [24]. It should be noted that each atom in the substitutional solid solution could be considered as a point defect in the effective averaged matrix-solvent media [11, 12, 20–22]. The zone of influence of such a defect on the dislocation in the glide plane is greater the farther this defect is from the plane, but the interaction force decreases in this case [34]. Thus, the stochastic shear-stress field, which is created by solute atoms in the glide plane in a multicomponent alloy, can be divided into two components. The short-wavelength component with a larger amplitude and shorter correlation length of the stress field is created by solute atoms located in the immediate vicinity of the glide plane. For example, in Ref. [4], it is proposed to take into account affecting of only these atoms to the dislocation motion. The long-wavelength component with a much smaller amplitude and longer correlation length is created by atoms, which are farther from the glide plane. Typically, this component is neglected, but it can be quite significant. It can be supposed that the short-wavelength component of the shear-stress field is related to the thermal component of solid solution strengthening of multicomponent alloy. The long-wavelength component can be tried to be related to the athermal component of this strengthening, because its significantly longer correlation length can prevent thermally activated overcoming of energy barriers, which associated with it [34].

The characteristics of the shear-stresses' distribution in the glide plane in a solid solution can be calculated both by direct summation of contributions from many solute atoms [24, 33] and by using a special statistical method [35]. The main parameters of this distribution are the standard deviation and the correlation length of the short-wavelength component of the stochastic shear-stress field in the glide plane and the standard deviation and the correlation length of its long-wavelength component. The shear-stresses' distribution is the main factor in modelling dislocation motion in the glide plane by the method of discrete dislocation dynamics [5, 23]. In particular, such simulation shows the reality of the sequential action of the short- and long-wavelength components of the shear-stress field on the dislocation motion. This also clarifies the sinusoidal shape of the bulges on the dislocation line. These bulges are formed and disappear under the action of an external load, and the dislocation moves ahead by such a way.

The equilibrium shape of the dislocation at zero load fits well into a

band with a width of three full correlation lengths of the short-wavelength component of the shear-stress field [5]. The waviness of the dislocation line on the scale of the correlation length of the long-wavelength component does not appear without an external load. The external stress applied in the glide plane, which assists the dislocation segments to overcome the internal force barriers, can, to some extent, compensate for the short-wavelength component of the shear-stress field. Then, the waviness of the dislocation line will be activated on the scale that is associated with the long-wavelength component as the numerical experiment shows. Thus, the two components of the shear-stress field affect the dislocation line shape separately and sequentially when the external load increases. It is relevant to study how the two components of the shear-stress field affect the temperature dependence of the yield strength of a multicomponent alloy.

The goal of this work is to consider the statistical method of determining the characteristics of the stochastic shear-stress field in the glide plane in a multicomponent alloy and the influence of these characteristics on the temperature dependence of the yield strength in such an alloy, taking into account the short- and long-wavelength components of this field.

2. CALCULATION ALGORITHMS

2.1. Determination of Characteristics of Stochastic Shear-Stresses' Field in Glide Plane in Multicomponent Alloy

Shear stress τ_s that acts to trial rectilinear segment of the dislocation with the coordinates of centre x_u and z_u in the glide plane from solute atoms, which are located at the sites of crystal lattice with coordinates x_{hkm}, y_{hkm}, z_{hkm} in the space around this plane in multicomponent alloy, and gradient of this stress g_x along the x axis can be calculated as sums of contributions from these atoms [24, 33, 35]:

$$\tau_s = \sum_h \left(\sum_k \left(\sum_m \left(\frac{Gp'_{hkm} V_a}{b\Delta z} \tilde{\Delta} + \frac{Gq'_{hkm} V_a}{b\Delta z} \tilde{H} \right) \right) \right), \tag{1a}$$

$$g_x = \frac{\partial \tau_s}{\partial x} = \sum_h \left(\sum_k \left(\sum_m \left(\frac{Gp''_{hkm} V_a}{b\Delta z} \tilde{\Delta} + \frac{Gq''_{hkm} V_a}{b\Delta z} \tilde{H} \right) \right) \right). \tag{1b}$$

where G is the shear modulus of the alloy, b is the absolute value of Burgers vector of the alloy, V_a is the volume per atom for the alloy ($V_a = b^3(2)^{-1/2}$ for the alloy with f.c.c. lattice, $V_a = 4b^3/(3(3)^{1/2})$ for the alloy with b.c.c. lattice), Δz is the length of trial rectilinear segment of the edge dislocation, h, k and m are the indices, which specify the coor-

dinates of the sites where the solute atoms are located, along the axes x (in the glide plane in the direction of dislocation motion), y (perpendicular to the glide plane) and z (in the glide plane along the dislocation line) [24], h is the number of the plane perpendicular to the Burgers vector, in which the site is located, k is the number of the atomic row in the plane in which the site is located, m is the site number in the atomic row, $\tilde{\Delta}$ and $\tilde{H}$ are the discrete random variables that determine the atomic size misfit and elastic modulus misfit of a solute atom at a crystal lattice site in comparison with the 'average' atoms of a virtual matrix-solvent, respectively, and since an atom of any component can be located in a given site with a certain probability, then these variables take on their individual values for each site, p'_{hkm}, q'_{hkm}, p''_{hkm}, and q''_{hkm} are the variables that are related to the first and second derivatives of both pressure and energy density of elastic deformations by the x coordinate, respectively. The pressure and energy density are created by a trial segment of the edge dislocation at the point, where the solute atom is located.

If we sum in (1) only the contributions of the solute atoms in the two atomic planes nearest to the glide plane on each side, then this will be the so-called short-wavelength component τ_{s1} of the shear-stress field and its gradient g_{x1} [35]. The long-wavelength component of the shear-stress field τ_{s2} and its gradient g_{x2} are easily calculated from the equations [35]:

$$\tau_{s2} = \tau_s - \tau_{s1} \text{ and } g_{x2} = g_x - g_{x1}. \qquad (2)$$

The region of the dislocation core, where the elastic behaviour of the material is disturbed, should also be taken into account. This means that contributions of solute atoms located in the region of the dislocation core

$$\sqrt{(x_{hkm} - x_u)^2 + y_{hkm}^2} \le r_c, \left|z_{hkm} - z_u\right| \le \Delta z / 2,$$

where r_c is the radius of the dislocation core ($r_c \approx b$ for f.c.c. lattice), to the shear stress in the glide plane and to its gradient can be neglected, *i.e.*, equate to zero the corresponding terms in Eqs. (1). Contributions of solute atoms, which are far enough from the point of shear-stress determination at a distance greater than a certain critical distance, become very small and can be neglected too. Thus, the summation should be carried out, taking into account only the sites located at a distance that is less than the critical distance.

Variables $\tilde{\Delta}$ and $\tilde{H}$ can take the values of δ_i and η'_i with the probability X_i, respectively, where $\delta_I = (1/s_{lat})(ds_{lat}/dX_i)$ is the atomic size misfit of the component i in comparison with the atoms of the virtual effective averaged matrix-solvent (a conventional material consisting

of 'average' atoms of a solid solution [11]), s_{lat} is the average distance between the nearest atoms in the alloy ($s_{\text{lat}} = b$), $\eta'_i = \eta_i / (1 + 0.5|\eta_i|)$, $\eta_i = (1/G)(dG/dX_i)$ is the elastic modulus misfit of the component i in comparison with the atoms of the matrix-solvent [24, 33], X_i is the atomic fraction of the component i (note that the sum of the atomic fractions of all components is equal to one, that is, the sum of the probabilities of all possible options will, as it should, also be equal to one). Mathematical expectations of discrete random variables $\tilde{\Delta}$ and $\tilde{H}$ will be equal to zero due to the balance of positive and negative misfits:

$$E(\tilde{\Delta}) = \sum_{i=1}^{N} \delta_i X_i = 0 \text{ and } E(\tilde{H}) = \sum_{i=1}^{N} \eta'_i X_i = 0 .$$

In this case the variances of the variables $\tilde{\Delta}$ and $\tilde{H}$ are

$$D(\tilde{\Delta}) = \sum_{i=1}^{N} \delta_i^2 X_i \text{ and } D(\tilde{H}) = \sum_{i=1}^{N} (\eta'_i)^2 X_i ,$$

respectively.

Taking into account the details of the calculation of shear stresses given in Ref. [24], the variables p'_{hkm}, q'_{hkm}, p''_{hkm}, and q''_{hkm} can be determined through the numerically calculated first and second derivatives of both the pressure and the energy density of elastic deformations by the x coordinate, respectively [35]:

$$p'_{hkm} = 3\frac{p^{(1)}_{hkm} - p^{(2)}_{hkm}}{G\Delta x}, \tag{3a}$$

$$q'_{hkm} = \frac{q^{(1)}_{hkm} - q^{(2)}_{hkm}}{G\Delta x}, \tag{3b}$$

$$p''_{hkm} = \frac{6p^{(1)}_{hkm} - 3(p^{(2)}_{hkm} + p^{(3)}_{hkm})}{G\Delta x^2}, \tag{3c}$$

$$q''_{hkm} = \frac{2q^{(1)}_{hkm} - q^{(2)}_{hkm} - q^{(3)}_{hkm}}{G\Delta x^2}, \tag{3d}$$

where Δx is the small step along the x coordinate in the direction that is perpendicular to the trial segment of the edge dislocation (it is appropriate to accept $\Delta x = b/100$ [24, 33]);

$$p^{(j)}_{hkm} = -\frac{\sigma_{xx} + \sigma_{yy} + \sigma_{zz}}{3} \tag{4a}$$

is the pressure that is created by a trial segment of the edge dislocation with the coordinates of centre z_u and x_u ($j = 1$), $x_u + \Delta x$ ($j = 2$), $x_u - \Delta x$ ($j = 3$) at the point with the coordinates x_{hkm}, y_{hkm}, z_{hkm} [35];

$$q_{hkm}^{(j)} = \frac{(p_{hkm}^{(j)})^2}{2K} + \frac{\sigma_{xy}^2 + \sigma_{xz}^2 + \sigma_{yz}^2}{2G} \quad (4b)$$

is the energy density of elastic deformations in this point, σ_{xx}, σ_{yy}, σ_{zz}, σ_{xy}, σ_{xz}, σ_{yz} are the stress tensor components for the stress created by a trial segment of the edge dislocation at the point where the solute atom is located (details of the calculation of stress tensor components are given in Ref. [24]), K is the bulk modulus of the alloy.

The shear stress at a local point of the glide plane and gradient of this stress in the multicomponent alloy will be normally distributed random variables because, in accordance with (1), they will be the sums of a large number of random variables. Each of the variables is determined for its own site and multiplied by the corresponding constant. This was confirmed in shear-stress calculation by direct summation of contributions from individual solute atoms [24]. The mathematical expectations and variances of such normally distributed variables will be equal to the sums of the mathematical expectations and variances of summed random variables, which are multiplied by certain coefficients, respectively. Mathematical expectations of shear stress and gradient of this stress will be equal to zero due to the fact that $E(\tilde{\Delta}) = 0$ and $E(\tilde{H}) = 0$, that is, all components of mathematical expectations and their sum are equal to zero. This corresponds to the condition of zero balance of shear stresses in the glide plane and is confirmed by direct summation of contributions [24].

Taking into account the definition of the variances of discrete random variables $\tilde{\Delta}$ and $\tilde{H}$, the variance of the shear stress and gradient of this stress are, respectively [35]:

$$D(\tau_s) = s^2 = \sum_h \left(\sum_k \left(\sum_m \left[\left(\frac{Gp'_{hkm} V_a}{b\Delta z} \right)^2 D(\tilde{\Delta}) + \left(\frac{Gq'_{hkm} V_a}{b\Delta z} \right)^2 D(\tilde{H}) \right] \right) \right), \quad (5a)$$

$$D(g_x) = s_g^2 = \sum_h \left(\sum_k \left(\sum_m \left[\left(\frac{Gp''_{hkm} V_a}{b\Delta z} \right)^2 D(\tilde{\Delta}) + \left(\frac{Gq''_{hkm} V_a}{b\Delta z} \right)^2 D(\tilde{H}) \right] \right) \right), \quad (5b)$$

where s and s_g are the standard deviations of the shear stress and gradient of this stress, respectively. These deviations, as well as, by analogy, the corresponding deviations for the short- and long-wavelength components and corresponding gradients, s_1, s_{g1}, s_2, s_{g2}, can be expressed from (5) after some transformations taking into account the definition of $D(\tilde{\Delta})$ and $D(\tilde{H})$ as follows [35]:

$$s = \frac{GV_a}{b\Delta z} (Q')^{1/2} \left(\sum_{i=1}^{N} (\eta_i'^2 + \alpha_s^2 \delta_i^2) X_i \right)^{1/2}, \quad (6a)$$

$$s_g = \frac{GV_a}{b\Delta z}(Q'')^{1/2}\left(\sum_{i=1}^{N}(\eta_i'^2 + \alpha_g^2\delta_i^2)X_i\right)^{1/2}, \tag{6b}$$

$$s_1 = \frac{GV_a}{b\Delta z}(Q_1')^{1/2}\left(\sum_{i=1}^{N}(\eta_i'^2 + \alpha_{s1}^2\delta_i^2)X_i\right)^{1/2}, \tag{6c}$$

$$s_{g1} = \frac{GV_a}{b\Delta z}(Q_1'')^{1/2}\left(\sum_{i=1}^{N}(\eta_i'^2 + \alpha_{g1}^2\delta_i^2)X_i\right)^{1/2}, \tag{6d}$$

$$s_2 = \frac{GV_a}{b\Delta z}(Q_2')^{1/2}\left(\sum_{i=1}^{N}(\eta_i'^2 + \alpha_{s2}^2\delta_i^2)X_i\right)^{1/2}, \tag{6e}$$

$$s_{g2} = \frac{GV_a}{b\Delta z}(Q_2'')^{1/2}\left(\sum_{i=1}^{N}(\eta_i'^2 + \alpha_{g2}^2\delta_i^2)X_i\right)^{1/2}, \tag{6f}$$

where

$$\alpha_s = (P'/Q')^{1/2} \text{ and } \alpha_g = (P''/Q'')^{1/2}, \tag{7a}$$

$$\alpha_{s1} = (P_1'/Q_1')^{1/2} \text{ and } \alpha_{g1} = (P_1''/Q_1'')^{1/2}, \tag{7b}$$

$$\alpha_{s2} = (P_2'/Q_2')^{1/2} \text{ and } \alpha_{g2} = (P_2''/Q_2'')^{1/2}, \tag{7c}$$

$$P' = \sum_h\left(\sum_k\left(\sum_m (p'_{hkm})^2\right)\right) \text{ and } P'' = \sum_h\left(\sum_k\left(\sum_m (p''_{hkm})^2\right)\right), \tag{8}$$

and

$$Q' = \sum_h\left(\sum_k\left(\sum_m (q'_{hkm})^2\right)\right) \text{ and } Q'' = \sum_h\left(\sum_k\left(\sum_m (q''_{hkm})^2\right)\right). \tag{9}$$

Parameters P_1', P_1'', Q_1', Q_1'' for short-wavelength component can be obtained, if we sum up the contributions only from solute atoms in the two atomic planes nearest to the glide plane on each side. The parameters for the long-wavelength component are calculated as $P_2' = P' - P_1'$, $Q_2' = Q' - Q_1'$, $P_2'' = P'' - P_1''$, and $Q_2'' = Q'' - Q_1''$.

It is also important to determine the correlation lengths w_1 and w_2 of the short- and long-wavelength components of the stochastic shear-stress field in the glide plane, *i.e.* the average linear dimensions of regions where the short-wavelength component has the same sign and regions where the long-wavelength component has the same sign. The distribution of positive shear stresses along the axis inside such a region will be considered, regardless of the component, to do this. Schematically, three individual realizations of such shear-stresses' distribution as random variable are shown in Fig. 1. The points that are located exactly in the middle between the endpoints of the distributions are combined together. This centre point is chosen as the coordinate

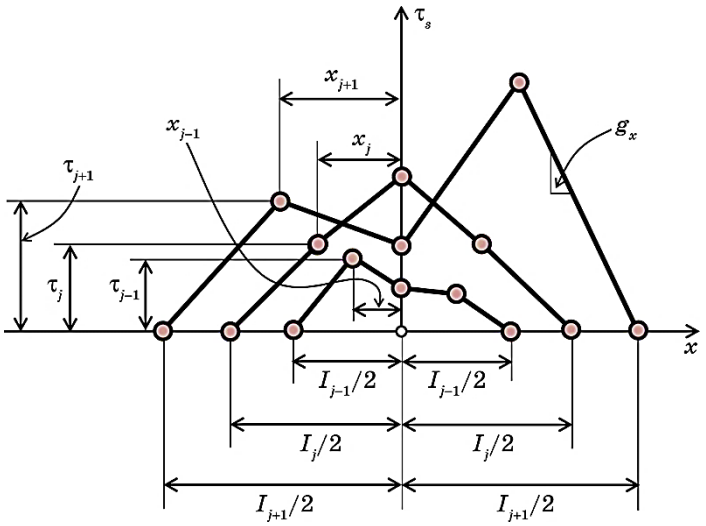

Fig. 1. Schematic presentation of three individual realizations of the distribution of positive shear stresses as random variables [35]. Grey circles show the corresponding random values.

origin. First, for these realizations, as well as all similar ones, the shear stress is always zero at the endpoints. Secondly, the size of the regions and the maximum stress in the regions may be different for different realizations. Thirdly, different realizations can have several local maxima and be completely asymmetric. However, it is possible to determine the average stress distribution for such regions. The size of the region of such an average distribution will be equal to, by definition, the average linear size of the region where the stresses are positive, *i.e.* the correlation length $w = <l_j>$, where l_j is the size of the region of the j-th realization.

If shear stress, as random variable, have a normal distribution with zero mathematical expectation and standard deviation s, then a set of only positive values from such distribution has an average value, which will be the average stress value of $m_s = <\tau_j> = s(2/\pi)^{1/2}$ for our average distribution. If the special coordinates $(x_j/l_j)w$ for each realization will be defined, then, the points of all realizations can be displayed in single average region with the size w. Further, it is possible to average the stress over all realizations for each special coordinate $(x_j/l_j)w$ and obtain the average distribution of positive stresses in the region with the size w (Fig. 2). The stresses of the average distribution will be equal to zero at the end points of the region. Further, the stress should increase from each end point towards the centre of the region, since the average stress value of the average distribution is greater than zero. This increase will be symmetrical relative to the centre point of the region be-

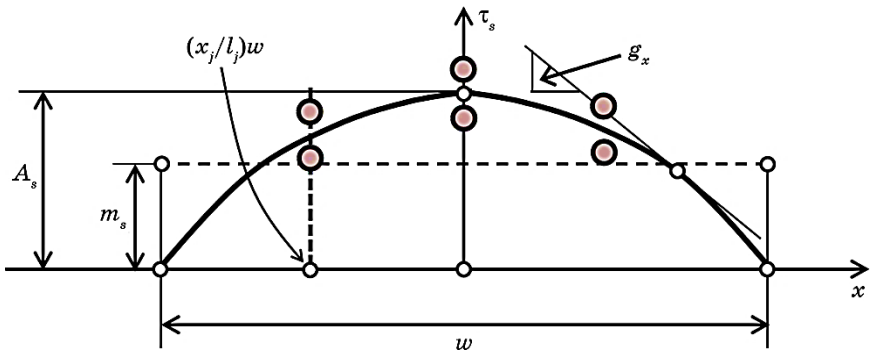

Fig. 2. Schematic presentation of the averaged distribution of positive shear stresses as random variables [35]. Grey circles show the corresponding random values.

cause the portions of the region on both sides of the centre point are absolutely equal and have no advantages over each other due to the homogeneity of the statistical distribution of stresses on the glide plane. Thus, the average distribution will be a smooth curve symmetrical relative to the centre point with the maximum at this point. Note that the average value of the stress gradient for the average distribution will be zero, because the stress must rise from zero at one end point and fall to zero at the other. The change in the gradient along the average distribution region is shown in Fig. 3. If only the positive values of the gradient will be averaged, then, similarly to the stress, we will have an average value of $m_g = s_g(2/\pi)^{1/2}$. The average distribution can be approximated by a suitable function, for example $\tau_s = A_s\cos(\pi x/w)$ or $\tau_s = A_s(1 - |2x/w|^n)$, where n is the exponent ($n > 1$). Then maximum values of average distribution will be $A_s = \pi m_s/2$ and $A_s = (n+1)m_s/n$ for these approximation functions, respectively (Fig. 2). If the stress gradient for both functions is averaged over the portion where it is positive, a single result for average gradient of $m_g = 2A_s/2$ is obtained (Fig. 3). Further, it is easy to derive expressions for w and, by analogy, for w_1 and w_2 for both approximation functions [35]:

$$w = \pi s / s_g,\ w = 2(n+1)s / (ns_g)\,, \tag{10a}$$

$$w_1 = \pi s_1 / s_{g1},\ w_1 = 2(n+1)s_1 / (ns_{g1})\,, \tag{10b}$$

$$w_2 = \pi s_2 / s_{g2},\ w_2 = 2(n+1)s_2 / (ns_{g2})\,. \tag{10c}$$

Note that, for $n = 2$, both functions result in very close results. Besides, the parameters s_1, s_{g1}, s_2 and s_{g2} depend on Δz. Besides, it was found that we should use $\Delta z = 2w_2$ [5, 36]. If Eqs. (10) are taken into account, it is possible to obtain, in particular, the equation

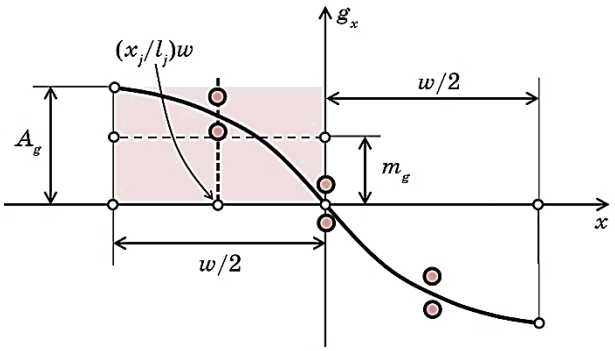

Fig. 3. Schematic presentation of the gradient of the averaged distribution of positive shear stresses as random variables [35]. Grey circles show the corresponding random values.

$w_2 = \pi s_2(2w_2)/s_{g2}(2w_2)$ allowing to determine the values of Δz and w_2.

The main parameters of the stress field may also depend on the coordinates x_u and z_u. At the same time, it should be taken into account that, for convenience, the origin of coordinates can be chosen so that it lies in the glide plane and the nearest crystal lattice site is directly above it (in the positive direction of the y axis). Due to the periodicity of crystal lattice, the results will be repeated with the period b (distance between lattice sites in the direction of dislocation motion) for x_u and with periods $b(3)^{1/2}$ or $2b(2)^{1/2}$ (distance between sites along the dislocation line for f.c.c. and b.c.c. lattices, respectively) for z_u. Therefore, it is enough to average the main parameters of the shear-stress field in the local region of the glide plane, where $0 \le x_u \le b$ and $0 \le z_u \le b(3)^{1/2}$ or $0 \le z_u \le 2b(2)^{1/2}$, to obtain an averaged result for the entire plane. In this way, four main parameters of the stochastic shear-stress field in the glide plane can be calculated, namely the standard deviation S_1 and the correlation length w_1 of the short-wavelength component and the standard deviation S_2 and the correlation length w_2 of long-wavelength component of the stress field [35].

2.2. Temperature Dependence of Yield Strength of Multicomponent Alloy

If the virtual matrix-solvent is taken into account, the yield strength of a multicomponent alloy with the contribution of only solid solution strengthening can be expressed as follows [22, 36]:

$$\sigma_y = \overline{\sigma}^* + \overline{\sigma}_\mu + \Delta\sigma^* + \Delta\sigma_\mu = M\tau_y = M(\tau_P + \tau^* + \tau_\mu), \qquad (11)$$

where $\overline{\sigma}^*$ and $\overline{\sigma}_\mu$ are the thermal and athermal components of yield

strength of virtual matrix-solvent in the terms of normal stress, $\Delta\sigma^*$ and $\Delta\sigma_\mu$ is the thermal and athermal components of solid solution strengthening in the terms of normal stress, M is the Taylor factor ($M = 3.06$ for the material with f.c.c. lattice), τ_y is the critical resolved shear stress (yield strength in the terms of shear stress), $\tau_P = \overline{\sigma}^* / M$ is the Peierls–Nabarro stress of virtual matrix-solvent (also known as the lattice friction stress, which is typically equal to a few of megapascals for a material with f.c.c. lattice), $\tau^* = \Delta\sigma^*/M$ is the thermal component of the critical resolved shear stress associated with solid solution strengthening, $\tau_\mu = \Delta\sigma_\mu/M$ is the athermal component of the critical resolved shear stress associated with solid solution strengthening.

Since the virtual matrix-solvent without solid solution strengthening is in a certain way an ideal material and effect of grain boundaries presence is not considered, it essentially lacks sources of long-range internal stresses. Therefore, it can be assumed that $\overline{\sigma}_\mu = 0$.

There are three main factors that affect the dislocation motion: the periodic potential of the crystal lattice, which is responsible for the Peierls–Nabarro stress, the short-wavelength and long-wavelength components of the stochastic shear-stress field in the glide plane, which are created by solute atoms in a multicomponent alloy, if the alloy is in the form of a single-phase concentrated solid solution and only solid solution strengthening is considered [33]. The lattice potential creates a periodic distribution of stresses in the direction of dislocation motion, and as a result resistance to this movement. For example, the amplitude of such a distribution for a material with f.c.c. lattice is quite small. The distance in the direction of dislocation motion, at which these stresses are balanced, is approximately equal to the absolute value of the Burgers vector b. The short-wavelength component of the shear-stress field in the glide plane as a normally distributed random variable has a mathematical expectation that is equal to zero and a standard deviation $s_1(\Delta z)$ that depends on the length of the trial segment of the dislocation Δz used in the calculation of the stress distribution. The average linear size of the region where the stochastic stresses have the same sign for this component will be w_1. Then the full correlation length, the average linear size of the region where the stresses balance themselves, is $2w_1$ [33]. The long-wavelength component also has zero mathematical expectation and standard deviation $s_2(\Delta z)$ with full correlation length $2w_2$. The parameter Δz can be estimated from the condition that the correlation length of the long-wavelength component of the shear-stress field along the dislocation line should be equal to the one along the direction of the dislocation motion, *i.e.* $2w_2$. Therefore, it is possible to accept $\Delta z = 2w_2$ in calculations [5].

Each of the described factors can create force barriers for dislocation motion. The width of these barriers will be comparable with the Burgers vector for the periodic lattice potential and with w_1 and w_2 for

the short-wavelength and long-wavelength components of the shear-stress field, respectively. That is, the narrowest force barrier is created by the periodic lattice potential, and the widest force barrier is formed by the long-wave component of the shear-stress field. The stresses from the periodic lattice potential are balanced at a distance smaller than the average linear size of the region where the stochastic stresses have the same sign for the short-wavelength component. The stress of the short-wavelength component, in turn, is balanced at a distance smaller than the average linear size of the region where the long-wavelength component has the same sign. Such conclusions can be drawn from the results of calculations w_1 and w_2 for some alloys [33]. That is, all these force barriers act independently of each other, each on its own size scale. For example, it is shown that initially only short-wavelength component of the shear-stress field acts on the dislocation motion. Then, after overcoming the barriers from this component with the external stress assistance, the long-wavelength component of this field starts to affect this movement [5].

The height of these force barriers will be in a completely different ratio compared to their width. The force barrier due to the short-wavelength component will be the highest, while the barriers due to the other two factors will be significantly lower. Thus, barriers due to the short-wavelength component will dominate. Overcoming such a barrier by a dislocation with the assistance of externally applied stress and thermal activation will be a critical event to start the dislocation motion. The stress required to overcome the barrier from the short-wavelength component will determine the term τ^* in (11). Barriers due to the periodic lattice potential, which are much lower compared to the barriers due to the short-wavelength component, will be suppressed by the latter, since both types of barriers are superimposed on each other. Therefore, the barriers due to the periodic lattice potential can be taken into account by simply adding a constant stress τ_P to the stress that is necessary to overcome the barrier from the short-wavelength component. The barrier due to the long-wavelength component is significantly wider in the spatial dimension, lower in the force dimension and higher in the energy sense than the barrier from the short-wavelength component. Therefore, such a barrier, which is also superimposed on the barriers due to the short-wavelength component, can be overcome only athermally, without thermal activation. As in the case of barriers due to periodic lattice potential, the barriers due to the long-wavelength component can be taken into account by adding the constant stress required for their athermal overcoming to the stress for overcoming the barriers due to the short-wavelength component. The stress required to overcome the barrier due to the long-wavelength component will determine the term τ_μ in Eq. (11).

A dislocation in stochastic shear-stress field under the action of an

external load will not move as a whole. Rather, it will advance step-by-step by forming appropriate bulges on individual segments of finite length. The critical dislocation segment with a bulge that is directed against the direction of dislocation motion is first straightened under the action of external stress, and then a new bulge is formed on it that is directed in the direction of dislocation motion. As a result, bulges are formed on the adjacent segments, which are directed against the direction of dislocation motion. The process of straightening and changing the direction of the bulges takes place on these segments as well. This, in turn, brings the critical segment to a state where the bulge on it again becomes directed against the direction of dislocation motion and the whole process is repeated. Schematically, this process for the critical segment in an idealized form is shown in Fig. 4. Initially, there is the bulge *1* with length L_1 and height $2w_1$ at zero applied stress. The averaged coordinate of $x = 0$ can be attributed to it. Further, under an external stress equal to τ_{y1}, the bulge *1* is straightened to state *2*. It can be assigned the averaged coordinate of $x = 4w_1/3$, if it is assumed that the average bulge has a parabolic shape for simplification. The bulge takes the state *3* with the averaged coordinate of $x = 8w_1/3$ in the next step. Further, the bulge successively turns into state *4* and state *5*, and the process is repeated.

In order to analyse overcoming a force barrier by a dislocation with the assistance of the thermal activation, it is necessary to set the profile of the effective stress from the shear-stress field that acts on the critical segment of the dislocation in the direction of its movement in the glide plane, that is, the dependence of this stress on the averaged forward displacement x of this segment. To simplify the problem, consider the acceptable sinusoidal dependence proposed in [4]:

$$\tau_1(x) = \tau_{y1} \sin(\pi x / 2\tilde{x}), \tag{12}$$

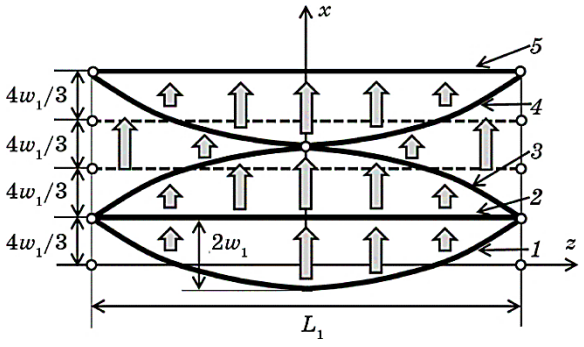

Fig. 4. The idealized process of the critical segment movement [36]. Grey arrows show the direction of movement of this segment.

where $\tilde{x} = 4w_1 / 3$ is the averaged forward displacement of the critical segment at which the maximum stress τ_{y1} is reached. The maximum stress is associated with the short-wavelength component of the shear-stress field in our case, because it dominates at the formation of a force barrier that the dislocation can overcome with the thermal activation assistance. This dependence is schematically shown in Fig. 5. The stress τ_{y1} required for the critical dislocation segment to overcome the short-wavelength component of the stochastic stress field without thermal activation will be equal to the stress acting on average from this component to this segment [3, 17]:

$$\tau_{y1} = s_1(2w_2)\sqrt{\frac{w_2}{w_1}}\sqrt{\frac{2w_1}{L_1}} = G\left(\frac{2}{\alpha\beta}\frac{w_1}{b}\right)^{1/3}\left(\frac{s_1(2w_2)}{G}\sqrt{\frac{w_2}{w_1}}\right)^{4/3} = \\ = A_1 G\left(\sum_{i=1}^{N}(\eta_i'^2 + \alpha_{s1}^2\delta_i^2)X_i\right)^{2/3}, \tag{13}$$

where

$$A_1 = \left(\frac{b^7 Q_1'^2}{32\alpha\beta w_1 w_2^2}\right)^{1/3} \tag{14}$$

for the alloy with f.c.c. lattice, and

$$A_1 = \left(\frac{b^7 Q_1'^2}{22.78\alpha\beta w_1 w_2^2}\right)^{1/3} \tag{15}$$

for the alloy with b.c.c. lattice. The average length L_1 of the critical

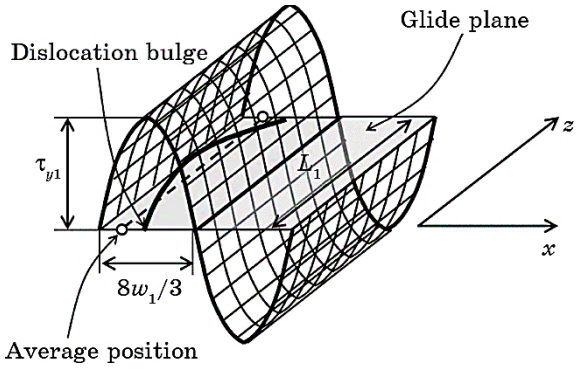

Fig. 5. Schematic presentation of the dependence of the stress acting on the critical segment in the glide plane on the averaged forward displacement of this segment x [36]. The average bulge on critical segment and its averaged position are also shown.

segment under acting short-wavelength component is [5, 36]:

$$L_1 = \left(\frac{\beta\Gamma}{s_1(2w_2)b\sqrt{w_2 / w_1}} \right)^{2/3} (2w_1)^{1/3}, \qquad (16)$$

where β is the coefficient depended on the shape of critical segment bulge ($\beta = 2\pi \approx 6.28$ for sinusoidal shape that confirmed by modelling [5]), Γ is the linear tension of the dislocation line ($\Gamma = \alpha G b^2$, where α is the coefficient less than 1/2).

It is more convenient to consider dependence (12) in terms of the force acting on the critical segment (Fig. 6). Then, the area under the curve will be measured in energy units. Point *1* at zero applied stress in Fig. 6 corresponds to state *1* in Fig. 4, point *2* corresponds to state *2* and so on, respectively. When an external stress τ is applied, the critical segment goes to the state with $x = x_s$. In order to overcome the force barrier from this position (pass through point *2*), it is necessary to provide the critical segment with additional energy ΔE, which is a function of τ. This energy can be obtained with the thermal activation assistance, which occurs due to thermal fluctuations. The probability of this event (a forward jump of the segment through the barrier) will depend on the energy ΔE and temperature T. At the same time, the critical segment will go to the state with $x = x_u$. This is a state of unstable equilibrium. In this case, the segment will quickly advance to the state with $x = x_2$ spontaneously. A backward jump from point with $x = x_2$ to

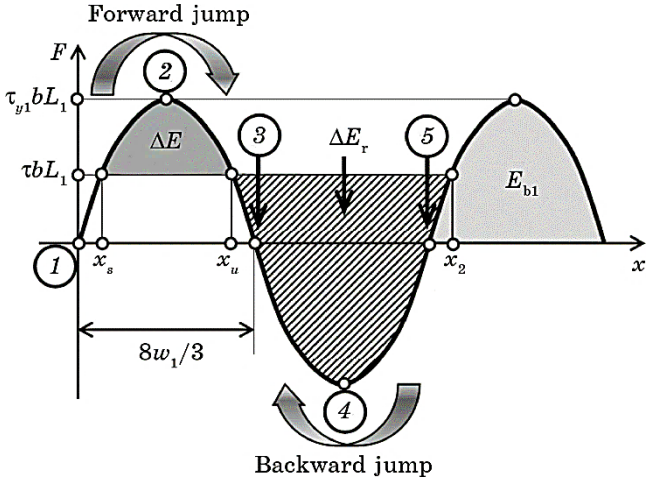

Fig. 6. Dependence of the force acting on the critical segment from the stochastic shear-stress field on the averaged forward displacement of this segment x [36]. Arrows show the directions of forward and reverse jumps through force barriers.

point with $x = x_u$ and further to point with $x = x_s$ is also possible. It is necessary to obtain energy ΔE_r through thermal activation for a backward jump. The probability of this jump will be determined by this energy and temperature T. Taking into account the probabilities of forward and backward jumps of critical segment, the strain rate can be expressed as [4]:

$$\dot{\varepsilon} = \dot{\varepsilon}_0 \left\{ \exp\left(-\frac{\Delta E}{k_B T} \right) - \exp\left(-\frac{\Delta E_r}{k_B T} \right) \right\}, \tag{17}$$

where $\dot{\varepsilon}_0$ is the pre-exponential factor, k_B is the Boltzmann constant. It should be noted that, for sinusoidal dependence (Fig. 6), we have [4]:

$$\Delta E = E_{b1}(1 - \tau / \tau_{y1})^{3/2}, \tag{18}$$

where the height of barrier from short-wavelength component in energy units [36]:

$$E_{b1} = \frac{16}{3\pi} b w_1 L_1 \tau_{y1} = \frac{25.398}{3\pi} (\beta\Gamma)^{1/3} b^{2/3} w_1^{4/3} w_2^{1/3} [s_1(2w_2)]^{2/3}. \tag{19}$$

Detailed analysis of area ratio in Fig. 6 results in

$$\Delta E_r = \Delta E + \pi E_{b1} \frac{\tau}{\tau_{y1}}. \tag{20}$$

Then from (17), (18) and (20) it can be derived the expression [36]:

$$\theta = (1 - \gamma)^{3/2} - (\theta / \lambda) \ln(1 - \exp(-\pi\lambda\gamma / \theta)), \tag{21}$$

where $\theta = T/T_0$, $\gamma = \tau/\tau_{y1}$, $\lambda = \ln(\dot{\varepsilon}_0 / \dot{\varepsilon})$ and

$$T_0 = \frac{E_{b1}}{k_B \ln(\dot{\varepsilon}_0 / \dot{\varepsilon})}. \tag{22}$$

Eq. (21) should be solved numerically to obtain the dependence $\gamma(\theta)$. If the appropriate values of $\dot{\varepsilon}_0 \approx 10^4$ s^{-1} and $\dot{\varepsilon}_0 \approx 10^{-3}$ s^{-1} are used [11], we have $\lambda = \ln(\dot{\varepsilon}_0 / \dot{\varepsilon}) \approx 16$. Then the equation (21) results in [36]:

$$\gamma = 1 - \theta^{2/3}, \; 0 \le \theta \le 0.9, \tag{23a}$$

$$\gamma = 4630 \exp(-12.35\theta), \; 0.9 < \theta. \tag{23b}$$

This result depends weakly on the values of $\dot{\varepsilon}_0$ and $\dot{\varepsilon}$, if the ratio $\dot{\varepsilon}_0 / \dot{\varepsilon}$ changes by an order of magnitude in one direction or another, since it is under the logarithm. The effect of backward jumps becomes noticeable only for $\theta > 0.9$, that is, at small applied stresses τ. At the

same time, the value γ quickly goes to zero. Practically we have $\gamma = 0$ at $\theta = 1.25$. Recall that in our analysis, τ is the applied stress, at which thermal activation assists overcoming the barriers from the short-wavelength component of the shear-stress field at a given strain rate and at a given temperature, essentially $\tau^* = \tau$.

The existence of the long-wavelength component of the shear-stress field, the calculation of which is shown in Ref. [33], was proved by modelling dislocation motion in Ref. [5]. The stress required for athermal overcoming of the force barrier from the long-wavelength component is [36]

$$\tau_{y2} = s_2(2w_2)\sqrt{\frac{2w_2}{L_2}} = G\left(\frac{2}{\alpha\beta}\frac{w_2}{b}\right)^{1/3}\left(\frac{s_2(2w_2)}{G}\right)^{4/3} = \\ = A_2 G\left(\sum_{i=1}^{N}(\eta_i'^2 + \alpha_{s2}^2\delta_i^2)X_i\right)^{2/3}, \tag{24}$$

where

$$A_2 = \left(\frac{b^7 Q_2'^2}{32\alpha\beta w_2^3}\right)^{1/3} \tag{25}$$

for the alloy with f.c.c. lattice, and

$$A_2 = \left(\frac{b^7 Q_2'^2}{22.78\alpha\beta w_2^3}\right)^{1/3} \tag{26}$$

for the alloy with b.c.c. lattice. The average length L_2 of the critical segment under acting long-wavelength component can be determined by analogy like L_1 [5]:

$$L_2 = \left(\frac{\beta\Gamma}{s_2(2w_2)b}\right)^{2/3}(2w_2)^{1/3}. \tag{27}$$

Now we can take $\tau_\mu = \tau_{y2}$. The height of barrier from long-wavelength component in energy units can be found by analogy as for short-wavelength component using Eq. (19), if necessary replacements will be made [36]:

$$E_{b2} = \frac{16}{3\pi} b w_2 L_2 \tau_{y2} = \frac{25.398}{3\pi}(\beta\Gamma)^{1/3} b^{2/3} w_2^{5/3}(s_2(2w_2))^{2/3}. \tag{28}$$

Eqs. (11) and (23) lead to the temperature dependence of the yield strength of a multicomponent alloy in the form of a single-phase concentrated solid solution, taking into account only solid solution strengthening and two components of the shear-stress field in the glide

plane, in the form [36]:

$$\sigma_y = M\{\tau_P + \tau_{y1}[1 - (T / T_0)^{2/3}] + \tau_{y2}\},\ 0 \le T \le 0.9T_0\,, \quad (29a)$$

$$\sigma_y = M\{\tau_P + 4630\tau_{y1}\exp(-12.35T / T_0) + \tau_{y2}\},\ T > 0.9T_0\,. \quad (29b)$$

However, the characteristic stresses τ_{y1} and τ_{y2} can depend on temperature due to the temperature dependence of the shear modulus G. The existence of a 'plateau' on the temperature dependence of the yield strength at high temperatures, when the yield strength remains constant in a certain temperature range, proves that the drop in the shear modulus with temperature is necessarily compensated for, in some way, for example, by an increase in the crystal lattice distortion as the temperature increases [25]. That is, the drop in the shear modulus should actually be compensated by an increase in $s_1(2w_2)$ and $s_2(2w_2)$, which depend on lattice distortion. This allows to assume that the products of the shear modulus and the factors associated with $s_1(2w_2)$ and $s_2(2w_2)$ in Eqs. (13) and (24) do not depend on temperature [36]. Thus, it is enough to calculate them at some temperature and consider them approximately the same for all other temperatures.

3. RESULTS AND DISCUSSION

3.1. Characteristics of Shear-Stress Field in Glide Plane in the CrCoNiFeMn Alloy

The method of determining the standard deviations and correlation lengths of the short- and long-wavelength components of the stochastic shear-stress field in the glide plane needs verification. To do this, it must be applied to a multicomponent alloy, the above-mentioned characteristics of which are known from other sources. Multicomponent CrCoNiFeMn alloy was chosen to verify the method. This alloy is a substitutional solid solution having an f.c.c. lattice. The parameters s_1, w_1, s_2 and w_2 for this alloy were determined in [33] by another method from the analysis of shear-stresses' distributions in the glide plane, which were calculated by the method of direct summation of contributions from solute atoms. The input parameters for calculation were taken as in [33]: shear modulus $G = 81$ GPa, bulk modulus $K = 176$ GPa, Poisson's ratio $\nu = 0.3$, Burgers vector $b = 0.25$ nm, atomic volume $V_a = 0.011$ nm^3. Atomic size misfits and elastic modulus misfits for component atoms are given in Table 1 [33]. The critical distance of approximately 4.75 nm was determined, at which the contribution to the shear stress from the solute atom should still be taken into account [24, 33]. Therefore, in the sums P_1', Q_1', P_1'', Q_1'', P_2', Q_2', P_2'', Q_2'' it is necessary to take into account only contributions from atoms that are at a dis-

TABLE 1. Atomic-sizes' misfits δ_i and elastic-moduli misfits η_i for component atoms used for the calculation of main parameters of shear-stress field in the CrCoNiFeMn alloy [35].

Component	i	X_i	δ_i	η_i
Cr	1	0.2	0.010077	0.290837
Co	2	0.2	0.001747	–0.13433
Ni	3	0.2	0.004622	–0.12114
Fe	4	0.2	0.004674	–0.04529
Mn	5	0.2	–0.02244	–0.05755

tance less than or equal to 4.75 nm from the point with coordinates x_u and z_u.

The dependences of the parameters s_1, w_1, s_2 and w_2 on the x_u coordinate in the range of $0 \le x_u \le b$ were determined by equations (6) and (10) at $\Delta z = 1.94$ nm for various characteristic values of the z_u coordinate from the range of $0 \le z_u \le b(3)^{1/2}$ for the CrCoNiFeMn alloy [33, 35, 36]. Dependences s_1 and w_1 are symmetrical with respect to $x_u = 0.125$ nm, because this is the distance between the atomic planes that are perpendicular to the Burgers vector in the f.c.c. lattices in our chosen alloy. The atoms are located along a straight line parallel to the Burgers vector with a step equal to the absolute value of this vector, *i.e.* 0.25 nm. The parameters $s_1 = 180$ MPa and $w_1 = 0.38$ nm averaged over x_u and z_u correlate well with the average values $s_1 = 191$ MPa and $w_1 = 0.38$ nm, which were determined in Ref. [33] from the analysis of shear-stresses' distributions in the glide plane. It should also be noted that the ranges of minimum–maximum values of 165–208 MPa for s_1 and of 0.21–0.54 nm for w_1 in the proposed method also correlate well with similar ranges of 166–234 MPa and 0.32–0.48 nm determined in [33]. Dependences s_2 and w_2 demonstrate the practical independence of these parameters on x_u and z_u [35]. This is due to the fact that s_2 and w_2 are determined by atoms farther from the glide plane and from the dislocation core. The averaged parameters of $s_2 = 71$ MPa and $w_2 = 1$ nm also correlate well with the average values of $s_2 = 72$ MPa and $w_2 = 0.97$ nm, which were determined in [33].

A certain combination of atomic size misfits and elastic modulus misfits is used to characterize the general lattice distortion in [37]:

$$\chi = \left(\sum_{i=1}^{N} (\eta_i'^2 + \alpha_0^2 \delta_i^2) X_i\right)^{2/3}, \tag{30}$$

where α_0 is the constant that equal to 16 for the edge dislocations [20, 24, 30, 37]. This parameter is called the average distortion of crystal lattice in [24]. Statistical method of the determination of the standard

deviations of the shear-stress field leads to similar combinations in (13) and (24), which can be called the effective lattice distortions for the short- and long-wavelength components, respectively [35]:

$$\chi_{s1} = (\sum_{i=1}^{N} (\eta_i'^2 + \alpha_{s1}^2 \delta_i^2) X_i)^{2/3} \text{ and } \chi_{s2} = (\sum_{i=1}^{N} (\eta_i'^2 + \alpha_{s2}^2 \delta_i^2) X_i)^{2/3}. \quad (31)$$

Equations (31) differ from (30) because instead of α_0 they contain α_{s1} and α_{s2}, which can be calculated by equations (7). These parameters averaged over the characteristic region $0 \le x_u \le b$ and $0 \le z_u \le b(3)^{1/2}$ are $\alpha_{s1} = 39$ and $\alpha_{s2} = 107$, and the corresponding parameters $\chi_{s1} = 0.36$ and $\chi_{s2} = 1.32$ for the CrCoNiFeMn alloy. Note that in this case $\chi = 0.14$. In essence, the constant α_0 is the ratio of the force of dislocation interaction with a solute atom, caused by atomic size misfit, to the force of interaction caused by elastic modulus misfit [32]. The farther the solute atom is located from the glide plane, the greater this ratio. This is explained by the fact that the force of interaction, caused by elastic modulus misfit, decreases with the distance from the glide plane faster than the force, caused by atomic size misfit. If only the solute atoms nearest to the glide plane are taken into account, then this ratio cannot be less than 16 for an edge dislocation. This determines that the constant $\alpha_0 = 16$ [20, 24, 30, 37]. The parameters α_{s1} and α_{s2} have the same sense as α_0. Their larger values are due to the fact that solute atoms farther from the glide plane than in the calculation of α_0 are taken into account. At the same time, α_{s2} is greater compared to α_{s1}, because atoms farther from the glide plane participate when forming the long-wavelength component of the stress field in comparison with forming the short-wavelength component. Thus, the method considered in this paper proposes the use of different effective lattice distortions to determine the main parameters of the short- and long-wavelength components of the shear-stress field.

Athermal component of solid solution strengthening was considered in [20, 35] as

$$\Delta\sigma_\mu = AG\chi, \quad (32)$$

where A is the empirical constant. Average value of 0.0026 ± 0.0005 was determined for this constant by experimental data treatment for many alloys with f.c.c. lattice. On other hand, we have $\Delta\sigma_\mu = M\tau_{y2}$ [36]. Eqs. (24), (31) and (32) result in

$$A = MA_2\chi_{s2} / \chi, \quad (33)$$

where A_2 is determined by Eq. (25) [35]. In our case, we have $A_2 = 0.000133$ for the CrCoNiFeMn alloy. Then, the constant can be calculated as $A = 0.0038$ according to Eq. (33). This is comparable with

the value given in Ref. [20]. It should be noted that the values of χ_{s2} and A_2 will also depend on the Poisson's ratio of the alloy due to the stress-tensor components at the solute atom location. The larger Poisson's ratio, the larger χ_{s2} and A_2. That is, each alloy may have its own individual value of A_2. The constant A was calculated for one specific alloy in this work, and it was determined by averaging data for many alloys, each of which had its own Poisson's ratio, in [20]. Under such circumstances, these two values of the constant A cannot completely match. They will necessarily be different from each other. Nevertheless, their comparability proves that the statistical method proposed here gives at least realistic results. It can also be concluded that the constant A for each alloy has its own individual value. There is no single constant A for all alloys. The sums P_1', Q_1', P_1'', Q_1'', P_2', Q_2', P_2'', Q_2'', which determine the main parameters of the shear-stress field, are also individual for each alloy. It should be noted that they are not random quantities like the shear stresses in the glide plane, which depend on the specific random arrangement of various solute atoms. This is one of the advantages of the proposed method in comparison with the method of direct summation of contributions from solute atoms.

3.2. Temperature Dependence of Yield Strength of CrCoNiFeMn Alloy

A multicomponent CrCoNiFeMn alloy was also used to model the temperature dependence of the yield strength taking into account the short- and long-wavelength components of the stochastic shear-stress field in the glide plane. The input and calculated parameters of modelling are listed in Table 2. An important parameter is also the coefficient $\alpha = 0.123$, which determines the linear tension of the dislocation line in the CrCoNiFeMn alloy [12]. The Peierls–Nabarro stress, *i.e.*, the frictional stress of the lattices of the virtual matrix-solvent, can be estimated as for metals with f.c.c. lattice and taken, for example, to be approximately $\tau_P = 3$ MPa [4]. The temperature dependence of the yield strength in this material taking into account only solid solution strengthening is shown in Fig. 7. The solid line corresponds to calculations using equations (29) for the averaged main parameters of the shear-stress field, which are given in Table 2. Circles, triangles, and squares are experimental data taken from the literature [38–40]. The grey band corresponds to the band of possible theoretical yield strengths, taking into account the inaccuracy of the main parameters determination. Experimental values from different sources correlate well with each other and with the modelled dependence. They demonstrate clearly 'plateau' at temperatures above approximately 650 K. The theoretical dependence smoothly transitions to this 'plateau'. There is a deviation of the calculated dependence from the experimental values in the region of very low temperatures.

TABLE 2. The input and calculated parameters of modelling the temperature dependence of yield strength of the CrCoNiFeMn alloy [36].

G, GPa	81	$s_1(2w_2)$, MPa	180	$s_2(2w_2)$, MPa	71
α	0.123	w_1, nm	0.38	w_2, nm	1
τ_P, MPa	3	L_1, nm	12.97	L_2, nm	45.96
b, nm	0.25	τ_{y1}, MPa	70.69	τ_{y2}, MPa	14.81
T_0, K	664	E_{b1}, eV	0.92	E_{b2}, eV	1.8

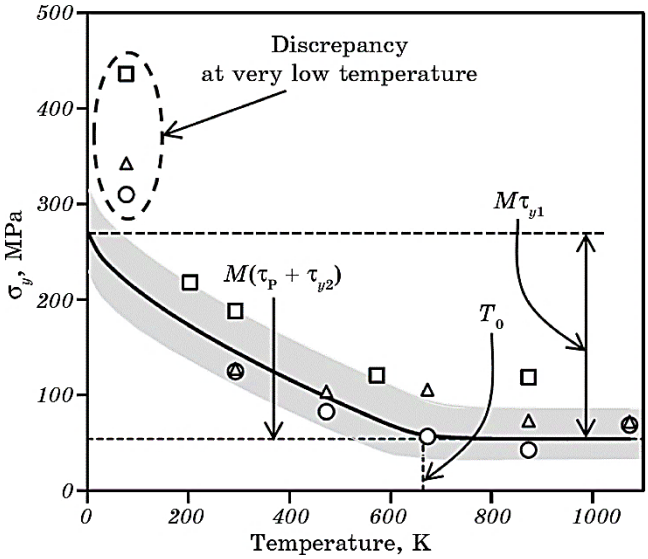

Fig. 7. Temperature dependence of the yield strength of the CrCoNiFeMn alloy taking into account only solid solution strengthening [36]. The solid line is a calculation using equations (29) for the averaged main parameters of the shear-stress field, which are presented in Table 2. Circles, triangles, and squares are experimental values taken from [38], [39], and [40], respectively. The grey band corresponds to the band of possible theoretical yield strengths, taking into account the inaccuracy of the main parameters determination.

The stochastic shear-stress field in the glide plane was not calculated at all in work [11], that is, its short- and long-wavelength components were not determined as well. Nevertheless, a force barrier of a sinusoidal profile was considered similarly to our work as an obstacle for the dislocation motion. The height of this barrier was determined on the basis of the interaction energies of solute atoms with dislocations calculated from first principles [11]. The temperature dependence of the yield strength of the CrCoNiFeMn alloy was obtained from the analysis of dislocation overcoming of this sinusoidal force barrier

in this paper. It is obvious that the athermal component of the yield strength associated with solid solution strengthening and with long-wavelength component of the shear-stress field was not considered at all in [11].

In fact, the theoretical temperature dependence from [11] does not have a 'plateau' demonstrated by experimental data [38–40]. Instead, this dependence smoothly goes to zero without a 'plateau'. Perhaps that is why the theoretical temperature dependence and experimental data from [38] are compared in [11] only up to a temperature of 673 K, and this is only the very beginning of the 'plateau' for the CrCoNiFeMn alloy. The 'plateau' exists for this alloy at least from 670 K to 1073 K. In addition, the theoretical temperature dependence from [11] at 673 K is slightly below the experimental value. This theoretical dependence will be even lower at higher temperatures, when the experimental data show a 'plateau', that is, an almost constant value of the yield strength. On the other hand, this dependence practically coincides with the experimental value from [38] at 293 K, but is lower than the value from [40] at this temperature. Instead, the theoretical temperature dependence of the yield strength of the CrCoNiFeMn alloy, which was calculated in our paper, is higher than the similar dependence from the paper [11]. This better correlates with the entire set of experimental data from Refs. [38–40], except for the range of very low temperatures. Such discrepancy is explained by a possible change in the linear tension of the dislocation line in this temperature range in [11]. However, this assumption requires further research. It should also be added that at sufficiently high temperatures, which are not considered in this work, the yield strength will no longer be on the 'plateau', but will start to decrease sharply due to the action of other mechanisms of plastic deformation instead of dislocation gliding.

The main advantage of our approach is that it takes into account the athermal component of the yield strength associated with solid solution strengthening. This component can be associated with the long-wavelength component of the stochastic stress field in the glide plane. In this case, it is possible to calculate the theoretical 'plateau' stress almost exactly. On the other hand, if the force barrier for the dislocation motion, which can be overcome with the thermal activation assistance and which determines the course of the temperature dependence of the yield strength, is connected with the short-wavelength component, then the temperature of the beginning of the 'plateau' can be fairly accurately predicted (T_0 in Table 2). This cannot be done within the framework of the model from work [11]. The activation volume at 293 K, calculated from our theoretical temperature dependence according to the method from [12], is equal to $V = 147b^3$. This correlates well with the value $2w_1L_1b \approx 153b^3$ obtained from the geometrical parameters of the average dislocation bulge for the CrCoNiFeMn alloy

(Table 2). On the other hand, this value has one order of magnitude with the value $\sim 350b^3$ for this alloy, which was determined by the experimental method in [41].

4. CONCLUSION

Atomic size misfits and elastic modulus misfits at the crystal lattice sites can be considered as discrete random variables with a mathematical expectation equal to zero and a certain non-zero variance. Analytical expressions for the standard deviations and correlation lengths of the short- and long-wavelength components of the stochastic shear-stress field created by solute atoms in the glide plane in a multicomponent alloy were obtained from the variance definition of these random variables. The developed method was verified by calculating the main parameters of shear-stress field for the CrCoNiFeMn alloy. The calculated parameters were well correlated with similar parameters determined from the analysis of shear-stresses' distributions in the glide plane, which were calculated by the method of direct summation of contributions from solute atoms. It was found that it is possible to define two different effective distortions of crystal lattice, which cause short- and long-wavelength components of the stress field, respectively. In addition, it was established that there is no single empirical constant for all alloys to determine the yield strength using the shear modulus and the average lattice distortion. However, it is possible to calculate the yield strength of a specific multicomponent alloy using the main parameters of the shear-stress field, which are determined by the method considered in this paper.

The periodic lattice potential, short- and long-wavelength components of the stochastic shear-stress field in the glide plane determine the yield strength of a multicomponent alloy taking into account only solid solution strengthening. The force barriers from the short- and long-wavelength components are described using the main parameters of the shear-stress field. The force barrier for the dislocation motion from the short-wavelength component is dominant in a multicomponent alloy, which is a concentrated solid solution. In this case, the beginning of dislocation motion is determined by overcoming this barrier with the assistance of applied stress and thermal activation. The effect of barriers from the periodic lattice potential and the long-wavelength component on the yield strength can be taken into account by constant terms that do not depend on temperature. This is possible because these barriers are quite low in comparison with the barrier from the short-wavelength component in a concentrated solid solution. The temperature dependence of the yield strength of a multicomponent alloy in a wide temperature range can be determined using thermal activation analysis of overcoming barriers from the short-wavelength

component, taking into account the probability of forward and backward jumps through the barriers and the constant stresses that take into account the barriers from the periodic lattice potential and long-wavelength component. Effect of solute atoms located farther from the glide plane on yield strength cannot be neglected because they create long-wavelength component of the shear-stress field. The temperature dependence of the yield strength calculated in this way describes well the region of the high-temperature 'plateau'. This dependence, calculated for the CrCoNiFeMn alloy, also correlates well with the corresponding experimental data for this alloy.

REFERENCES

1. D. B. Miracle and O. N. Senkov, *Acta Mater.*, **122**: 448 (2017).
2. E. P. George, W. A. Curtin, and C. C. Tasan, *Acta Mater.*, **188**: 435 (2020).
3. F. R. N. Nabarro and P. B. Hirsch, *The Physics of Metals* (Cambridge: Cambridge University Press: 1976), p. 152.
4. A. S. Argon, *Strengthening Mechanisms in Crystal Plasticity* (Oxford: Oxford University Press: 2008).
5. M. Lugovy, D. Verbylo, and M. Brodnikovskyy, *Uspikhy Materialoznavstva*, Nos. 4/5: 36 (2022) (in Ukrainian).
6. R. Labusch, *Czech. J. Phys. B*, **31**: 165 (1981).
7. G. Leyson, W. Curtin, L. Hector, and C. F. Woodward, *Nature Mater.*, **9**: 750 (2010).
8. G. P. M. Leyson, L. G. Hector, and W. A. Curtin, *Acta Mater.*, **60**, No. 9: 3873 (2012).
9. G. P. M. Leyson and W. A. Curtin, *Phil. Mag.*, **93**, Iss. 19: 2428 (2013).
10. G. P. M. Leyson and W. A. Curtin, *Modelling Simulation Mater. Sci. Eng.*, **24**: 065005 (2016).
11. C. Varvenne, A. Luque, and W. A. Curtin, *Acta Mater.*, **118**: 164 (2016).
12. C. Varvenne, G. P. M. Leyson, M. Ghazisaeidi, and W. A Curtin, *Acta Mater.*, **124**: 660 (2017).
13. W. G. Nöhring and W. A. Curtin, *Scripta Mater.*, **168**: 119 (2019).
14. G. Bracq, M. Laurent-Brocq, C. Varvenne, L. Perrière, W. A. Curtin, J.-M. Joubert, and I. Guillot, *Acta Mater.*, **177**: 266 (2019).
15. Y. Hu, B. A. Szajewski, D. Rodney, and W. A. Curtin, *Modelling Simulation Mater. Sci. Eng.*, **28**: 015005 (2020).
16. M. Zaiser, *Phil. Mag. A*, **82**, No. 15: 2869 (2002).
17. J.-H. Zhai and M. Zaiser, *Mater. Sci. Eng. A*, **740–741**: 285 (2019).
18. G. Péterffy, P. D. Ispánovity, M. E. Foster, X. Zhou, and R. B. Sills, *J. Mater. Sci.: Mater. Theory*, **4**: 6 (2020).
19. R. Pasianot and D. Farkas, *Computational Mater. Sci.*, **173**: 109366 (2020).
20. M. Lugovy, V. Slyunyayev, and M. Brodnikovskyy, *Progress in Natural Sci.: Mater. Int.*, **31**: 95 (2021).
21. M. Lugovy, V. Slyunyayev, M. Brodnikovskyy, and S. Firstov, *Ehlektronnaya Mikroskopiya i Prochnost' Materialov*, Iss. 23: 3 (2017) (in Ukrainian).
22. M. Lugovy, V. Slyunyayev, and M. Brodnikovskyy, (2019). *Ehlektronnaya Mikroskopiya i Prochnost' Materialov*, Iss. 25: 26 (2019) (in Russian).

23. M. Lugovy, D. Verbylo, and M. Brodnikovskyy, *Uspikhy Materialoznavstva*, No. 2: 19 (2021) (in Ukrainian).
24. M. Lugovy, D. Verbylo, and M. Brodnikovskyy, *Uspikhy Materialoznavstva*, No. 3: 24 (2021) (in Ukrainian).
25. S. O. Firstov and T. G. Rogul, *Metallofiz. Noveishie Tekhnol.*, **44**, No. 1: 127 (2022) (in Ukrainian).
26. A. V. Podolskiy, E. D. Tabachnikova, V. V. Voloschuk, V. F. Gorban, N. A. Krapivka, and S. A. Firstov, *Mater. Sci. Eng. A*, **710**: 136 (2018).
27. S. O. Firstov, T. G. Rogul, N. A. Krapivka, and S. I. Chugunova, *Metallofiz. Noveishie Tekhnol.*, **40**, No. 2: 219 (2018) (in Russian).
28. S. O. Firstov and T. G. Rogul, *Metallofiz. Noveishie Tekhnol.*, **39**, No. 1: 33 (2017) (in Russian).
29. L. A. Gypen and A. Deruyttere, *J. Mater. Sci.*, **12**: 1028 (1977).
30. I. Toda-Caraballo, *Scripta Mater.*, **127**: 113 (2017).
31. U. F. Kocks, A. S. Argon, and M. F. Ashby, *Progress Mater. Sci.*, **19**: 110 (1975).
32. R. L. Fleischer, *Acta Metallurgica*, **11**: 203 (1963).
33. M. Lugovy, D. Verbylo, and M. Brodnikovskyy, *Uspikhy Materialoznavstva*, Nos. 4/5: 12 (2022) (in Ukrainian).
34. G. Gremaud, *Mater. Sci. Eng. A*, **370**: 191 (2004).
35. M. Lugovy, D. Verbylo, and M. Brodnikovskyy, *Uspikhy Materialoznavstva*, No. 7: 3 (2023) (in Ukrainian).
36. M. Lugovy, D. Verbylo, and M. Brodnikovskyy, *Uspikhy Materialoznavstva*, No. 6: 15 (2023) (in Ukrainian).
37. R. Labusch, *phys. status solidi (b)*, **41**, Iss. 2: 659 (1970).
38. F. Otto, A. Dlouhy, C. Somsen, H. Bei, G. Eggeler, and E. P. George, *Acta Mater.*, **61**: 5743 (2013).
39. A. Gali and E. P. George, *Intermetallics*, **39**: 74 (2013).
40. S. J. Sun, Y. Z. Tian, H. R. Lin, X. G. Dong, Y. H. Wang, Z. J. Wang, and Z. F. Zhang, *J. Alloys Compd.*, **806**: 992 (2019).
41. G. Laplanche, J. Bonneville, C. Varvenne, W. A. Curtin, and E. P. George, *Acta Mater.*, **143**: 257 (2018).

Metallophysics and Advanced Technologies
Металофіз. новітні технол.
Metallofiz. Noveishie Tekhnol.
2025, vol. 47, No. 3, pp. 335–346
https://doi.org/10.15407/mfint.47.03.0335
Reprints available directly from the publisher

PACS numbers: 46.50.+a, 62.20.F-, 81.20.Hy, 81.20.Wk, 81.40.Ef, 81.40.Jj, 83.50.Uv

Analysis of Deformation Forces in Simulation of a New Thermomechanical Wire Processing

I. E. Volokitina and E. A. Panin

Karaganda Industrial University,
30 Republic Ave.,
101400 Temirtau, Republic of Kazakhstan

This work is concerned with the study of the emerging deformation forces during the implementation of a new method of thermomechanical wire processing that is a combined process including successive stages of wire drawing and cooling in a special chamber with liquid nitrogen. The analysis of forces is carried out by finite-elements' modelling of the combined process within the DEFORM program. As found, the presence of intermediate heating to ambient temperature allows calculating the force according to the Krasilshchikov formula and the well-known nomogram of the tensile strength of AISI-316 steel at 20°C with minimal errors. The deformation without intermediate heating leads to the negative temperatures in the workpiece section in the second and third drawing cycles.

Key words: drawing, wire, modelling, steel, stress–strain state, cryogenic cooling.

Роботу присвячено дослідженню деформаційних сил, які виникають під час реалізації нового методу термомеханічного оброблення дроту, що являє собою комбінований процес, який включає послідовні стадії волочіння й охолодження дроту в спеціяльній камері з рідким азотом. Аналіза сил проводилася за допомогою моделювання комбінованого процесу за методом скінченних елементів за програмою DEFORM. Встановлено, що наявність проміжного нагріву до температури навколишнього середови-

Corresponding author: Irina E. Volokitina
E-mail: irina.vav55@gmail.com

Citation: I. E. Volokitina and E. A. Panin, Analysis of Deformation Forces in Simulation of a New Thermomechanical Wire Processing, *Metallofiz. Noveishie Tekhnol.*, **47**, No. 3: 335–346 (2025). DOI: 10.15407/mfint.47.03.0335

ща уможливлює розраховувати зусилля за формулою Красильщикова та відомою номограмою межі міцности криці AISI-316 за 20°C із мінімальними похибками. Деформація без проміжного нагріву приводить до неґативних температур у перерізі заготовки в другому та третьому циклах витягування.

Ключові слова: волочіння, дріт, моделювання, криця, напружено-деформований стан, кріогенне охолодження.

(Received 27 March, 2024; in final version, 6 May, 2024)

1. INTRODUCTION

Metallic materials are characterized by special useful properties due to their structural structure. It is well known that the properties of materials are based on structure and, therefore, they can significantly depend on the manufacturing process. Modern production methods make it possible to obtain specialized materials based on both steels and nonferrous metals (for example, gradient or composite structures [1–3]), which are able to meet individual and ever-increasing demands based on the requirements of modern technologies. However, the production of such materials without the addition of expensive alloying elements or the inclusion of energy and economically costly heat treatment, often used to improve mechanical properties, remains a serious problem. One of the promising options is to increase the performance characteristics of metal materials by reducing the grain size in their structure.

According to the grain size, metal materials can be divided into several groups. The first group includes materials determined by the casting structure (castings). The second group of materials is determined by the reduced grain size achieved, for example, by plastic deformation (traditional metal forming processes). The third group of materials is characterized by a very small grain size, *i.e.*, materials obtained by severe plastic deformation, powder metallurgy, *etc*. Further, they can be divided into ultrafine-grained (UFG) materials and nanomaterials (NM). NM can be defined as materials with a structural unit (grain) size in the range of 1–100 nm (at least in one direction), while UFG materials can be defined by grain size in the range of 100–1000 nm [4–7].

The deformation behaviour of the material is significantly influenced not only by the grain size, but also by the nature and number of their boundaries [8–14]. However, as the grain size decreases, determined in the nanometre range, the properties of materials change dramatically, so that even at high temperatures these materials can be stronger than coarse-grained ones. Thermomechanical (TM) processing allows to control the course of structural processes (*i.e.*, influence the grain size, ratio and character of grain boundaries), and therefore determine the final structure, *i.e.*, mechanical properties, of

the material already during its processing. Although in practice this type of moulding can lead to a reduction in grain size to the submicrometre range, further refinement using traditional forming methods is usually no longer possible, even if they are used in TM processing. For this reason, other methods are being sought for the production of nanomaterials, among which methods of severe plastic deformation are most often used.

When obtaining NM, two factors are crucial: the processing temperature and the shear stress. Therefore, deformation processes in which the shear stress component prevails are the most suitable for obtaining very fine-grained structures. The relationship between mechanical properties and grain size is usually described by the Hall–Petch dependence, which determines an increase in strength characteristics with a decrease in grain size. There are studies [15, 16] conducted in the field of cryogenic deformations, which confirm the effectiveness of cryogenic cooling during deformation in terms of refinement structural elements. Thus, in [15, 17] it was proved that the microstructure of the initial coarse-grained copper and aluminium after cryogenic deformation differs significantly in a smaller grain size than after conventional cold deformation. Therefore, in our combined thermomechanical processing, it is proposed to use cryogenic cooling immediately after the wire leaves the drawing using liquid nitrogen, which will give a more favourable compromise between the strength and ductility of the material.

2. EXPERIMENTAL

The developed technology of thermomechanical wire processing is a combined process that includes successive stages of wire drawing and cooling in a special chamber with liquid nitrogen (Fig. 1).

The wire loading process is the same as with conventional drawing at room temperature. The pointed end of the wire is inserted into the fibre, after which it is passed through an empty tank chamber, where cryogenic cooling is carried out. This storage chamber is installed in the rolling line directly behind the drawing unit. Then the end of the wire is fixed to the drum of the drawing mill and wound onto the drum. When the extractor reaches the working tension speed, the tank chamber is filled with liquid nitrogen. The tank chamber is equipped with a nitrogen recirculation system. The initial diameter of the wire was 6 mm, during the first pass it changed to 5.6 mm, then on the second pass from 5.6 mm to 5.3 mm and on the third to 5 mm. It was also decided to consider drawing thicker wire with a diameter of 9 mm. Here, the workpiece was deformed to 8.2 mm, then on the second pass from 8.2 mm to 7.5 mm and on the third pass from 7.5 mm to 7 mm.

At the theoretical stage of research on deformation processes in which there is a drawing scheme, a study of force parameters is usually

carried out, since the very possibility of deformation of the wire depends on the magnitude of the force.

The drawing force depends on various geometric and technological factors, such as the mechanical properties of the deformable material, the amount of compression, external friction, the shape and size of the drawing, the drawing speed, the presence or absence of tension at the front and rear ends of the workpiece, as well as the transverse area of the resulting profile. For solid round profiles, you can use the Kra-

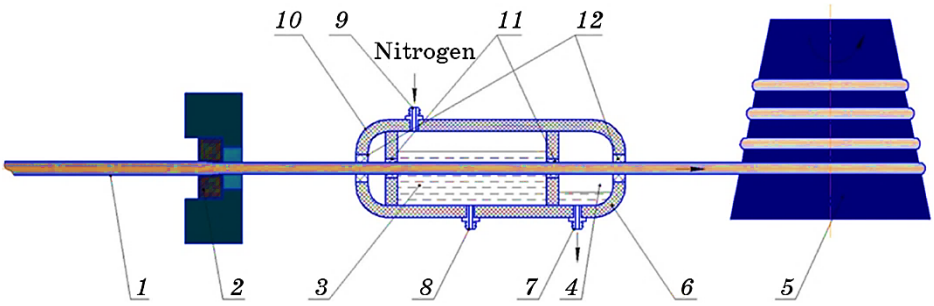

Fig. 1. Installation diagram for thermomechanical wire processing: *1* is wire, *2* is lugs in a fibre holder, *3* is cryogenic cooling chamber, *4* is chamber for collecting excess nitrogen, *5* is drum of the drawing mill, *6* is thermal insulation layer, *7* is removal of liquid nitrogen residues, *8* is nitrogen pumping, *9* is liquid nitrogen supply, *10* is cryogenic installation, *11* is fine seals, *12* is sealing seals for coarse cleaning.

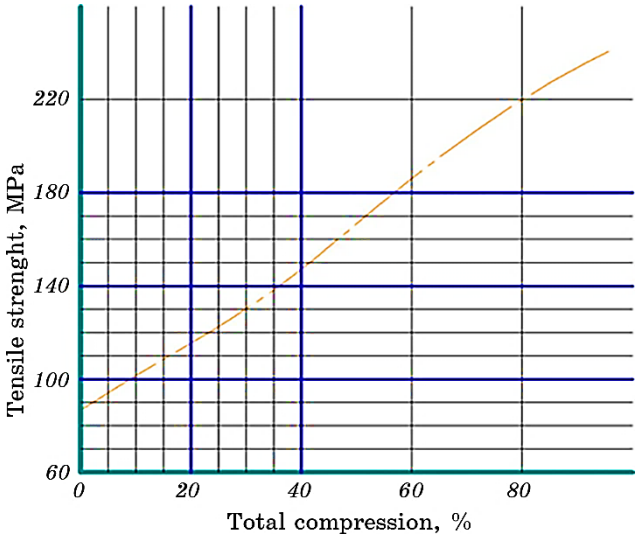

Fig. 2. Nomogram of the tensile strength of AISI-316 steel during drawing at 20°C.

TABLE 1. Parameters of wire drawing of AISI-316 steel.

No. of pass	D_0, mm	D_1, mm	F_1, mm^2	F_2, mm^2	ε (single), %	ε (total), %	σ_{B0}, MPa	σ_{B1}, MPa	σ_{BAV}, MPa
Drawing a workpiece with a diameter of 6 mm									
1 pass	6	5.6	28.26	24.61	12.89	12.89	862	1038	950
2 pass	5.6	5.3	24.62	22.05	10.43	21.97	1038	1156	1097
3 pass	5.3	5	22.05	19.62	11	30.55	1156	1284	1220
Drawing a workpiece with a diameter of 9 mm									
1 pass	9	8.2	63.59	52.78	16,98	16.98	862	1080	971
2 pass	8.2	7.5	52.78	44.16	16,34	30.55	1080	1284	1182
3 pass	7.5	7	44.16	38.46	12,89	39.5	1284	1420	1352

silshchikov formula, which was obtained on the basis of numerous experimental data:

$$P = 0.6d_0^2\sqrt{(d_0^2 - d_1^2) / d_0^2}\sigma_{BCP}\,. \quad (1)$$

Identify applicable funding agency here. If none, delete this text box.

The determination of the average tensile strength during drawing is carried out according to nomograms based on the results of experimental tensile tests after a series of draws at different compressions. In particular, for austenitic stainless steel AISI-316, deformable at 20°C, it is necessary to use the nomogram shown in Fig. 2.

In accordance with Fig. 2, the values of the strength limits for each passage of both thicknesses of the workpieces were determined. The results were summarized in Table 1.

3. RESULTS AND DISCUSSION

Using Eq. (1), when drawing a wire with a diameter of 6 mm, the following force values were obtained: on the first pass from 6 mm to 5.6 mm = 44201 N, on the second pass from 5.6 mm to 5.3 mm = 37326 N, on the third pass from 5.3 mm to 5 mm = 36144 N.

When drawing a wire with a diameter of 9 mm, the following force values were obtained: on the first pass from 9 mm to 8.2 mm = 175051 N, on the second pass from 8.2 mm to 7.5 mm = 158087 N, on the third pass from 7.5 mm to 7 mm = 122863 N.

To verify the correctness of the received data, it was decided to carry out verification using finite element modelling. The thermomechanical processing route was carried out in two variants, in each variant the workpiece was deformed to a predetermined diameter, after which

it fell into a container with liquid nitrogen.

In the first variant, the workpiece was heated in air to a temperature of 20°C after each treatment with liquid nitrogen. In the second variant, this heating was absent. For the first option, the nomogram in Fig. 2 is completely suitable, since before each stage of drawing, the workpiece is evenly heated to room temperature.

Given that in the second variant, the workpiece will have a negative temperature after nitrogen treatment, the usual Deform material database will not be suitable for such modelling, since the standard lower temperature limit is 20°C. In [18], FEM modelling of this steel under cryogenic cooling was carried out. For this purpose, a new database was developed, which included the rheological properties of AISI-316 steel up to –200°C. This database of material is available at https://data.mendeley.com/datasets/6m5r6f2z5g/1.

At the same time, it must be borne in mind that in this case the nomogram in Fig. 2 will give a noticeable error. Using a similar nomogram for cryogenic conditions will also not give good convergence for the following reason. The simulation was carried out at two deformation rates: 500 mm/s and 1000 mm/s. Accordingly, it was assumed that any wire section is in liquid nitrogen for a certain amount of time: 1 s at a speed of 500 mm/s and 0.5 s at a speed of 1000 mm/s. As a result, the workpiece after such a short-term treatment with liquid nitrogen will have a significant temperature gradient across the cross section, which will lead to an uneven distribution of mechanical properties.

Figures 3, 4 show graphs of the forces when drawing workpieces with diameters of 6 and 9 mm using heating at a speed of 500 mm/s. The results on the first pass remain unchanged, so are not considered further. All force values were summarized in Table 2. Comparing the values obtained during calculation and modelling, it is necessary to note their high convergence; the error level is less than 1%.

Figures 5, 6 show force plots for drawing 6 and 9 mm diameter billets using heating at a speed of 1000 mm/s.

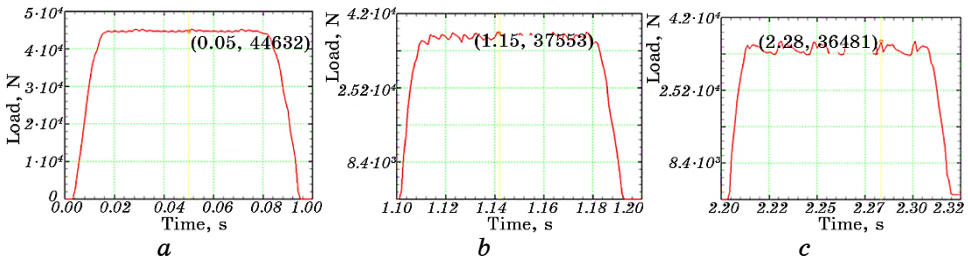

Fig. 3. Graphs of forces when drawing a wire with a diameter of 6 mm with a heated workpiece at a speed of 500 mm/s: the first pass (*a*), the second pass (*b*), the third pass (*c*).

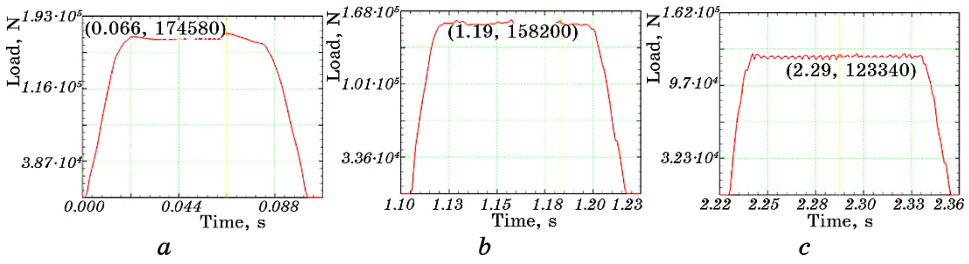

Fig. 4. Graphs of forces when drawing a wire with a diameter of 9 mm with a heated workpiece at a speed of 500 mm/s: the first pass (*a*), the second pass (*b*), the third pass (*c*).

TABLE 2. Force values during the calculation and in model with a heated workpiece at a speed of 500 mm/s.

Drawing a workpiece with a diameter of 6 mm					
No. of pass	D_0, mm	D_1, mm	Calculated force, N	Force in the model, N	Difference, %
1 pass	6	5.6	44201	44362	0.36
2 pass	5.6	5.3	37326	37553	0.6
3 pass	5.3	5	36144	36481	0.92
Drawing a workpiece with a diameter of 9 mm					
1 pass	9	8.2	175051	174580	0.27
2 pass	8.2	7.5	158087	158200	0.07
3 pass	7.5	7	122863	123340	0.38

All force values were summarized in Table 3. Comparing the values obtained during calculation and modelling, it is necessary to note their high convergence, while the error level increased to 3–5%. Thus, with an increased rate of deformation, the use of the tensile strength nomogram is correct.

Figures 7, 8 show graphs of the forces when drawing workpieces with diameters of 6 and 9 mm without using heating at a speed of 500 mm/s. The results on the first pass remain unchanged, so they are not considered further.

All the effort values were summarized in Table 4. Comparing the values obtained during calculation and modelling, it is necessary to note a high level of error, which is approximately 35% for a diameter of 6 mm and 25% for a diameter of 9 mm. The decrease in error with an increase in the thickness of the workpiece is due to the fact that with an increased thickness and a constant cooling time in nitrogen, a higher temperature gradient occurs when the central layers are cooled less intensively.

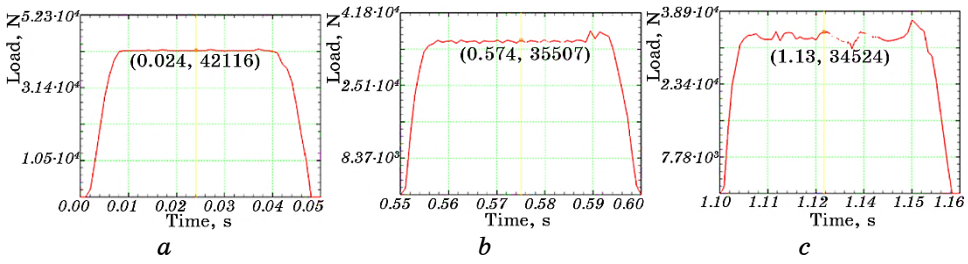

Fig. 5. Graphs of forces when drawing a wire with a diameter of 6 mm with a heated workpiece at a speed of 1000 mm/s: the first pass (*a*), the second pass (*b*), the third pass (*c*).

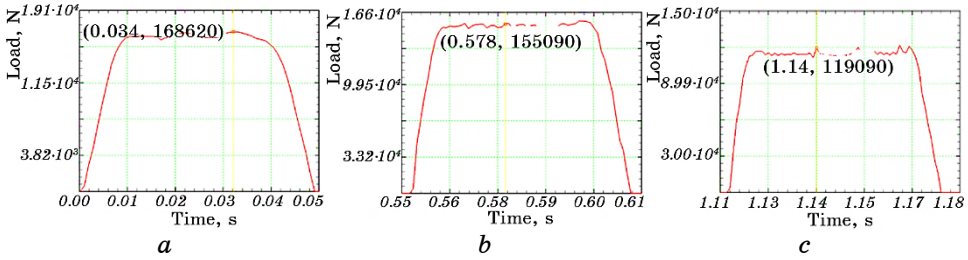

Fig. 6. Graphs of forces when drawing a wire with a diameter of 6 mm with a heated workpiece at a speed of 1000 mm/s: the first pass (*a*), the second pass (*b*), the third pass (*c*).

TABLE 3. Force values during the calculation and in model with a heated workpiece at a speed of 1000 mm/s.

Drawing a workpiece with a diameter of 6 mm					
No. of pass	D_0, mm	D_1, mm	Calculated force, N	Force in the model, N	Difference, %
1 pass	6	5.6	44201	42116	4.95
2 pass	5.6	5.3	37326	35507	5.12
3 pass	5.3	5	36144	34524	4.69
Drawing a workpiece with a diameter of 9 mm					
1 pass	9	8.2	175051	168620	3.81
2 pass	8.2	7.5	158087	155090	1.93
3 pass	7.5	7	122863	119090	3.16

At the same time, all calculated values are lower than the values obtained during modelling, which is the result of deformation at a reduced temperature. Taking into account the results obtained, it can be

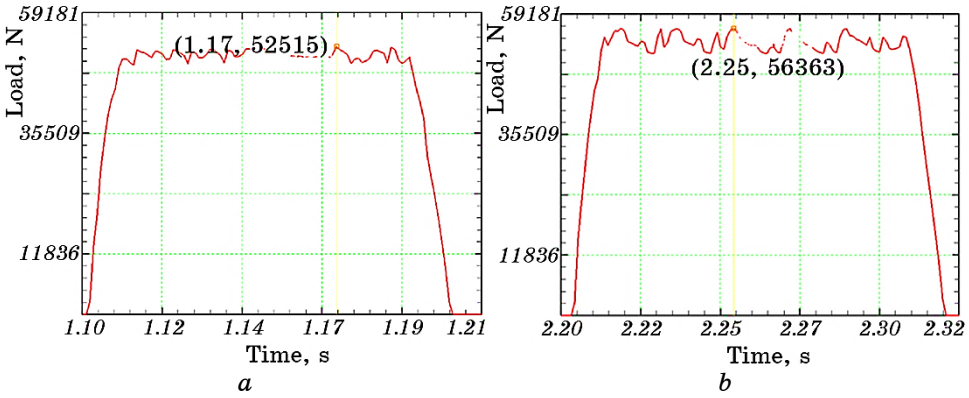

Fig. 7. Graphs of forces when drawing wire with a diameter of 6 mm without heating the workpiece at a speed of 500 mm/s: the second pass (*a*), the third pass (*b*).

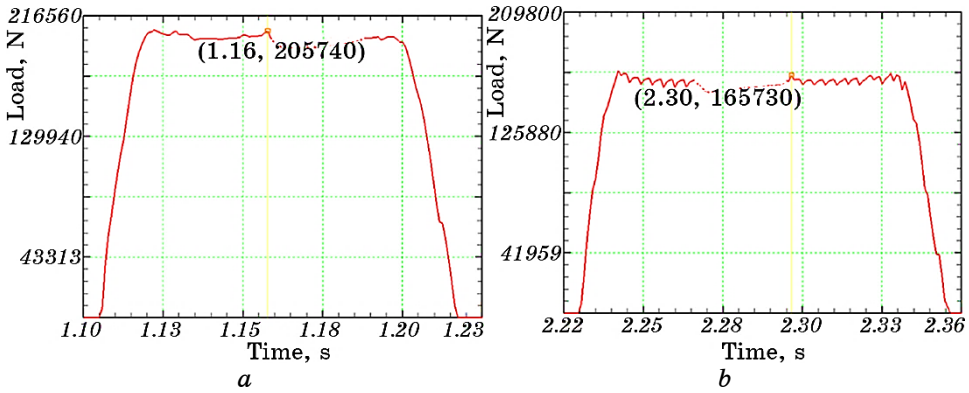

Fig. 8. Graphs of forces when drawing wire with a diameter of 6 mm without heating the workpiece at a speed of 500 mm/s: the second pass (*a*), the third pass (*b*).

recommended to increase the calculated values by about 35% for a diameter of 6 mm and by 25% for a diameter of 9 mm when using a calculation technique and a nomogram to obtain correct values.

Figures 9, 10 show graphs of the forces when drawing workpieces with diameters of 6 and 9 mm without using heating at a speed of 1000 mm/s.

All the effort values were summarized in Table 5. Comparing the values obtained during calculation and modelling, it is necessary to note a high level of error, which is approximately 30% for a diameter of 6 mm and 20% for a diameter of 9 mm. Taking into account the results obtained, it can be recommended to increase the calculated values by approximately the specified difference values when using the calcu-

TABLE 4. Force values during calculation and in model without workpiece heating at a speed of 500 mm/s.

No. of pass	D_0, mm	D_1, mm	Calculated force, N	Force in the model, N	Difference, %
Drawing a workpiece with a diameter of 6 mm					
2 pass	5.6	5.3	37326	52515	28.92
3 pass	5.3	5	36144	56363	35.87
Drawing a workpiece with a diameter of 9 mm					
2 pass	8.2	7.5	158087	205740	23.16
3 pass	7.5	7	122863	165730	25.86

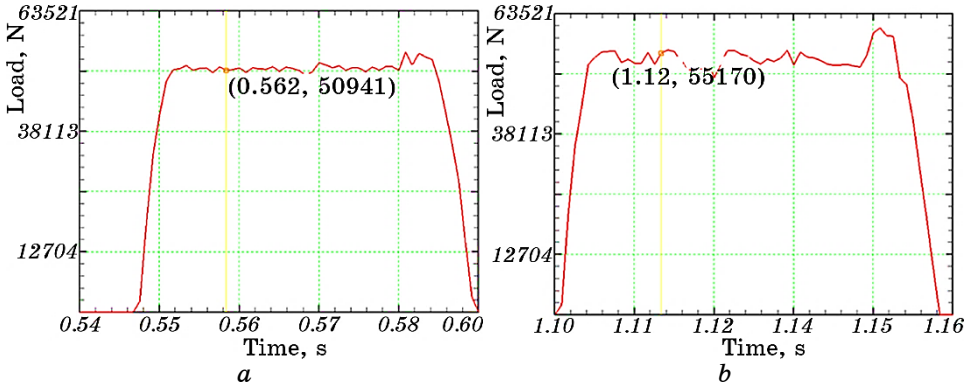

Fig. 9. Graphs of forces when drawing wire with a diameter of 6 mm without heating the workpiece at a speed of 1000 mm/s: the second pass (*a*), the third pass (*b*).

lation method and nomogram to obtain correct values.

4. CONCLUSION

In this paper, a new combined technology of multi-cycle thermomechanical processing including conventional wire drawing and subsequent cooling in liquid nitrogen has been simulated in the Deform software package. The results show that the presence of intermediate heating to room temperature allows calculating the forces with minimal error using Krasilshchikov equation and the known nomogram of tensile strength at 20°C for AISI-316 steel. When deforming without intermediate heating, the cross-sectional temperature of the billet becomes negative during the second and third drawing cycles.

This research is funded by the Science Committee of the Ministry of

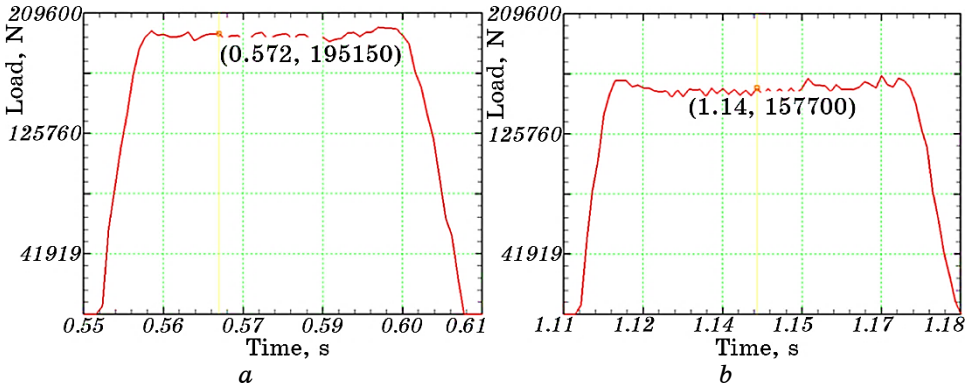

Fig. 10. Graphs of forces when drawing wire with a diameter of 9 mm without heating the workpiece at a speed of 1000 mm/s: the second pass (*a*), the third pass (*b*).

TABLE 5. Force values during calculation and in model without workpiece heating at a speed of 1000 mm/s.

Drawing a workpiece with a diameter of 6 mm					
No. of pass	D_0, mm	D_1, mm	Calculated force, N	Force in the model, N	Difference, %
2 pass	5.6	5.3	37326	50941	26.72
3 pass	5.3	5	36144	55170	34.48
Drawing a workpiece with a diameter of 9 mm					
2 pass	8.2	7.5	158087	195150	19
3 pass	7.5	7	122863	157700	22.1

Science and Higher Education of the Republic of Kazakhstan (Grant No. AP19576369).

REFERENCES

1. M. O. Kurin, O. O. Horbachov, A. V. Onopchenko, and T. V. Loza, *Metallofiz. Noveishie Tekhnol.*, **44**, No. 6: 785 (2022).
2. G. I. Raab, L. A. Simonova, and G. N. Aleshin, *Metalurgija*, **55**: 177 (2016).
3. I. E. Volokitina, A. V. Volokitin, and E. A. Panin, *Progress in Physics of Metals*, **23**, No. 4: 684 (2022).
4. B. Sapargaliyeva, A. Agabekova, G. Ulyeva, A. Yerzhanov, and P. Kozlov, *Case Studies Construction Mater.*, **18**: e02162 (2023).
5. A. Bychkov and A. Kolesnikov, *Metallography, Microstructure, and Analysis*, **12**: 564 (2023).

6. I. E. Volokitina, *Progress in Physics of Metals*, **24**, No. 3: 593 (2023).
7. I. E. Volokitina, A. V. Volokitin, M. A. Latypova, V. V. Chigirinsky, and A. S. Kolesnikov, *Progress in Physics of Metals*, **24**, No. 1: 132 (2023).
8. E. Panin, T. Fedorova, D. Lawrinuk, A. Kolesnikov, A. Yerzhanov, Z. Gelmanova, and Y. Liseitsev, *Case Studies Construction Mater.*, **19**: e02609 (2023).
9. I. Volokitina, *J. Chem. Technol. Metallurgy*, **57**: 631 (2022).
10. W. H. Huang, C. Y. Yu, P. W. Kao, and C. P. Chang, *Mater. Sci. Eng. A*, **356**: 321 (2004).
11. K. Lu., *Science*, **345**: 1455 (2014).
12. T. H. Fang, W. L. Li, N. R. Tao, and K. Lu, *Science*, **331**: 1587 (2011).
13. A. Volokitin, I. Volokitina, and E. Panin, *Metallography, Microstructure, and Analysis*, **11**: 673 (2022).
14. M. Murugesan, D. Won, and J. Johnson, *Mater.*, **12**: 609 (2019).
15. N. Zhangabay, I. Baidilla, A. Tagybayev, Y. Anarbayev, and P. Kozlov, *Case Studies Construction Mater.*, **18**: e02161 (2023).
16. I. Volokitina, A. Volokitin, A. Denissova, T. Fedorova D. Lawrinuk, A. Kolesnikov, A. Yerzhanov, Y. Kuatbay, and Y. Liseitsev, *Case Studies Construction Mater.*, **19**: e02346 (2023).
17. I. E. Volokitina, *Metal Sci. Heat Treatment*, **63**: 163 (2021).
18. I. Volokitina, A. Volokitin, and D. Kuis, *J. Chem. Technol. Metallurgy*, **56**: 643 (2021).